MICROMECHANICS FAILURE CRITERIA FOR COMPOSITES

Longin B. Greszczuk

McDonnell Douglas Astronautics Company

Prepared for:

Naval Air Systems Command

7 May 1973

FINAL SUMMARY REPORT

MICROMECHANICS FAILURE CRITERIA FOR COMPOSITES

Contract No. N00019-72-C-0221

by L. B. Greszczuk

May 1973

McDonnell Douglas Astronautics Company
Huntington Beach, California 92647

Prepared for

U.S. Naval Air Systems Command
Washington, D.C. 20360

DOCUMENT CONTROL DATA - R & D

(Security classification of title, body of abstract and indexing annotation must be entered when the overall report is classified)

1. ORIGINATING ACTIVITY (Corporate author)
McDonnell Douglas Astronautics Company
5301 Bolsa Avenue
Huntington, Beach, Calif., 92647

2a. REPORT SECURITY CLASSIFICATION
Unclassified

2b. GROUP

3. REPORT TITLE

Micromechanics Failure Criteria for Composites

4. DESCRIPTIVE NOTES (Type of report and inclusive dates)
Final Report, 3 April 1972 7 May 1973

5. AUTHOR(S) (First name, middle initial, last name)

Longin B. Greszczuk

6. REPORT DATE
7 May 1973

7a. TOTAL NO. OF PAGES
154 152

7b. NO OF REFS
20

8a. CONTRACT OR GRANT NO.
N00019-72-C-0221

b. PROJECT NO.

c.

d.

9a. ORIGINATOR'S REPORT NUMBER(S)
MDC G4701

9b. OTHER REPORT NO(S) (Any other numbers that may be assigned this report)

10. DISTRIBUTION STATEMENT

Approved for Public Release; Distribution Unlimited

11. SUPPLEMENTARY NOTES

12. SPONSORING MILITARY ACTIVITY
U. S. Naval Air Systems Command
Washington, D. C., 20360

13. ABSTRACT

Theoretical and experimental studies are presented of the micromechanics failure criteria for the transverse tensile and shear strengths of composites. Parameters accounted for in the failure theories include: fiber properties, matrix properties, fiber content, void content, volume fraction of ineffective fibers, internal triaxial stresses due to fibers and voids, and the interaction of stresses from fibers and voids. Equations are developed for predicting the influence of voids on elastic properties and internal stresses in solids containing voids. The voids are assumed to be cylindrical and arranged in a square array. Pertinent expressions are given for the Young's moduli, shear moduli, and Poisson's ratios of solids with voids. Approximate expressions are also presented for the internal stresses in solids containing voids. The theoretical results on the influence of voids on internal stresses and mechanical properties are verified experimentally using photoelastic models. Existing theory is used to predict the internal triaxial stresses in fiber-reinforced composites. Moreover, using superposition, the ineraction of internal stress concentrations due to fibers and voids is established theoretically and verified experimentally using photoelastic models. Test models are also employed to establish the strength of the material as influenced by porosity and matrix ductility. The results on fiber-void stress interaction and on the strength of brittle/ductile solids in combination with modified Hencky Von Mises Distortion Energy Criteria are used in formulating failure theories for composites subjected to transverse and shear loading. Test data from actual composites are used for final verification of the failure theories. Types of composites fabricated and tested in transverse tension and interlaminar shear include: glass epoxy, glass phenolic, graphite epoxy, graphite phenolic, and boron epoxy. The predicted transverse tensile strength of composites shows fair correlation with test data. For the composites subjected to shear loading, good correlation is obtained only between theory and test data obtained from torsion tests; the shear strength data obtained from the short-beam shear tests shows poor correlation with the theoretical prediction. Preliminary conclusions and recommendations are made on parameters influencing the transverse and shear strengths of composites and on how to improve these properties.

14. KEY WORDS	LINK A		LINK B		LINK C	
	ROLE	WT	ROLE	WT	ROLE	WT
failure criteria						
transverse tension						
shear						
micromechanics						
composite materials						
voids						
fibers						
stress concentrations						
graphite						
boron						
fiberglass						
stress interaction						
photoelasticity						

FINAL SUMMARY REPORT

MICROMECHANICS FAILURE CRITERIA FOR COMPOSITES

Contract No. N00019-72-C-0221

by L. B. Greszczuk

May 1973

McDonnell Douglas Astronautics Company
Huntington Beach, California 92647

Prepared for

U.S. Naval Air Systems Command
Washington, D.C. 20360

FOREWORD

This is the Final Report on the work performed under Naval Air Systems Command Contract N00019-72-0221, entitled "Micromechanics Failure Criteria for Composites". The report is for the period of 3 April 1972 to 7 May 1973. The principal investigator for this study was L. B. Greszczuk. The program was monitored by Mr. M. Stander, Naval Air Systems Command, Department of the Navy, Washington, D. C.

ABSTRACT

Theoretical and experimental studies are presented of the micromechanics failure criteria for the transverse tensile and shear strengths of composites. Parameters accounted for in the failure theories include: fiber properties, matrix properties, fiber content, void content, volume fraction of ineffective fibers, internal triaxial stresses due to fibers and voids, and the interaction of stresses from fibers and voids. Equations are developed for predicting the influence of voids on elastic properties and internal stresses in solids containing voids. The voids are assumed to be cylindrical and arranged in a square array. Pertinent expressions are given for the Young's moduli, shear moduli, and Poisson's ratios of solids with voids. Approximate expressions are also presented for the internal stresses in solids containing voids. The theoretical results on the influence of voids on internal stresses and mechanical properties are verified experimentally using photoelastic models. Existing theory is used to predict the internal triaxial stresses in fiber-reinforced composites. Moreover, using superposition, the interaction of internal stress concentrations due to fibers and voids is established theoretically and verified experimentally using photoelastic models. Test models are also employed to establish the strength of the material as influenced by porosity and matrix ductility. The results on fiber-void stress interaction and on the strength of brittle/ductile solids in combination with modified Hencky Von Mises Distortion Energy Criteria are used in formulating failure theories for composites subjected to transverse and shear loading. Test data from actual composites are used for final verification of the failure theories. Types of composites fabricated and tested in transverse tension and interlaminar shear include: glass epoxy, glass phenolic, graphite epoxy, graphite phenolic, and boron epoxy. The predicted transverse tensile strength of composites shows fair correlation with test data. For the composites subjected to shear loading, good correlation is obtained only between theory and test data obtained from torsion tests; the shear strength data obtained from the short-beam shear tests shows poor correlation with the theoretical prediction. Preliminary conclusions and recommendations are made on parameters influencing the transverse and shear strengths of composites and on how to improve these properties.

CONTENTS

Section 1	INTERNAL STRESSES IN FIBER-REINFORCED COMPOSITES		3
	1.1	Internal Stresses in Composites Subjected to Transverse Loading	3
	1.2	Internal Stresses in Composites Subjected to Inplane Shear Loading	4
	1.3	Test-Theory Comparison of Internal Stresses in Composite Models Subjected to Transverse Loading	4
Section 2	EFFECTIVE ELASTIC PROPERTIES OF SOLIDS CONTAINING VOIDS		13
	2.1	Young's Moduli of a Solid Containing Cylindrical Voids	13
	2.2	Shear Moduli of a Solid Containing Cylindrical Voids	14
	2.3	Poisson's Ratios of a Solid Containing Cylindrical Voids	16
	2.4	Experimental Studies on the Influence of Voids on the Young's Modulus of a Solid	16
Section 3	INTERNAL STRESSES IN SOLIDS CONTAINING VOIDS		25
	3.1	Theoretical Prediction of Internal Stresses from Transverse Loading	25
	3.2	Experimental Studies on Internal Stresses from Transverse Loading and Test-Theory Comparison	31
	3.3	Interr Stresses from Axial and Shear Loading	35
Section 4	STRESS INTERACTION FROM FIBERS AND VOIDS		
	4.1	Theoretical Studies on Fiber-Void Stress Interaction under Transverse Loading	45

	4.2	Experimental Studies on Fiber-Void Stress Interaction under Transverse Loading and Test-Theory Comparison	48
	4.3	Theoretical Studies on Fiber-Void Stress Interaction under Shear Loading	55
	4.4	Influence of Unbonded Fibers on Stress Concentrations in Composites Subjected to Transverse, Shear, or Axial Loading	55
Section 5		FAILURE CRITERIA FOR POROUS SOLIDS AND FOR COMPOSITES CONTAINING FIBERS, MATRIX, VOIDS, AND INEFFECTIVE FIBERS	59
	5.1	Strength of Brittle and Ductile Matrix as Influenced by Voids	59
	5.2	Transverse Tensile Strength of Composites	66
	5.3	Shear Strength of Composites	70
Section 6		FABRICATION AND TESTING OF ACTUAL COMPOSITES FOR VERIFICATION OF FAILURE THEORIES	75
	6.1	Matrix Materials and Their Properties	75
	6.2	Fiber Materials and Their Properties	76
	6.3	Fabrication of Composite Specimens	76
	6.4	Transverse Tensile Strength Data for Composites	83
	6.5	Interlaminar Shear Strength Data for Composites	90
Section 7		COMPARISON OF MEASURED TRANSVERSE TENSILE AND INTERLAMINAR SHEAR STRENGTH WITH MICROMECHANICS FAILURE THEORY PREDICTIONS	91
	7.1	Test-Theory Comparison of the Transverse Tensile Strength of Composites	91
	7.2	Test-Theory Comparison of the Interlaminar Shear Strength of Composites	95

Section 8	CONCLUSIONS AND RECOMMENDATIONS	111
Section 9	REFERENCES	115
Appendix A	STRESSES AND DEFORMATIONS OF POROUS SOLIDS	119
Appendix B	TEST DATA FOR PHOTOELASTIC TEST SPECIMENS	127
Appendix C	NUMERICAL EXAMPLES ON USE OF MICROMECHANICS FAILURE CRITERIA TO PREDICT THE TRANSVERSE TENSILE STRENGTH AND INTERLAMINAR SHEAR STRENGTH OF COMPOSITES	133
Appendix D	TEST DATA FOR RESIN CASTINGS AND FOR TRANSVERSE TENSILE AND INTERLAMINAR SHEAR STRENGTH OF ACTUAL COMPOSITES	139

ILLUSTRATIONS

Figure	Title	Page
1	General Study Approach	2
2	Mathematical Model for Investigating Interfiber Stresses in Composites	3
3	Internal Interfiber Stress Distribution in Composites Subjected to Transverse Loading	6
4	Influence of Fiber Content on the Internal Interfiber Stress Distribution in Composites Subjected to Transverse Loading	7
5	Transverse Young's Modulus of Composites as a Function of Properties of Constituents and Fiber Content	8
6	Interfiber Stress Distribution in Composites Subjected to Shear Loading	10
7	Photoelastic Test Specimen and Test-Theory Comparison of Internal Stresses in Composite Models	11
8	Mathematical Model for Determining Influence of Voids on Effective Elastic Properties of the Matrix	13
9	Young's Moduli of Solid Containing Cylindrical Voids	15
10	Shear Moduli of Solid Containing Cylindrical Voids	17
11	Poisson's Ratios of Solid Containing Cylindrical Voids	18
12	Test Specimens for Determining the Influence of Voids on Young's Modulus and Tensile Strength of Brittle Material (Homalite 100)	19
13	Typical Stress-Strain Curves for Homalite 100	20
14	Influence of Void Content on Young's Modulus of a Solid	24
15	Mathematical Model for Determining Internal Stresses Due to Transverse Loading	25
16	Internal Maximum Stresses in Solids Containing Cylindrical Voids and Subjected to Transverse Loading	28
17	Secondary Stresses in Solids Containing Cylindrical Voids and Subjected to Transverse Loading	29
18	Porous Solid Subjected to Biaxial Loading	31

19	Stress Concentrations in a Porous Solid Subjected to Biaxial Loading (Biaxial Stress Ratio of 1:1)	32
20	Stress Concentrations in a Porous Solid Subjected to Biaxial Loading (Biaxial Stress Ratio of 2:1)	33
21	Photoelastic Test Specimen for Determining Internal Stresses in a Solid with Cylindrical Voids	34
22	Photoelastic Fringe Pattern in Plates with Various Contents of Cylindrical Voids (Load P = 1, 220. 1 lb)	36
23	Overall View of the Photoelastic Fringe Pattern in Plates with Cylindrical Voids (Load P = 1, 220. 1 lb)	37
24	Test-Theory Comparison of Internal Stresses at Locations A and B	38
25	Test-Theory Comparison of Internal Stresses at Location C	39
26	Test-Theory Comparison of Internal Stresses at Locations D and E	40
27	Internal Stresses in Porous Solids Subjected to Loads in the Direction of Cylindrical Void Axis	41
28	Maximum Internal Shear Stresses in Solids Containing Cylindrical Voids	43
29	Idealized Model Composite Containing Fibers, Voids, and Matrix	46
30	Interaction of Stress Concentrations from Fibers and Voids in a Composite Subjected to Transverse Loading	47
31	Photoelastic Test Specimen for Determining Stress Interaction from Fibers and Voids	49
32	Photoelastic Test Setup for Determining Stress Interaction from Fibers and Voids	50
33	Photoelastic Fringe Pattern in Specimen 1 (k_v = 1. 01%, k_f = 40. 07%)	51
34	Photoelastic Fringe Pattern in Specimen 2 (k_v = 1. 37%, k_f = 54. 54%)	52
35	Interfiber Load Transfer in a Composite Containing Fibers, Voids, and Matrix	54
36	Interaction of Stresses from Fibers and Voids	56
37	Interaction of Stress Concentrations from Fibers and Voids in a Composite Subjected to Shear Loading	57

38	Photoelastic Fringe Patterns Due to Residual Stresses in Specimens with Various Void Contents	60
39	Typical Tensile Specimens with Voids. Specimen (a) Contains Residual Stresses; Specimen (b) is Free of Residual Stresses	61
40	Test-Theory Comparison of Tensile Strength of Brittle Matrix Containing Cylindrical Voids Arranged in Square Array	63
41	Test-Theory Comparison of Tensile Strength of Ductile Material Containing Cylindrical Voids Arranged in Square Array	64
42	Influence of Porosity on Tensile Strength of Ductile and Brittle Materials	65
43	Typical Theoretical Results for the Transverse Tensile Strength of Composites as Influenced by Porosity, Matrix Ductility, and Resin Strength	71
44	Typical Theoretical Results for the Shear Strength of Composites as Influenced by Porosity, Constituent Properties, Fiber Content, and Resin Shear Strength	73
45	Typical Stress-Strain Curve for Cast Epoxy 1004 Resin	79
46	Typical Stress-Strain Curve for Cast SC1008 Phenolic Resin	80
47	Typical Stress-Strain Curve for Cast and Post-Cured SC1008 Phenolic Resin	81
48	Test-Theory Comparison of Transverse Young's Modulus of Composites Made with S-Glass Fibers	92
49	Test-Theory Comparison of Transverse Young's Modulus of Composites Made with Graphite Fibers	93
50	Test-Theory Comparison of the Transverse Tensile Strength of Composites Made with Glass Fibers	96
51	Test-Theory Comparison of Transverse Tensile Strength of Composites Made with Graphite Fibers	97
52	Test-Theory Comparison of the Transverse Tensile Strength of Composites Made with S-Glass Fibers and Different Resins	98
53	Test-Theory Comparison of Shear Strength of Composites Made with Glass Fibers	99

54	Test-Theory Comparison of Shear Strength of Composites Made with Graphite Fibers	100
55	Test-Theory Comparison of Shear Strength of Glass- and Graphite-Fiber-Reinforced Composites	104
56	Assumed and Actual Stresses Acting on the Failure Plane in the Short-Beam Shear Test	105
57	Influence of Combined Loading on Shear Strength	107
58	Comparison of Predicted Shear Strength with Test Data Obtained from Solid Rod Torsion Test	108
A-1	Solid Containing a Square Array of Cylindrical Voids	120
A-2	Plate with a Single Hole	121

TABLES

Table		Page
1	Normalized Interfiber Stresses in Composites Subjected to Transverse Loading	5
2	Normalized Interfiber Shear Stresses in Unidirectional Composites	9
3	Properties of Homalite 100	21
4	Mechanical Properties on Tensile Specimens Containing Voids	23
5	Test-Theory Correlation of Fiber-Void Stress Interaction	53
6	Average Properties of Resins	77
7	Influence of Strain Gages on the Tensile Strength of Resin	78
8	Reinforcing Fibers and Their Properties	82
9	Processing Variables in Composite Panel Fabrication	84
10	Average Properties of Glass Epoxy and Glass Phenolic Composites	86
11	Average Properties of Graphite Epoxy and Graphite Phenolic Composites	87
12	Average Properties of Boron Epoxy Composites	88
13	Ineffective Fiber Contents for Composites Made with Glass and Graphite Fibers	102
14	Properties of Shell EPON 828/1031 MNA/BDMA Epoxy Resin	109
B-1	Strains and Stress Concentrations in a Perforated Plate with $(R/\ell) = 0.252$ ($k_v = 4.94\%$)	129
B-2	Strains and Stress Concentrations in a Perforated Plate with $(R/\ell) = 0.358$ ($k_v = 10.07\%$)	130
B-3	Strains and Stress Concentrations in a Perforated Plate with $(R/\ell) = 0.437$ ($k_v = 15.0\%$)	130
B-4	Strains and Stress Concentrations in a Perforated Plate with $(R/\ell) = 0.505$ ($k_v = 20.0\%$)	131
B-5	Strains and Stress Concentrations in a Perforated Plate with $(R/\ell) = 0.619$ ($k_v = 30.1\%$)	131

B-6	Experimental Results on Internal Stresses in a Composite Model Consisting of Fibers, Voids, and Matrix	132
D-1	Test Data for 1004 Epoxy and SC1008 Phenolic	141
D-2	Test Data for Glass Epoxy Composites	142
D-3	Test Data for Glass Phenolic Composites	143
D-4	Test Data for Graphite Epoxy and Graphite Phenolic Composites	144
D-5	Test Data for Boron Epoxy Composites	145

NOMENCLATURE

σ_T, τ_{LT}	=	External stresses acting on a fiber-reinforced composite
σ_1, σ_2, σ_3, σ_{13}	=	External stresses acting on a porous solid
σ_x, σ_y, σ_z, τ_{xz}	=	Internal stresses in the matrix of a fiber-reinforced composite or in the matrix of a porous solid
$p - q$	=	Difference between principal stresses
$\tilde{\sigma}_x$, $\tilde{\sigma}_y$	=	Stresses in a porous solid subjected to biaxial loading
σ_x^*, σ_y^*, σ_z^*, τ_{xz}^*	=	Internal stresses in a solid containing fibers, voids, and matrix
P	=	Load
K_x, K_y, K_z	=	Triaxial stress concentrations in the matrix of a fiber-reinforced composite
K_{xn}, K_{yn}, K_{zn}, K_{xzn} (n = A, B, C, D, E)	=	Stress concentrations at locations n in a solid with voids
K_{xn}^*, K_{yn}^*, K_{zr}^* (n = A, D)	=	Stress concentrations due to voids in the matrix of a fiber-reinforced composite (K_{xn}^*, K_{yn}^*, $K_{zr}^* = f(\lambda^*)$)
K_x^*, K_y^*, K_z^*	=	Stress concentrations due to fibers evaluated for E_f/E_r^*, where E_r^* is the effective Young's modulus of resin with voids.
σ_r, σ_o, σ_{tr}	=	Tensile strength of material or resin
σ_{cr}	=	Ultimate compressive strength of resin
τ_r	=	Shear strength of resin
σ_T^*, τ_{LT}^*	=	Transverse tensile and shear strengths, respectively, of composites containing fibers, matrix, voids, and ineffective fibers
E_1, E_2, E_3	=	Young's moduli of solids containing cylindrical voids
G_{13}, G_{12}, G_{23}	=	Shear moduli of solids containing cylindrical voids

ν_{12}, ν_{23}, ν_{31} = Poisson's ratios of solids containing cylindrical voids

E_f = Young's modulus of fibers

E_r = Young's modulus of resin

G_f = Shear modulus of fibers

G_r = Shear modulus of resin

ν_f = Poisson's ratio of fibers

ν_r = Poisson's ratio of resin

E_T = Transverse Young's modulus of composite

R = Fiber radius or void radius

2ℓ = Fiber or void spacing

λ = $R/\ell = \sqrt{4k_v/\pi}$ (Nondimensional void spacing)

λ^* = Nondimensional void spacing in a composite (see Equation 29).

k_v = Volume fraction of cylindrical voids in a solid $k_v = \pi\lambda 2/4$

k_{vc} = Void content in a fiber-reinforced composite

k_f = Apparent fiber volume fraction of composite (Equation 43)

$\bar{k}_f$ = True fiber volume fraction of composite (Equation 48)

k_{if} = Apparent volume fraction of ineffective fibers in a composite

$\bar{k}_{if}$ = True volume fraction of ineffective fibers in a composite

ξ = See Equation 19

ξ^* = Same as ξ except evaluated for λ^* rather than λ

x, y, z, 1, 2, 3 = Cartesian coordinates

L = Denotes fiber direction

T = Denotes transverse direction (normal to L direction)

INTRODUCTION

The ability to design reliably with advanced composites has been hampered by a lack of experimentally verified micromechanics failure criteria for predicting the strength of composites from the properties of the constituents and the composite's microstructure. Because such criteria are not available, extensive testing must now be performed to generate the mechanical properties data for composites. Lowest test values are generally selected for design allowables, which frequently leads to overdesign and weight penalties. Due to the high degree of scatter in test data, the generation of reliable design allowables requires an extensive amount of testing, which is both time consuming and expensive. Although the "make it" and "break it" approach sufficed up to now, the present emphasis on cost effectiveness, increased reliability, and improved performance of composites points out the need for micromechanics failure criteria.

The theoretical and experimental studies presented in this report are oriented towards this objective, that is, formulation of micromechanics failure criteria for predicting the transverse and shear strengths of composites from the properties of constituents - fibers and matrix - and the composite's microstructure. The general study approach employed in the formulation of a micromechanics failure theory is summarized in Figure 1 for the case of composites subjected to transverse loading. A similar approach is used to formulate a shear strength failure theory for composites.

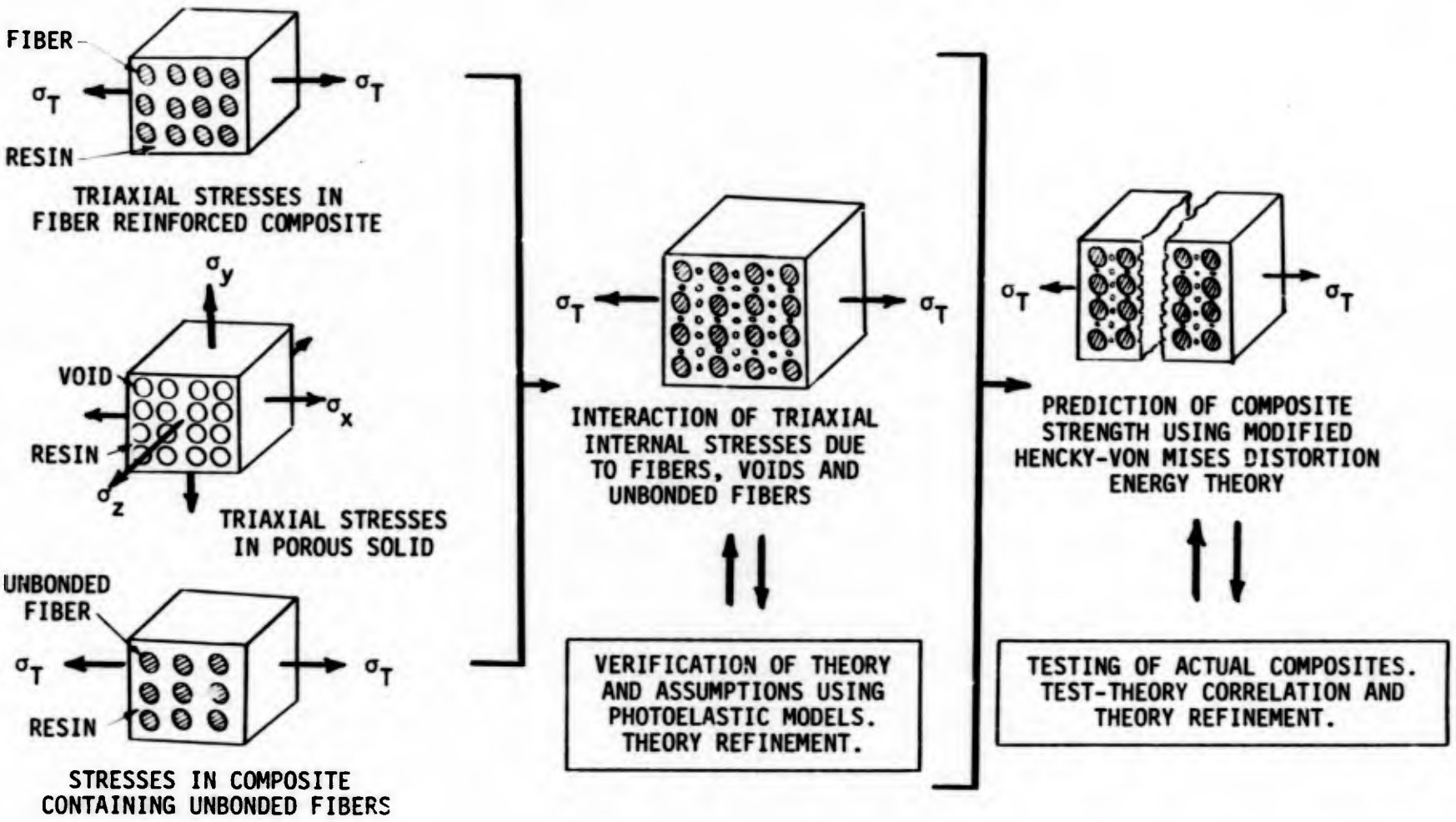

Figure 1. General Study Approach

Section 1

INTERNAL STRESSES IN FIBER-REINFORCED COMPOSITES

In accordance with the general study approach presented in Figure 1, the first step in the development of the micromechanics failure criteria for composites subjected to transverse and shear loading involves the determination of internal stresses in composites consisting of fibers and matrix. These internal stresses were determined using an existing approximate theory presented in Reference 1. Reference 1 contains an approximate solution for the internal triaxial stresses in composites consisting of a matrix reinforced by circular fibers arranged in a square array. Solutions are given therein for the principal elastic constants of unidirectional composites and for the internal stresses in composites subjected to axial loading (in the fiber direction), transverse loading (normal to the fiber direction), and inplane shear loading. The accuracy of the solutions presented in Reference 1 has been verified by comparing the results with results obtained from the closed-form rigorous elasticity solutions (Reference 2), results obtained from numerical computer solutions based on rigorous elasticity theory (References 3, 4, and 5), and experimental results obtained from photoelastic models (see Subsection 1.3).

1.1 INTERNAL STRESSES IN COMPOSITES SUPJECTED TO TRANSVERSE LOADING

The mathematical model used in Reference 1 for investigating the internal triaxial stresses in a composite subjected to transverse loading is shown in Figure 2.

CR84

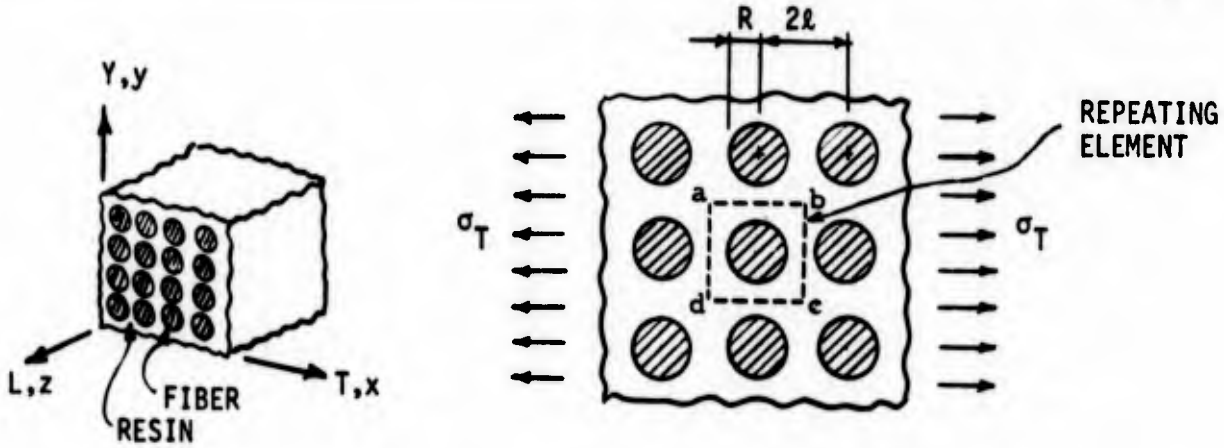

Figure 2. Mathematical Model for Investigating Interfiber Stresses in Composites

Numerical results, based on the theory of Reference 1, are presented in Table 1 and in Figures 3 and 4. Table 1 shows the triaxial stress concentrations in composites consisting of various combinations of fiber and matrix materials. The variables are the Young's moduli of the fibers and the matrix, and the fiber volume fraction. The triaxial stresses shown in Table 1 are at a point of maximum stress concentration. Figure 3 shows the distribution of triaxial stresses midway between the fibers for composites subjected to transverse loading. The results presented there are for composites with different E_f/E_r ratios and containing 55 percent reinforcement by volume. Figure 4 shows the stress distribution with $E_f/E_r = 100$ and containing various amounts of reinforcement. Inasmuch as determining the volume fraction of ineffective fibers (see Section 7) requires that the theoretical values of the transverse Young's modulus of composite must be known, the latter have been calculated from the results given in Reference 1 and are shown in Figure 5.

1.2 INTERNAL STRESSES IN COMPOSITES SUBJECTED TO INPLANE SHEAR LOADING

For a composite, such as that shown in Figure 2, subjected to inplane shear stress τ_{LT}, the interfiber shear stress concentrations calculated from theory given in Reference 1 are presented in Table 2. As in the previous section, the stress concentrations are given for composites made of fibers and resins having different shear moduli and containing various amounts of fiber reinforcement. Typical shear stress distribution on the boundary of a repeating element is shown in Figure 6. The variable in Figure 6 is the fiber-to-matrix shear modulus ratio.

1.3 TEST-THEORY COMPARISON OF INTERNAL STRESSES IN COMPOSITE MODELS SUBJECTED TO TRANSVERSE LOADING

The theoretical results presented in Subsection 1.1 have been partially verified with test data from photoelastic composite models (Reference 1). For completeness, the test-theory comparison reported in Reference 1 is presented here. The photoelastic models consisted of plates containing nine circular aluminum inclusions arranged in a square array and embedded in 4290 Hysol epoxy resin. Volume fractions of the inclusions ranged from k=50.2 percent to k=65 percent. Each plate with inclusions was subjected to tensile stresses along its principal axis. Two-dimensional photoelastic oblique incidence technique was used to measure the stresses across the sections of

Table 1.

NORMALIZED INTERFIBER STRESSES IN COMPOSITES SUBJECTED TO TRANSVERSE LOADING

	k_f = 40%			k_f = 55%			k_f = 70%			k_f = 75%			k_f = 78%		
E_f/E_r	K_x	K_z	K_y	K_x	K_z	K_y	K_x	K_z	K_y	K_x	K_z	K_y	K_x	K_z	K_y
5	1.464	0.619	0.633	1.434	0.645	0.651	1.410	0.661	0.663	1.405	0.666	0.666	1.403	0.669	0.668
10	1.595	0.762	0.770	1.602	0.793	0.794	1.652	0.837	0.833	1.686	0.859	0.854	1.713	0.876	0.870
20	1.669	0.847	0.851	1.727	0.893	0.893	1.908	0.999	0.995	2.036	1.070	1.064	2.148	1.132	1.125
40	1.705	0.892	0.894	1.805	0.953	0.953	2.136	1.136	1.133	2.425	1.292	1.287	2.740	1.462	1.456
100	1.725	0.918	0.919	1.859	0.993	0.993	2.349	1.259	1.257	2.900	1.555	1.553	3.778	2.028	2.024
200	1.731	0.926	0.927	1.877	1.007	1.007	2.441	1.311	1.310	3.163	1.700	1.698	4.697	2.525	2.522
400	1.733	0.931	0.931	1.887	1.014	1.014	2.493	1.341	1.340	3.332	1.792	1.791	5.597	3.012	3.010

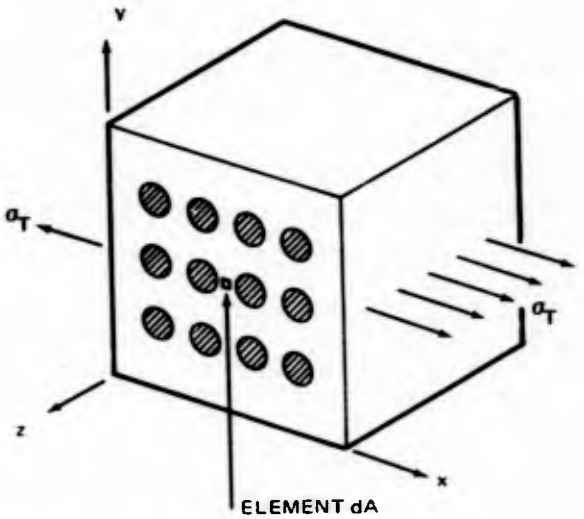

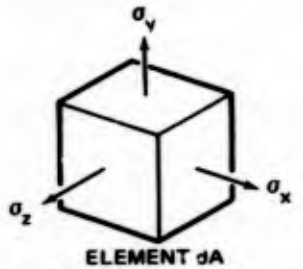

$K_x = \sigma_x/\sigma_T$

$K_y = \sigma_y/\sigma_T$

$K_z = \sigma_z/\sigma_T$

E_f = Young's modulus of fibers

E_r = Young's modulus of resin

k_f = Fiber volume fraction

σ_x, σ_y, σ_z = Stresses in the resin

σ_T = Remotely applied stress

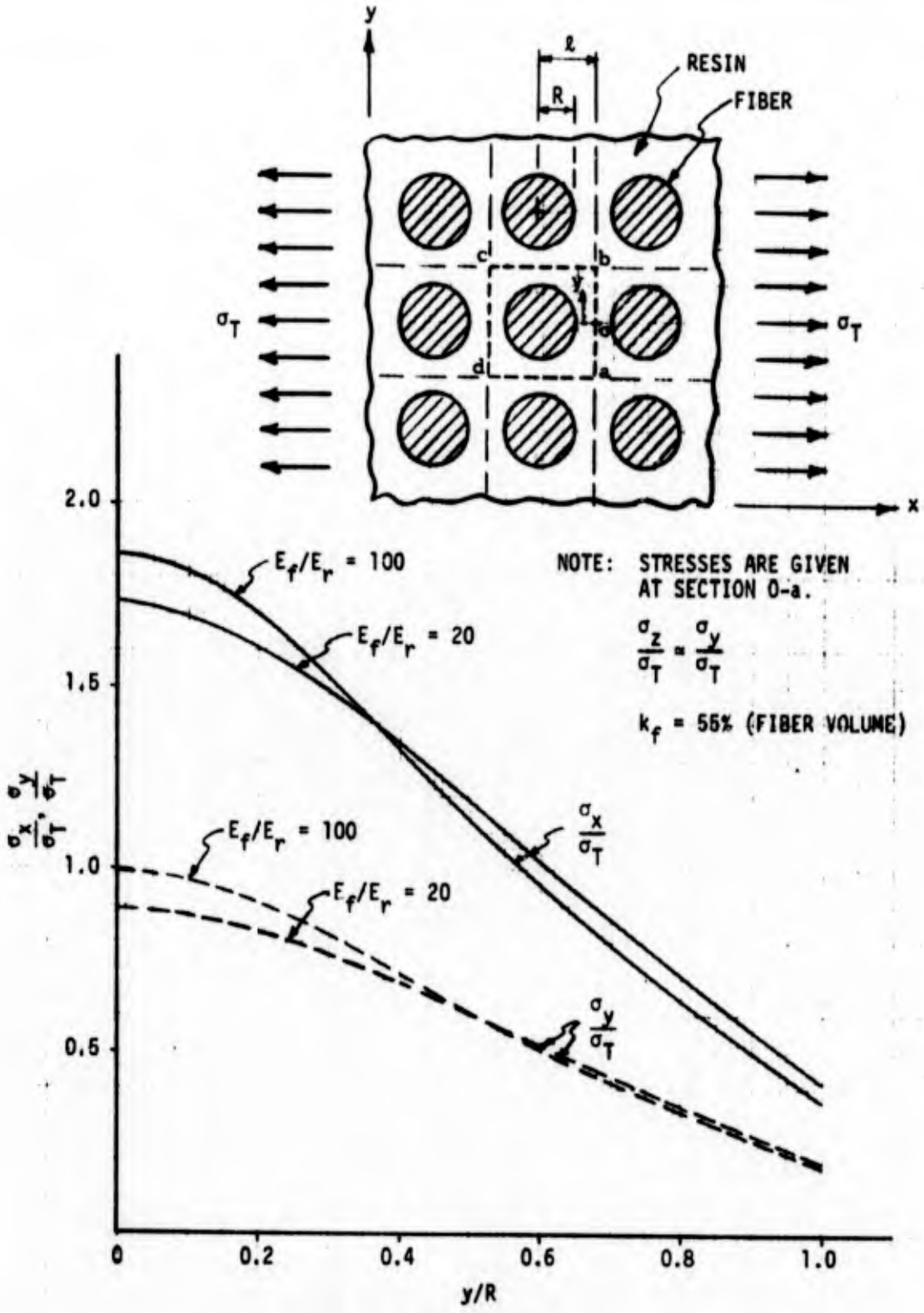

Figure 3. Internal Interfiber Stress Distribution in Composites Subjected to Transverse Loading

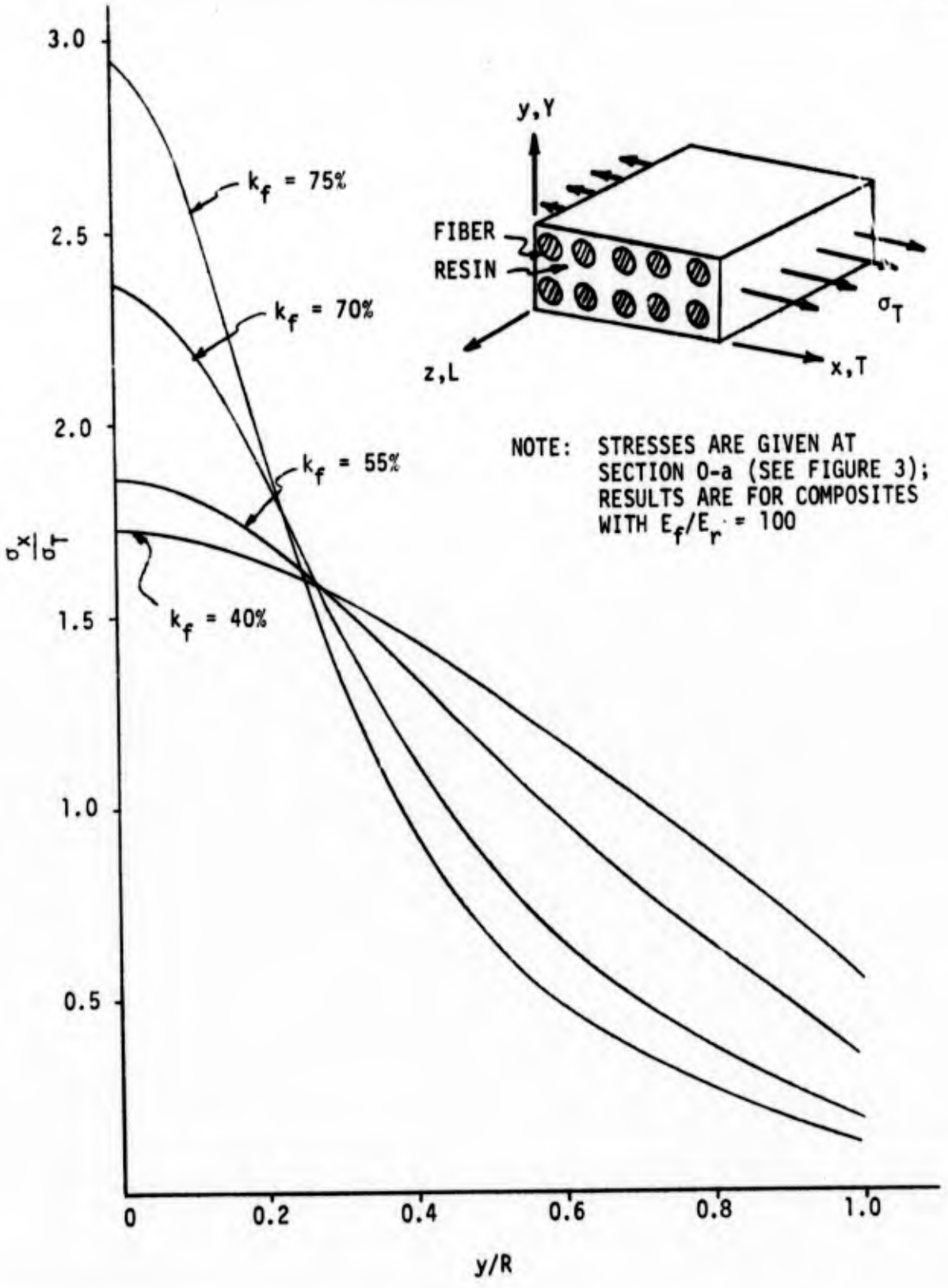

Figure 4. Influence of Fiber Content on the Internal Interfiber Stress Distribution in Composites Subjected to Transverse Loading

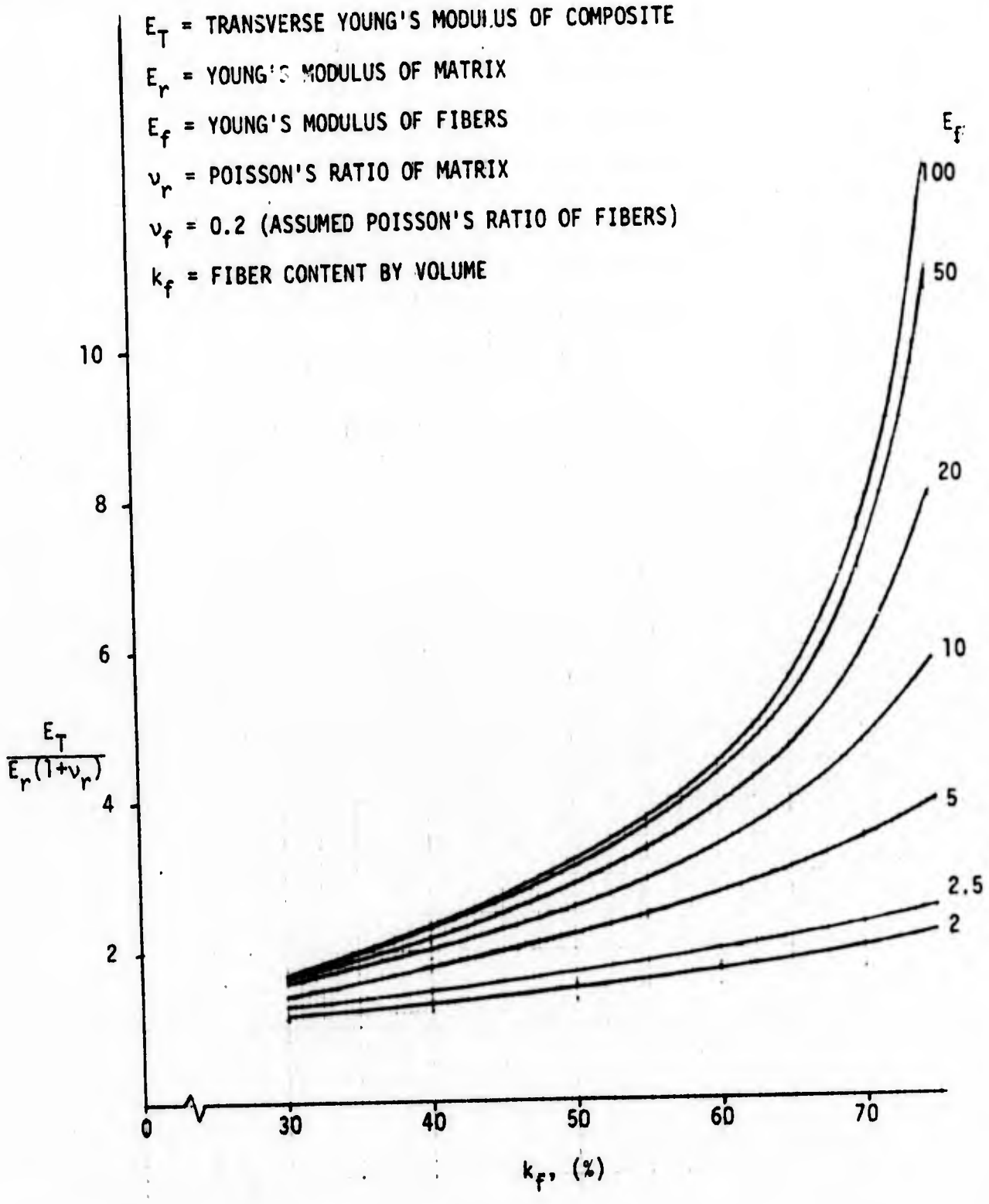

Figure 5. Transverse Young's Modulus of Composites as a Function of Properties of Constituents and Fiber Content

Table 2.

NORMALIZED INTERFIBER SHEAR STRESSES IN UNIDIRECTIONAL COMPOSITES

$\frac{G_f}{G_r}$	k_f = 40%		k_f = 55%		k_f = 70%		k_f = 75%		k_f = 78%	
	$\frac{\tau_M}{\tau_{LT}}$	$\frac{\tau_m}{\tau_{LT}}$	$\frac{\tau_M}{\tau_{LT}}$	$\frac{\tau_m}{\tau_{LT}}$	$\frac{\tau_M}{\tau_{LT}}$	$\frac{\tau_m}{\tau_{LT}}$	$\frac{\tau_M}{\tau_{LT}}$	$\frac{\tau_m}{\tau_{LT}}$	$\frac{\tau_M}{\tau_{LT}}$	$\frac{\tau_m}{\tau_{LT}}$
5.63	1.44	0.69	1.48	0.55	1.54	0.42	1.57	0.38	1.60	0.35
11.27	1.54	0.63	1.63	0.47	1.81	0.32	1.92	0.26	2.02	0.23
22.5	1.60	0.60	1.74	0.42	2.06	0.25	2.31	0.19	2.58	0.16
45.0	1.63	0.58	1.80	0.40	2.25	0.22	2.70	0.15	3.31	0.11
112.5	1.65	0.57	1.84	0.39	2.41	0.20	3.10	0.13	4.49	0.07
225.0	1.66	0.57	1.85	0.38	2.47	0.19	3.29	0.12	5.40	0.06
450.0	1.66	0.57	1.86	0.38	2.51	0.18	3.41	0.11	6.19	0.05
1127.0	1.67	0.57	1.87	0.38	2.53	0.18	3.48	0.11	6.89	0.04

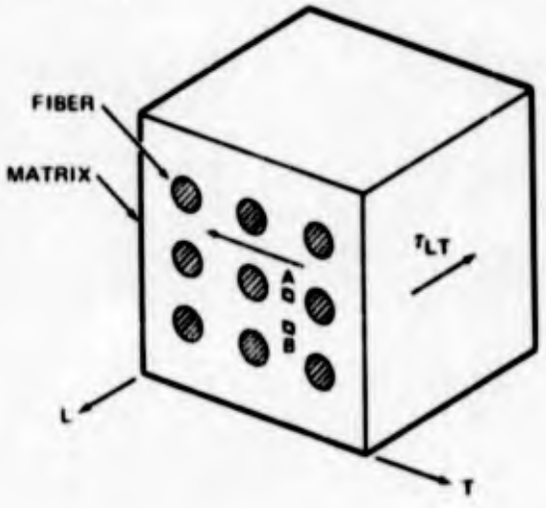

τ_M - Maximum shear stress (at Point "A")

τ_m - Shear stress (at Point "A")

τ_{LT} - Remotely applied shear stress

G_f - Shear modulus of fiber

G_r - Shear modulus of resin

k - Fiber volume fraction

symmetry, midway between the inclusions. Figure 7 shows the photoelastic model, photoelastic fringe pattern in the model subjected to tensile loading, and the test-theory comparison of the interfiber stresses in models with inclusion contents of k_f=50.2 percent and k_f=65 percent. The stress-state (σ_x) in a two-dimensional model has been shown to be an accurate representation for the corresponding internal stress in a three-dimensional composite Reference 1.

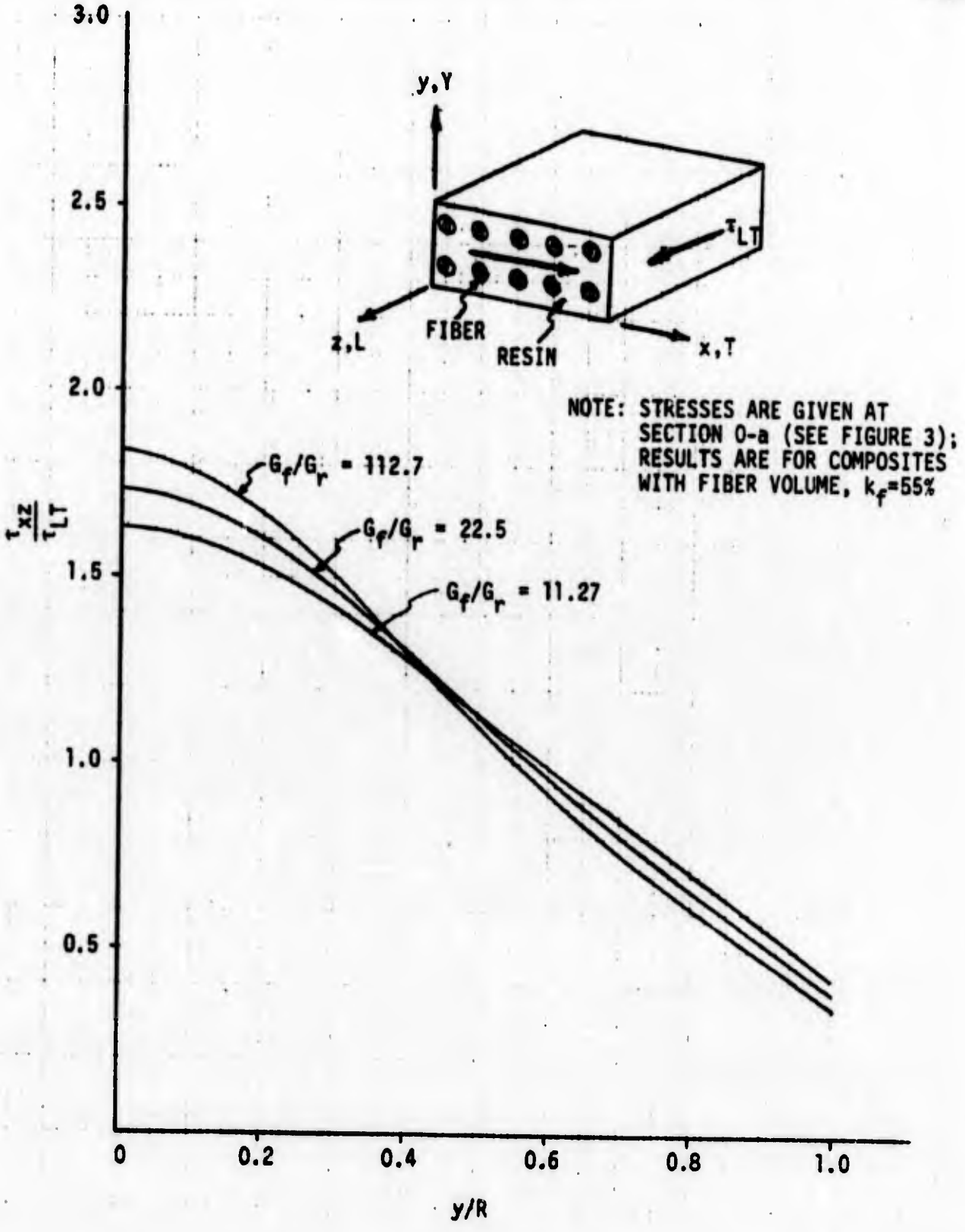

Figure 6. Interfiber Stress Distribution in Composites Subjected to Shear Loading

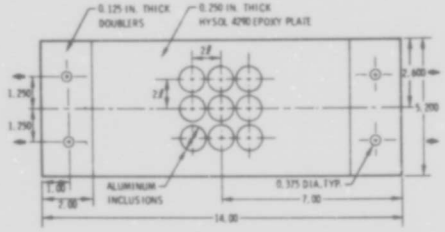

PHOTOELASTIC MODEL
(a)

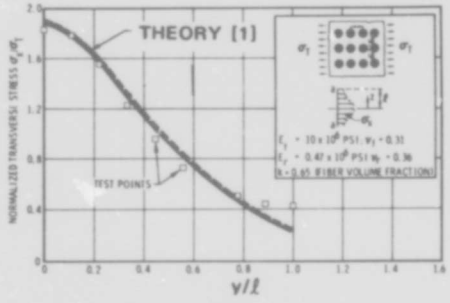

TEST-THEORY COMPARISON OF INTERFIBER STRESSES IN A PLATE WITH k_f = 65%
(c)

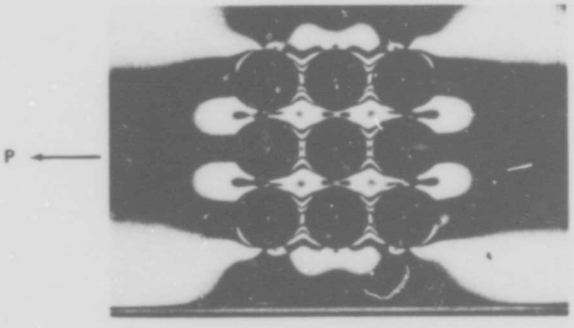

FRINGE PATTERN IN PHOTOELASTIC MODEL SUBJECTED TO TRANSVERSE TENSION
(b)

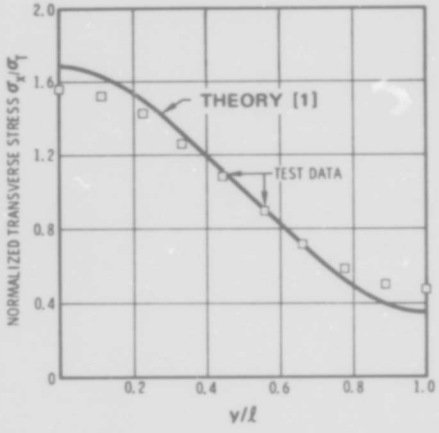

TEST-THEORY COMPARISON OF INTERFIBER STRESSES IN A PLATE WITH k_f = 50.2%
(d)

Figure 7. Photoelastic Test Specimen and Test-Theory Comparison of Internal Stresses in Composite Models

Section 2

EFFECTIVE ELASTIC PROPERTIES OF SOLIDS CONTAINING VOIDS

Microscopic observations of actual composites show that the voids within the matrix of such composites are primarily of cylindrical, or nearly cylindrical shape. To establish how such voids influence the deformations and strength of composites necessitated that a theory be developed for predicting the approximate elastic properties and stress concentrations in solids containing voids. The influence of voids on effective elastic properties of the matrix is presented here, while Section 3 gives the theoretical and experimental results on stress concentrations caused by voids.

The mathematical model selected for establishing approximately the influence of voids on elastic properties of the matrix is shown in Figure 8. The voids are assumed to be cylindrical in shape and arranged in a square array.

CR84

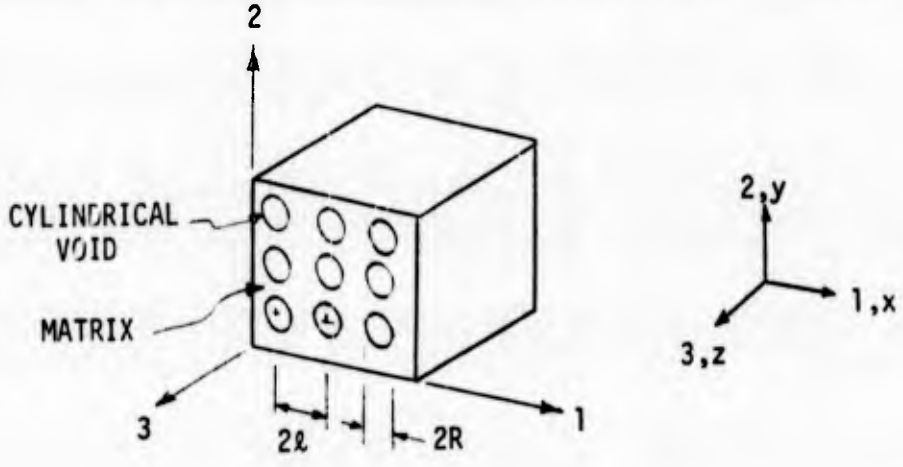

Figure 8. Mathematical Model for Determining Influence of Voids on Effective Elastic Properties of the Matrix

2.1 YOUNG'S MODULI OF A SOLID CONTAINING CYLINDRICAL VOIDS

The derivation of Young's modulus in Direction 1 is given in Appendix A. The final approximate expression for E_1 is

$$E_1 = \frac{E}{\left[\frac{2}{\sqrt{1-\lambda^2}} \tan^{-1}\sqrt{\frac{1+\lambda}{1-\lambda}} - \frac{\pi}{2} + \frac{1-\lambda}{1-\frac{\pi}{4}\lambda^2}\right]} \qquad (1)$$

where E is the Young's modulus of the void-free solid,

$$\lambda = R/\ell$$

and R and ℓ are defined in Figure 8. The term λ is related to volume fraction of voids, k_v, by the following

$$\lambda = \sqrt{\frac{4k_v}{\pi}} \tag{2}$$

or conversely,

$$k_v = \frac{\pi}{4}\lambda^2 \tag{3}$$

For a square array of voids, the Young's modulus associated with Direction 2 is given by Equation 1, that is $E_1 \equiv E_2$. The Young's modulus in Direction 3 can readily be obtained from the law of mixtures and is

$$E_3 = (1 - \frac{\pi}{4}\lambda^2)\, E \tag{4}$$

The variation of E_1 and E_3 as a function of λ is shown in Figure 9.

2.2 SHEAR MODULI OF A SOLID CONTAINING CYLINDRICAL VOIDS

The approximate expression for the shear modulus associated with Direction 1-3 can be obtained by using the same approach as was used to determine E_1. The expression for G_{13} is

$$G_{13} = \frac{G}{\left[\frac{2}{\sqrt{1-\lambda^2}} \tan^{-1}\sqrt{\frac{1+\lambda}{1-\lambda}} + 1 - \lambda - \frac{\pi}{2}\right]} \tag{5}$$

It is noted here that for the void array shown in Figure 8

$$G_{13} \equiv G_{23}$$

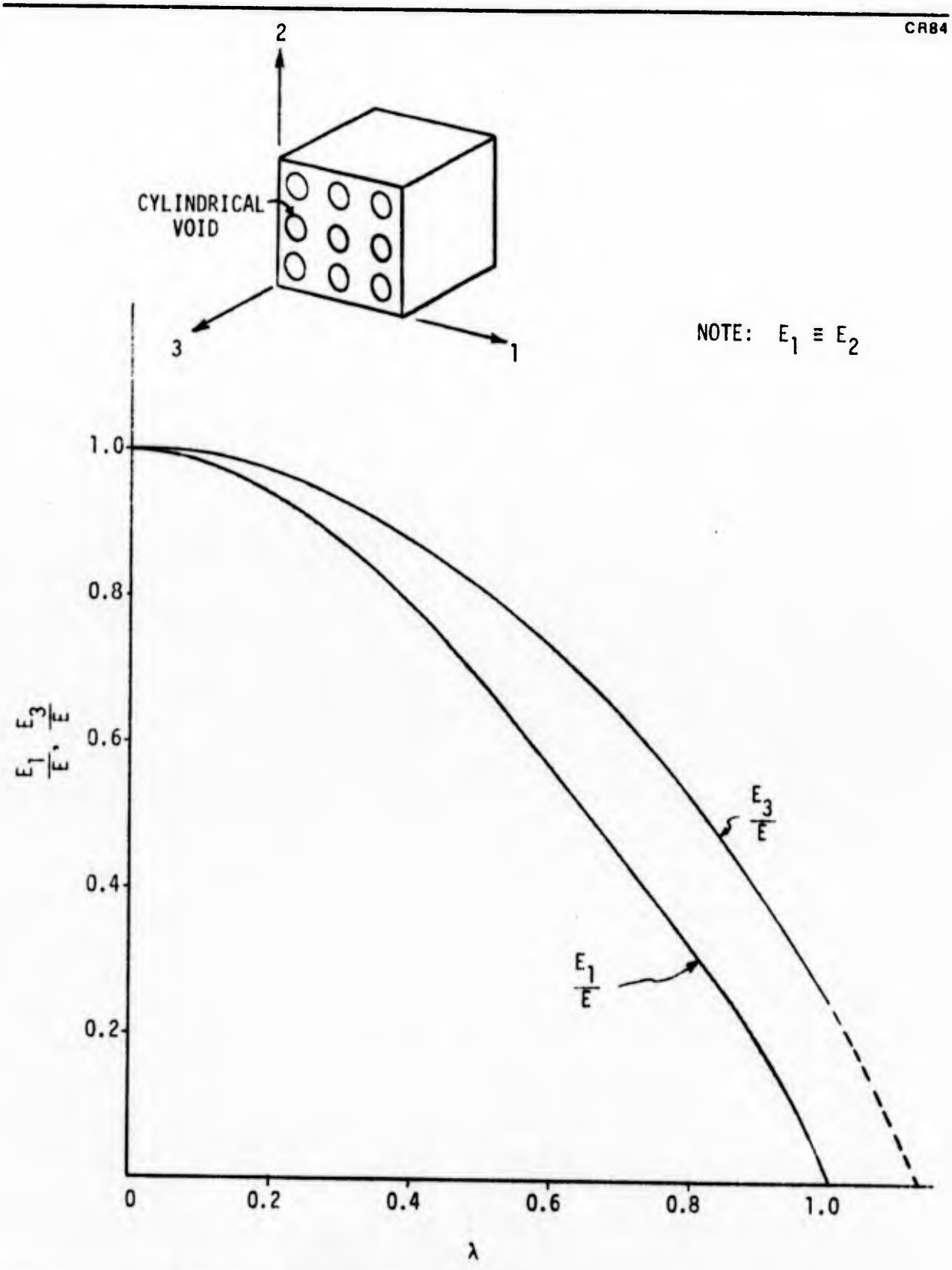

Figure 9. Young's Moduli of Solid Containing Cylindrical Voids

The shear modulus G_{12} associated with Direction 1-2 can be obtained from curves given in References 2 and 6 or from the following approximate expression

$$G_{12} \approx \frac{G(1+\nu)}{\left[\frac{2}{\sqrt{1-2\lambda^2}} \tan^{-1}\sqrt{\frac{1+\sqrt{2}\lambda}{1-\sqrt{2}\lambda}} - \frac{\pi}{2} + \frac{1-\sqrt{2}\lambda}{1-\frac{\pi}{2}\lambda^2}\right]\left[1+\nu\left(1-\frac{\pi}{2}\lambda^2\right)\right]} \tag{6}$$

where, in addition to previously defined terms, G and ν are the shear modulus and Poisson's ratio, respectively, of a void-free material. Equation 6 gives identical results to those given in Reference 2 in the region $\lambda \leq 0.65$, which is the region of interest. The variation of G_{13} and G_{12} as a function of λ is shown in Figure 10.

2.3 POISSON'S RATIOS OF A SOLID CONTAINING CYLINDRICAL VOIDS

As a first approximation, the Poisson's ratio ν_{31} can be obtained from the law of mixtures and is

$$\nu_{31} = \nu\left(1 - \frac{\pi}{4}\lambda^2\right) \tag{7}$$

The Poisson's ratio ν_{12} can be evaluated numerically from the results given in Section 3, or obtained from Reference 2. Figure 11 shows the variation of Poisson's ratios as a function of void spacing. The remaining Poisson's ratios, $\nu_{13} = \nu_{23}$, can be obtained from Maxwell's Reciprocity Theorem.

2.4 EXPERIMENTAL STUDIES ON THE INFLUENCE OF VOIDS ON THE YOUNG'S MODULUS OF A SOLID

To establish the influence of voids on the transverse Young's modulus E_1 of a solid, test specimens shown in Figure 12 were fabricated and tested in tension. Similar type of specimens were used, as described in Section 5, to determine the influence of voids on the tensile strength of a material. The material used in the preparation of these specimens was Homalite 100, which exhibits brittle behavior in tension, as shown in Figure 13. Additional test data for Homalite 100 is shown in Table 3. The results shown in Figure 13 and in Table 3 were obtained from conventional dog-bone tensile specimens similar to those shown in Figure 12. To ensure the accuracy of the test data,

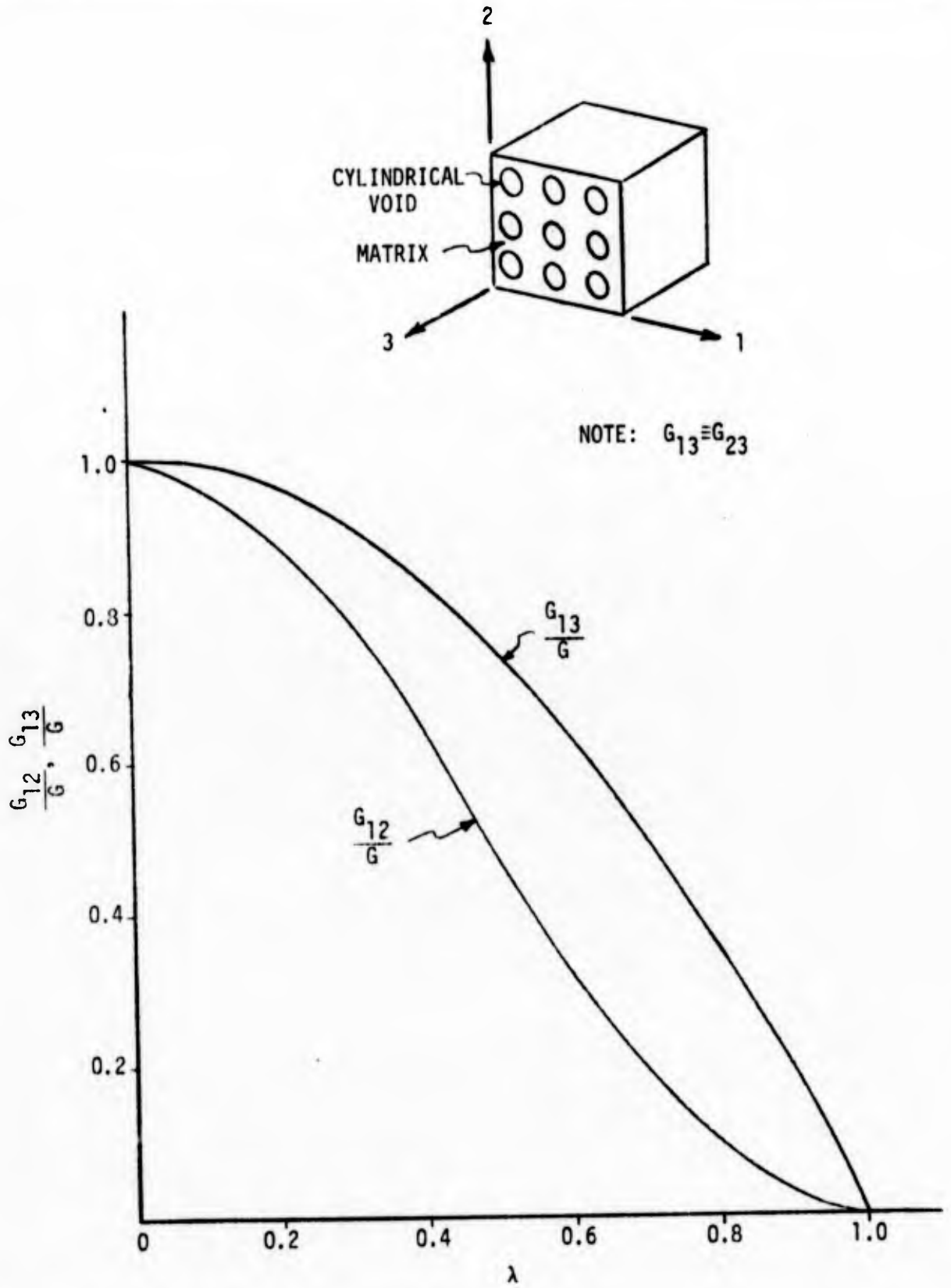

Figure 10. Shear Moduli of Solid Containing Cylindrical Voids

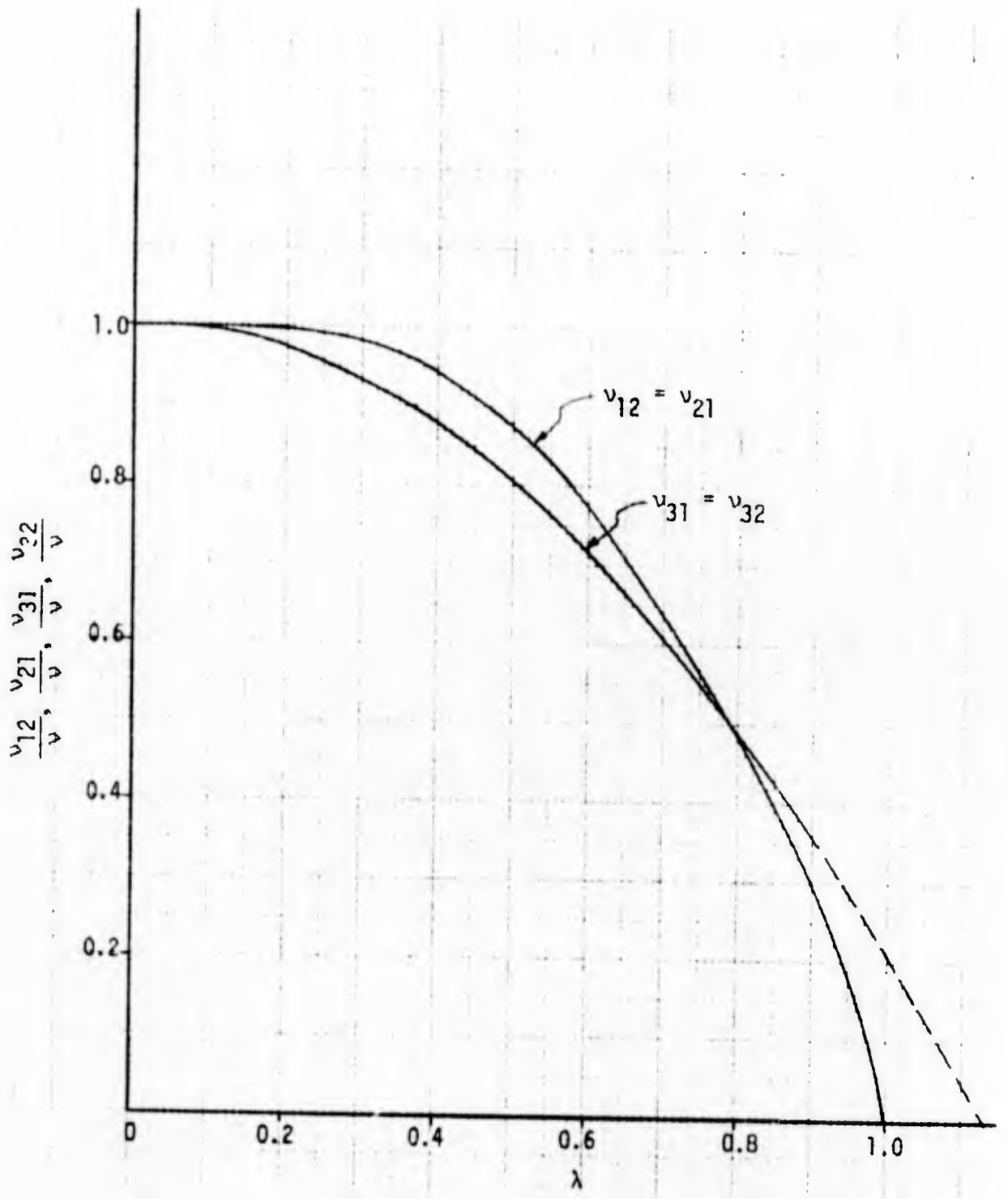

Figure 11. Poisson's Ratios of Solid Containing Cylindrical Voids

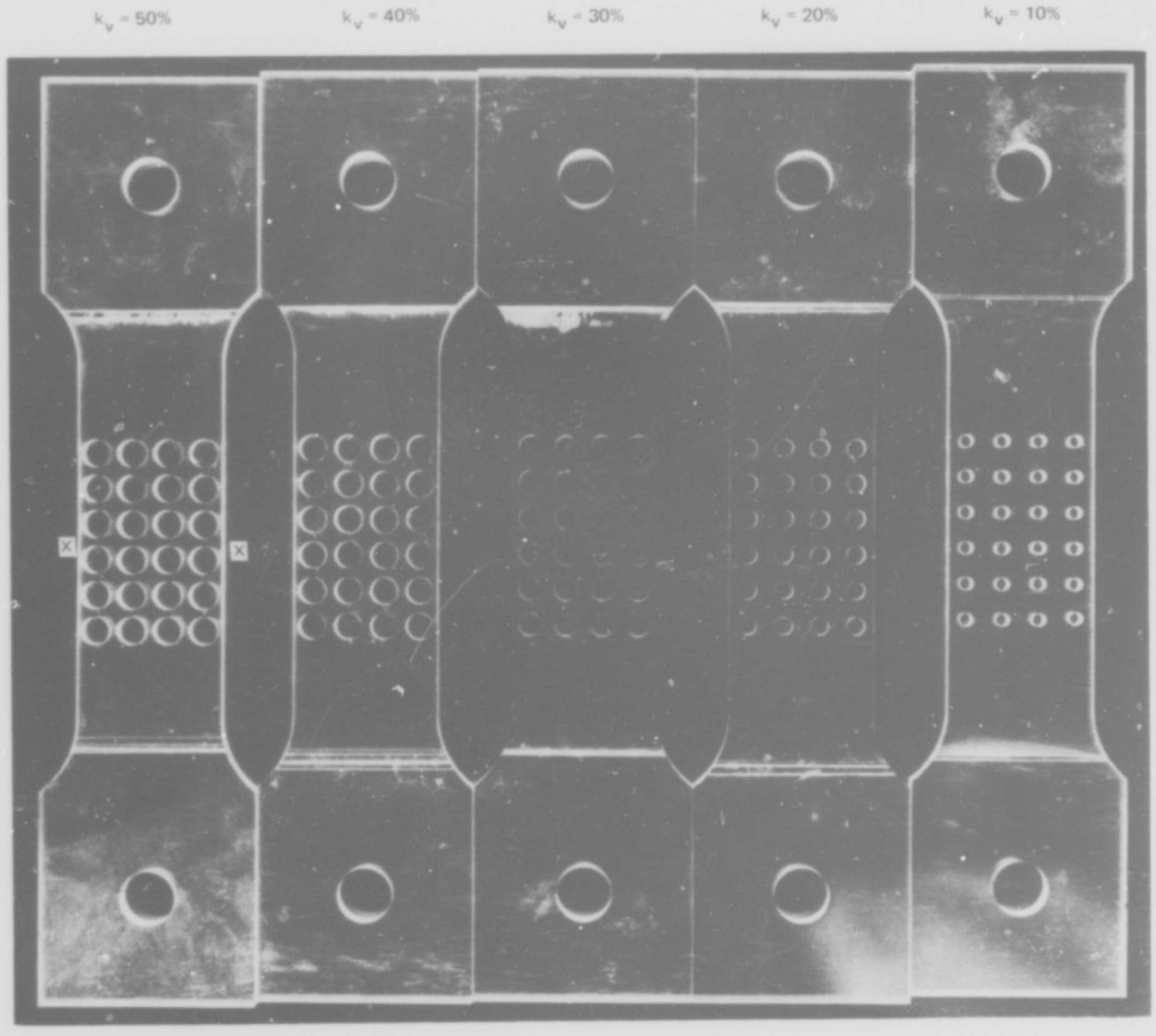

Figure 12. Test Specimens for Determining the Influence of Voids on Young's Modulus and Tensile Strength of Brittle Material (Homalite 100)

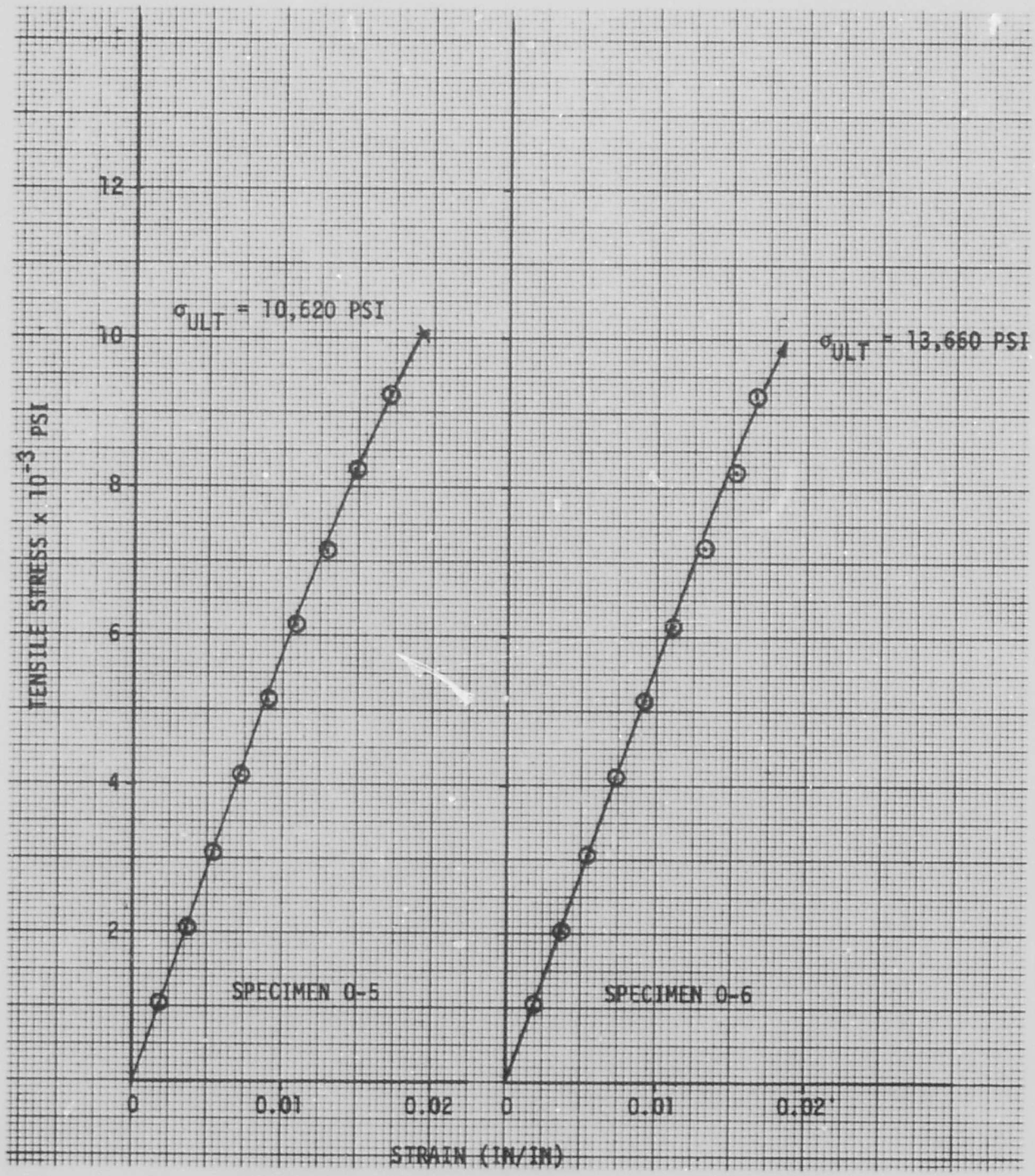

Figure 13. Typical Stress-Strain Curves for Homalite 100

TABLE 3

PROPERTIES OF HOMALITE 100

SPECIMEN DESIGNATION	POISSON'S RATIO	YOUNG'S MODULUS X 10^{-3} psi		TENSILE STRENGTH X 10^{-3} psi (1)	REMARKS ON FAILURE TYPE AND LOCATION (2)
		FROM STRAIN GAGES	FROM EXTENSO-METER		
0-1	0.356	610	597	(4.91)	S
0-2	0.348	629		(4.42)	S
0-3	0.337	637		(6.55)	S
0-4	---	585		(5.85)	S
0-5	---		576	10.62	T.S
0-6	---		570	13.66	T.S
0-7	---		576	(7.33)	pin
0-8	---		611	(7.37)	pin
0-9	---			11.63	T.S
0-10	---			9.81	T.S
0-11	---			10.78	T.S
AVERAGE	0.347	615	586	11.31	
		600			

(1) Data in parenthesis not used in average; strength data not valid, as described below.
(2) T.S - denotes failure of specimen in test section; S - specimens were instrumented with strain gages which influenced ultimate tensile strength.

two different methods were employed to measure the tensile strains used in calculating the Young's moduli of the specimens shown in Figure 12: Lightweight Instron extensometer and strain gages. The extensometer was mounted on the flat side of the specimen, with the extensometer's knife edges located approximately midway between the two adjacent rows of holes. In addition to the above method several specimens were also instrumented with two 0.75-inch-long strain gages mounted on each side of the tensile coupon (shown by x's in Figure 12). The nominal void contents in the tensile coupons ranged from 10 to 50 percent. Table 4 contains the description of the various specimens as well as the experimental results for the Young's moduli and tensile strength of specimens with various void contents. The specimens with a letter R in the specimen designation contained residual stresses produced during drilling of the holes, as shown in Figures 38 and 39 of Section 5. By modifying the drill feed rates and using coolants it was possible to produce specimens with holes that were free of residual stresses, as also shown in Section 5. All the specimens without the letter R in the specimen designation were free of any residual stresses.

Figure 14 compares the measured Young's moduli of specimens with voids with the theoretical results predicted from Equation 1. It is noted here that residual stresses are not expected to influence Young's modulus in the elastic range, therefore all the test data from Table 4 are plotted in Figure 14. The test-theory correlation shown in Figure 14 establishes the accuracy of Equation 1.

Although it would be desirable to verify experimentally the other properties of solids with voids (E_3, G_{13}, G_{12}, ν_{12}, ν_{31}), no such tests were planned for the present program.

TABLE 4

MECHANICAL PROPERTIES ON TENSILE SPECIMENS CONTAINING VOIDS

SPECIMEN DESIGNATION	HOLE DIAMETER 2R (in.) (1)	$\lambda = R/\ell$	k_v(%)	YOUNG'S MODULUS X 10^{-3} psi		TENSILE STRENGTH X 10^{-3} psi	REMARKS (2)
				FROM STRAIN GAGES	FROM EXTENSO-METER		
1-2	0.086	0.344	9.3	439	458	4.34	T.S
1-3	0.086	0.344	9.3		496	4.36	T.S
1-4	0.086	0.344	9.3		472	4.68	T.S
1-1R	0.090	0.360	10.2		429	(2.46)	R.S
1-5R	0.087	0.348	9.5		441	—	—
1-6R	0.090	0.360	10.2		460	(3.24)	R.S
2-4	0.124	0.496	19.3	370	378	3.65	T.S
2-5	0.125	0.500	19.6		384	4.04	T.S
2-1R	0.125	0.500	19.6		396	(1.8)	R.S
2-2R	0.123	0.492	19.0		354	(2.22)	R.S
2-3R	0.125	0.500	19.6		379	(2.28)	R.S
3-2	0.152	0.608	29.0	283	289	3.73	T.S
3-5	0.153	0.612	29.4		305	3.04	T.S
3-1R	0.155	0.620	30.2		352	(1.8)	R.S
3-3R	0.154	0.616	29.8		271	(2.76)	R.S
3-4R	0.155	0.620	30.2		304	(1.62)	R.S
4-2	0.176	0.704	38.9	253	226	2.31	T.S
4-5	0.176	0.704	38.9		236	2.40	T.S
4-1R	0.179	0.716	40.2		233	(2.04)	R.S
4-3R	0.186	0.744	43.4		208	(1.12)	R.S
4-4R	0.186	0.744	43.4		210	(1.55)	R.S
5-2	0.200	0.800	50.2	169	177	1.52	T.S
5-5	0.198	0.792	49.2		175	1.70	T.S
5-1R	0.199	0.796	49.7		163	(1.11)	R.S
5-3R	0.195	0.780	47.7		179	(1.26)	R.S
5-4R	0.195	0.780	47.7		170	(1.24)	R.S

SPECIMEN THICKNESS WAS t ≈ 0.256 INCHES

(1) The nominal center-to-center hole spacing for all specimen was 2ℓ=0.250 in.
(2) T.S denotes failure in the test section in specimens without any residual stresses; R.S denotes that specimens contained residual stress (see Fig.38)

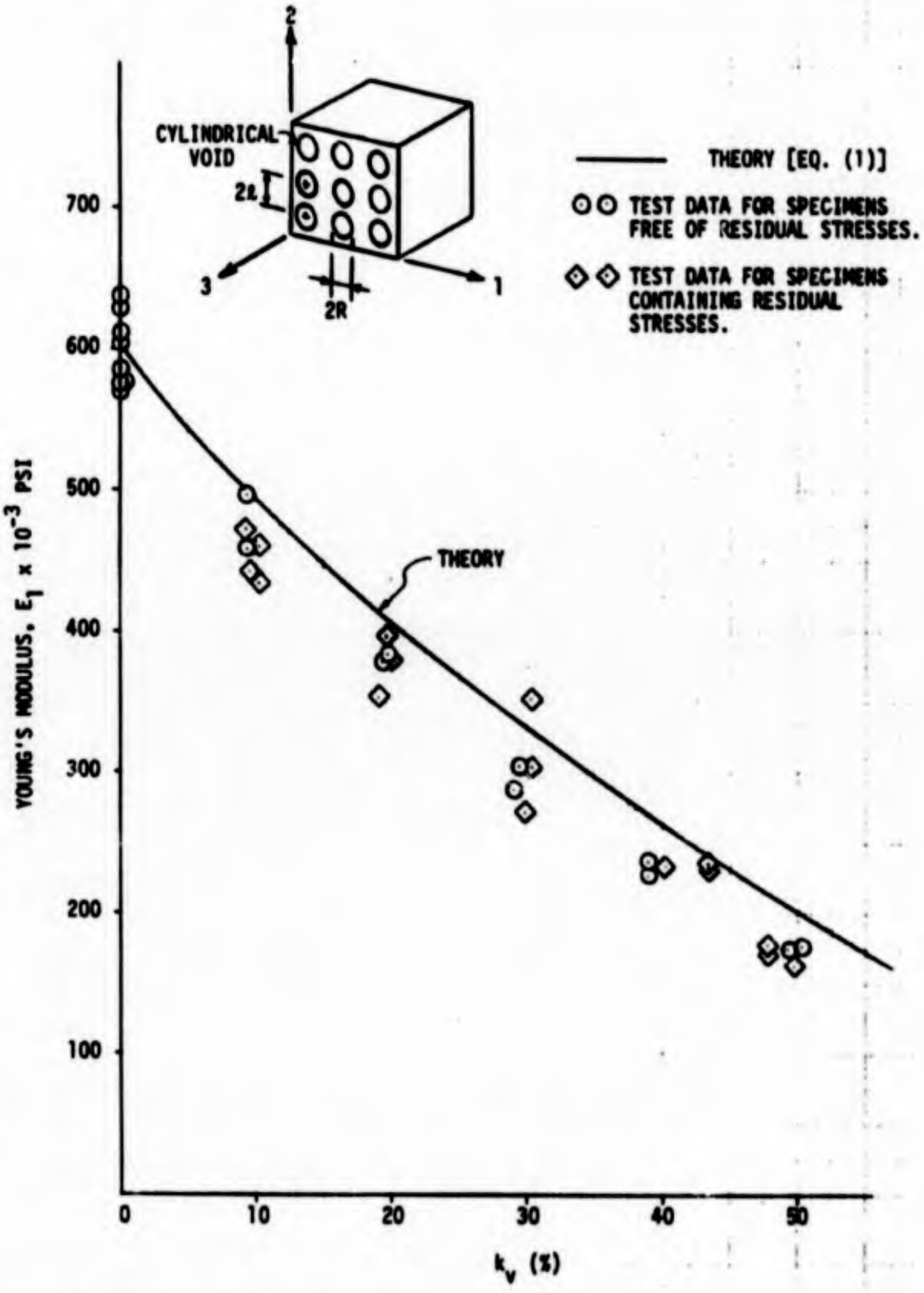

Figure 14. Influence of Void Content on Young's Modulus of a Solid

Section 3
INTERNAL STRESSES IN SOLIDS CONTAINING VOIDS

In accordance with the general study approach shown in Figure 1, the next step in formulating the micromechanics failure theory was to determine the internal stresses caused by voids. The pertinent results for this problem are presented herein and employed in Section 6 to study the interaction of stress concentration from fibers and voids, and in Section 5 in failure theory formulation.

3.1 THEORETICAL PREDICTION OF INTERNAL STRESSES FROM TRANSVERSE LOADING

The model used in determining the stresses due to transverse loading is shown in Figure 15. As before, the voids are assumed to be cylindrical in shape and arranged in a square array. A detailed derivation of the approximate expression for internal stresses at various locations is given in Appendix A: only the final equations are summarized here. The final

CR84

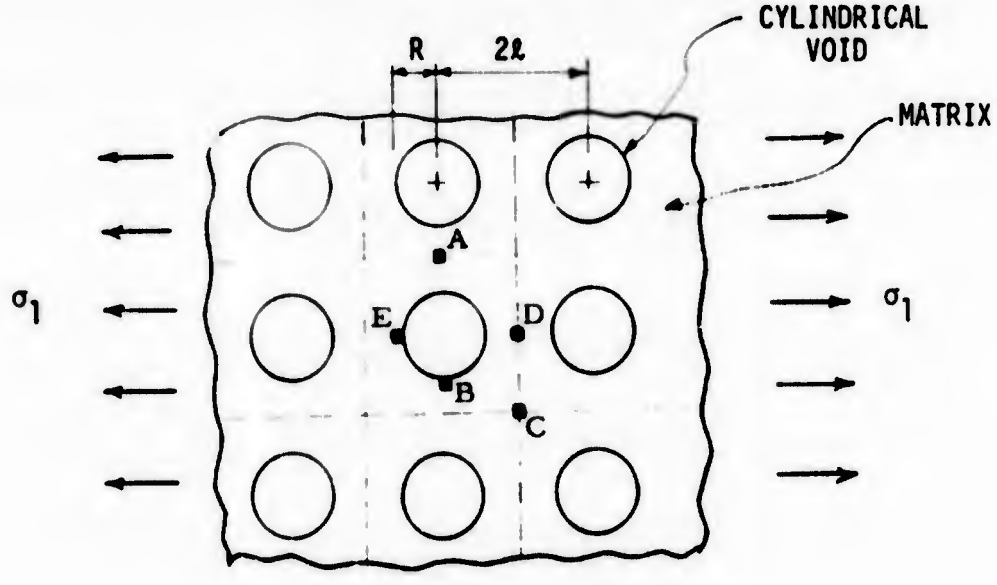

Figure 15. Mathematical Model for Determining Internal Stresses Due to Transverse Loading

expressions for stress concentrations at locations A, B, C, D, and E shown in Figure 15 are:

$$K_{xA} = \frac{\sigma_{xA}}{\sigma_1} = \frac{2 + \lambda^2 + 3\lambda^4}{2 - \lambda^2 - \lambda^4} \tag{8}$$

$$K_{yA} = \frac{\sigma_{yA}}{\sigma_1} = \frac{3(\lambda^2 - \lambda^4)}{2 - \lambda^2 - \lambda^4} \tag{9}$$

$$K_{xB} = \frac{\sigma_{xB}}{\sigma_1} = \frac{6}{2 - \lambda^2 - \lambda^4} \tag{10}$$

$$K_{yB} = \frac{\sigma_{yB}}{\sigma_1} = 0 \tag{11}$$

$$K_{xC} = \frac{\sigma_{xC}}{\sigma_1} = \frac{1}{2}\left(2 + \lambda^2 - \frac{3}{4}\lambda^4\right)\xi \tag{12}$$

$$K_{yC} = \frac{\sigma_{yC}}{\sigma_1} = \frac{1}{2}\left(-\lambda^2 + \frac{3}{4}\lambda^4\right)\xi \tag{13}$$

$$K_{xD} = \frac{\sigma_{xD}}{\sigma_1} = \left(\frac{1 - \lambda}{2}\right)\left(2 - 5\lambda^2 + 3\lambda^4\right)\xi \tag{14}$$

$$K_{yD} = \frac{\sigma_{yD}}{\sigma_1} = \left(\frac{1-\lambda}{2}\right)\left(\lambda^2 - \frac{3}{4}\lambda^4\right)\xi \tag{15}$$

$$K_{xE} = \frac{\sigma_{xE}}{\sigma_1} = 0 \tag{16}$$

$$K_{yE} = \frac{\sigma_{yE}}{\sigma_1} = -(1-\lambda)\xi \tag{17}$$

where

$$\lambda = R/\ell = \sqrt{\frac{4k_v}{\pi}} \tag{18}$$

$$\xi = \frac{2}{\sqrt{1-\lambda^2}} \tan^{-1}\sqrt{\frac{1+\lambda}{1-\lambda}} - \frac{\pi}{2} + \frac{1-\lambda}{1-\frac{\pi}{4}\lambda^2} \tag{19}$$

The theoretical stress concentrations at various locations are plotted in Figures 16 and 17.

In actual composites containing fibers, voids, and matrix, the matrix, in which the voids are assumed to be located, is under triaxial stresses when the composite is subjected to transverse loading (see Table 1). For the case of a porous matrix subjected to externally applied triaxial stresses, the internal stresses can be obtained by superposition. As a first approximation it is assumed here that the transverse stresses caused by externally applied axial stresses* along the cylindrical void axis are small, which reduces the problem to that of determining the internal stresses in

* The axial stresses due to axial loading are considered in Subsection 3.3.

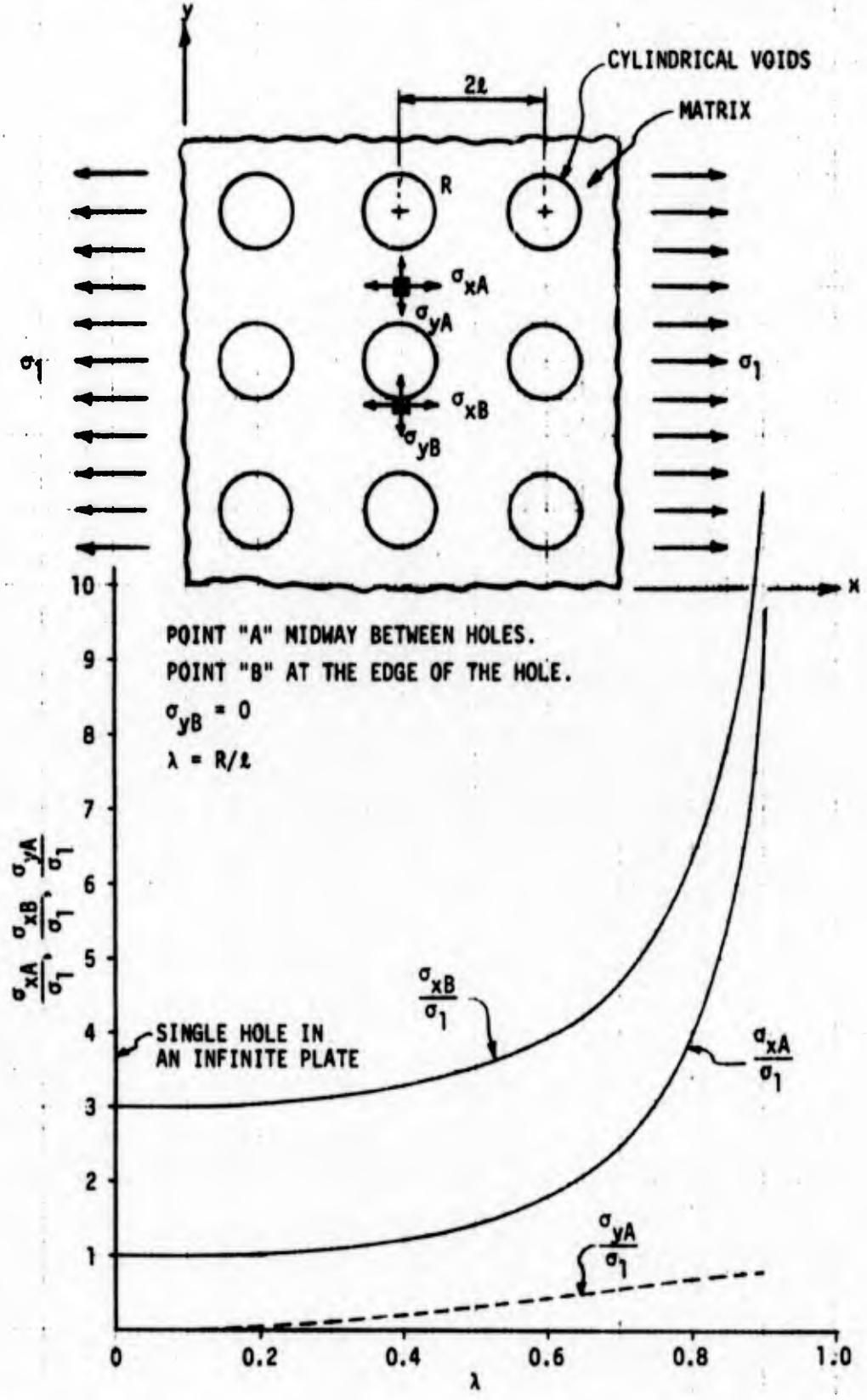

Figure 16. Internal Maximum Stresses in Solids Containing Cylindrical Voids and Subjected to Transverse Loading

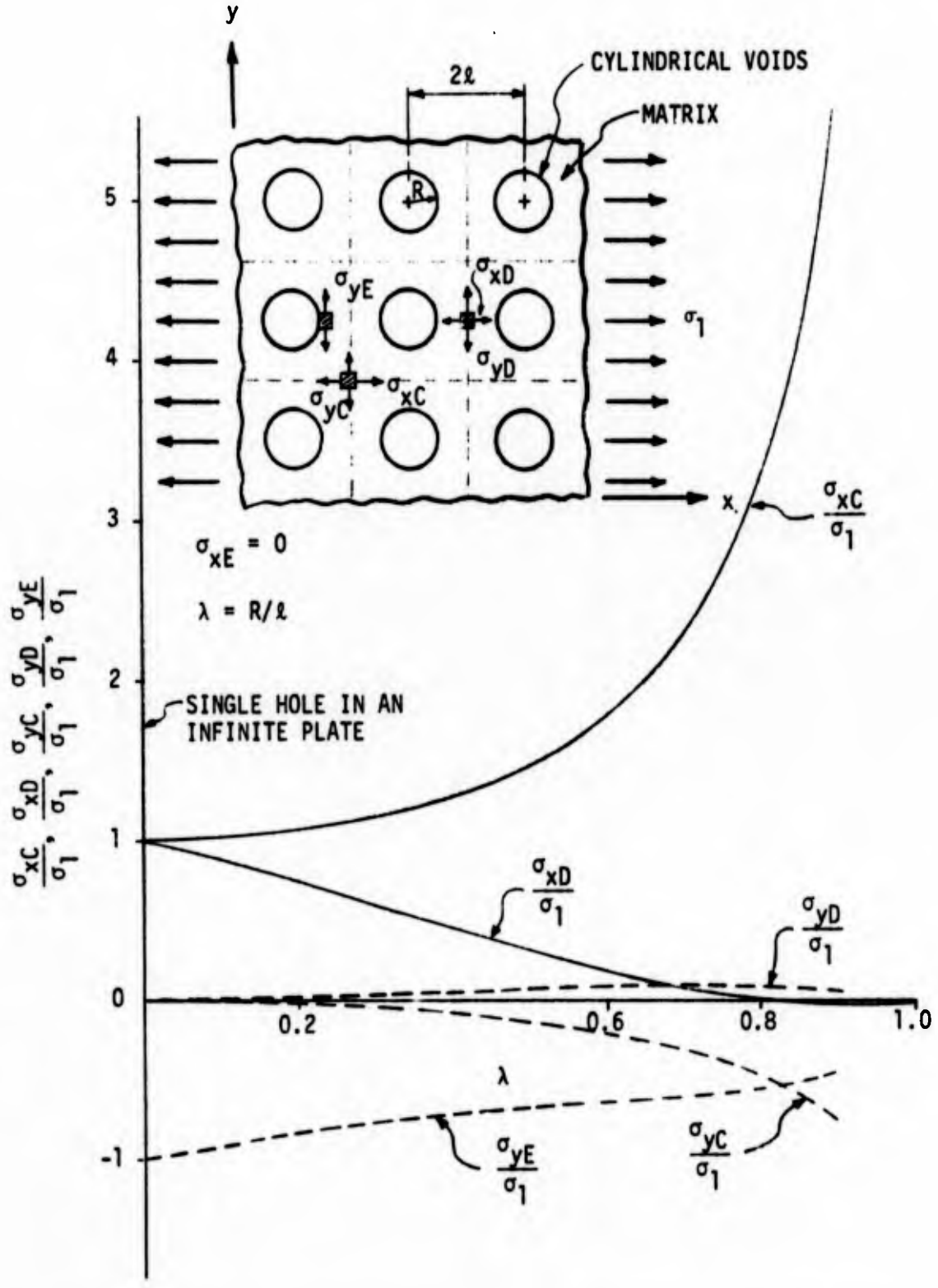

Figure 17. Secondary Stresses in Solids Containing Cylindrical Voids and Subjected to Transverse Loading

a porous solid under an externally applied biaxial loading (Figure 18).

The internal biaxial stresses at the points of interest (A, B, C, D, and E) can be obtained by superposition:

$$
\left.
\begin{aligned}
\tilde{\sigma}_{xA} &= K_{xA}\,\sigma_1 + K_{yD}\,\sigma_2 \\
\tilde{\sigma}_{yA} &= K_{yA}\,\sigma_1 + K_{xD}\,\sigma_2 \\
\tilde{\sigma}_{xB} &= K_{xB}\,\sigma_1 + K_{yE}\,\sigma_2 \\
\tilde{\tau}_{yB} &= 0 \\
\tilde{\sigma}_{xC} &= K_{xC}\,\sigma_1 + K_{yC}\,\sigma_2 \\
\tilde{\sigma}_{yC} &= K_{yC}\,\sigma_1 + K_{xC}\,\sigma_2 \\
\tilde{\sigma}_{xD} &= K_{xD}\,\sigma_1 + K_{yA}\,\sigma_2 \\
\tilde{\sigma}_{yD} &= K_{yD}\,\sigma_1 + K_{xA}\,\sigma_2 \\
\tilde{\sigma}_{xE} &= 0 \\
\tilde{\sigma}_{yE} &= K_{yE}\,\sigma_1 + K_{xB}\,\sigma_2
\end{aligned}
\right\} \qquad (20)
$$

where the K terms are given in Equations (8) through (17). The above equations can be used to predict the internal stresses in porous solids subjected to any combination of externally applied biaxial stresses. Figures 19 and 20 show some typical results. The results shown in Figure 19 are for a porous solid subjected to a 1:1 biaxial stress ratio, while those shown in Figure 20 are for a porous solid subjected to a 2:1 biaxial stress ratio.

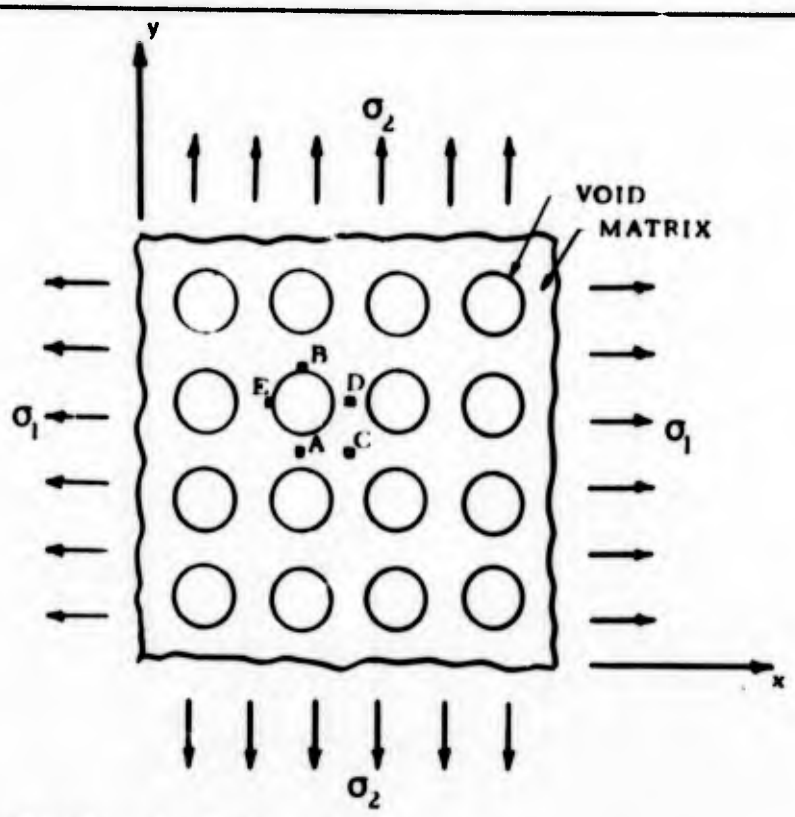

Figure 18. Porous Solid Subjected to Biaxial Loading

3.2 EXPERIMENTAL STUDIES ON INTERNAL STRESSES FROM TRANSVERSE LOADING AND TEST-THEORY COMPARISON

To verify the theoretically predicted stress concentrations caused by voids, photoelastic test specimens were fabricated and tested in tension. Figure 21 and its accompanying table show the geometry of the photoelastic test specimens. The test variable in various specimens was the void content, as is readily apparent from Figure 21. The photoelastic test specimens were made from Homalite 100. To ensure that the holes were stress free after machining, the holes were drilled using an end mill and WD40 as a coolant, which was fed continuously onto the end mill during drilling. This technique produced holes that were free of any residual stresses, as shown later in Section 5. In addition to the use of photoelasticity to measure the internal stresses and the differences between the principal stresses in plates with various void contents, the plates were instrumented with strain gages, the data from which were also used to obtain the stresses at various locations. The photoelastic test specimens were subjected to a tensile dead-weight load of 1,220.10 lb, and fringe orders were obtained under the said loading.

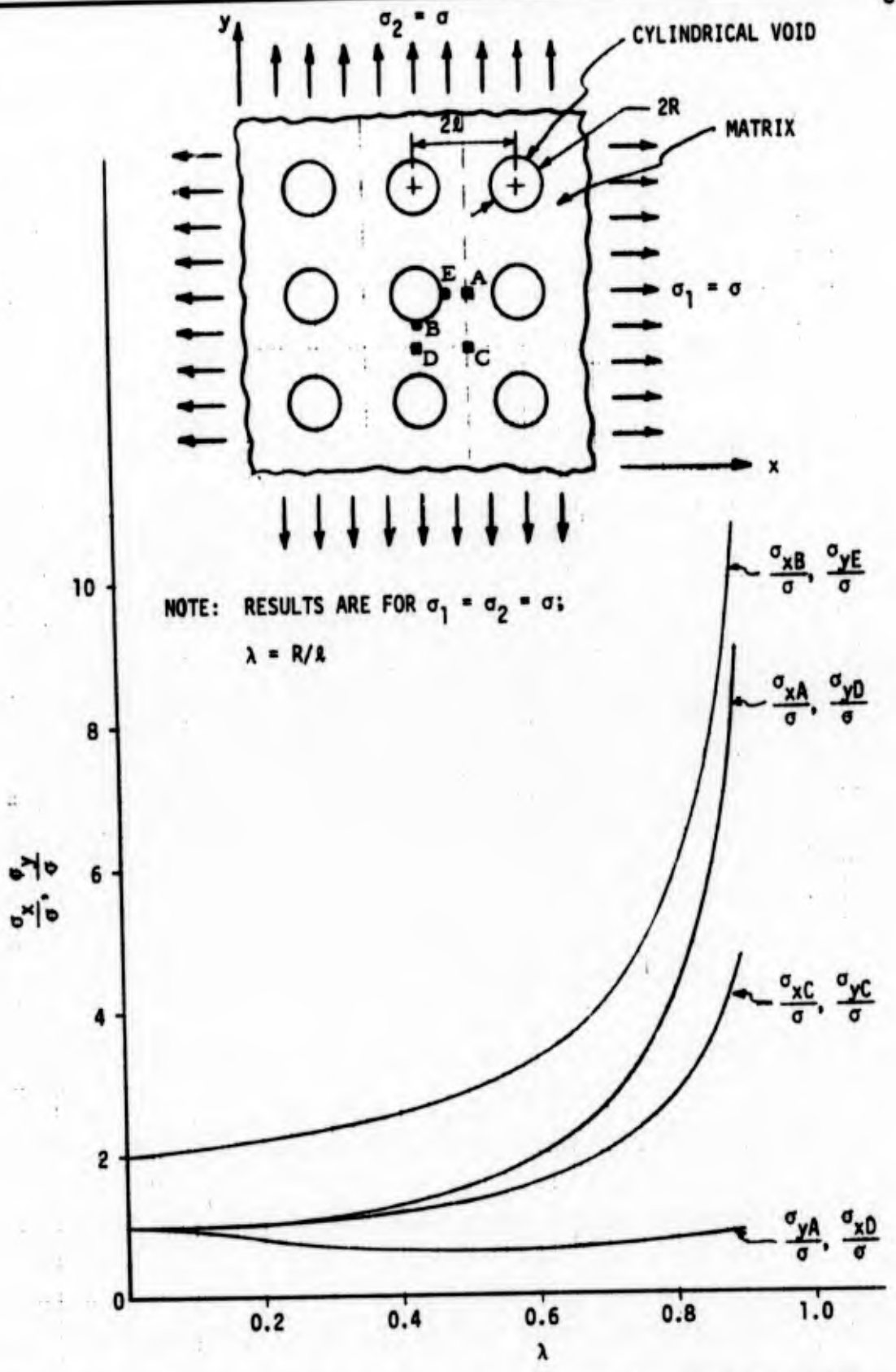

Figure 19. Stress Concentrations in a Porous Solid Subjected to Biaxial Loading (Biaxial Stress Ratio of 1:1)

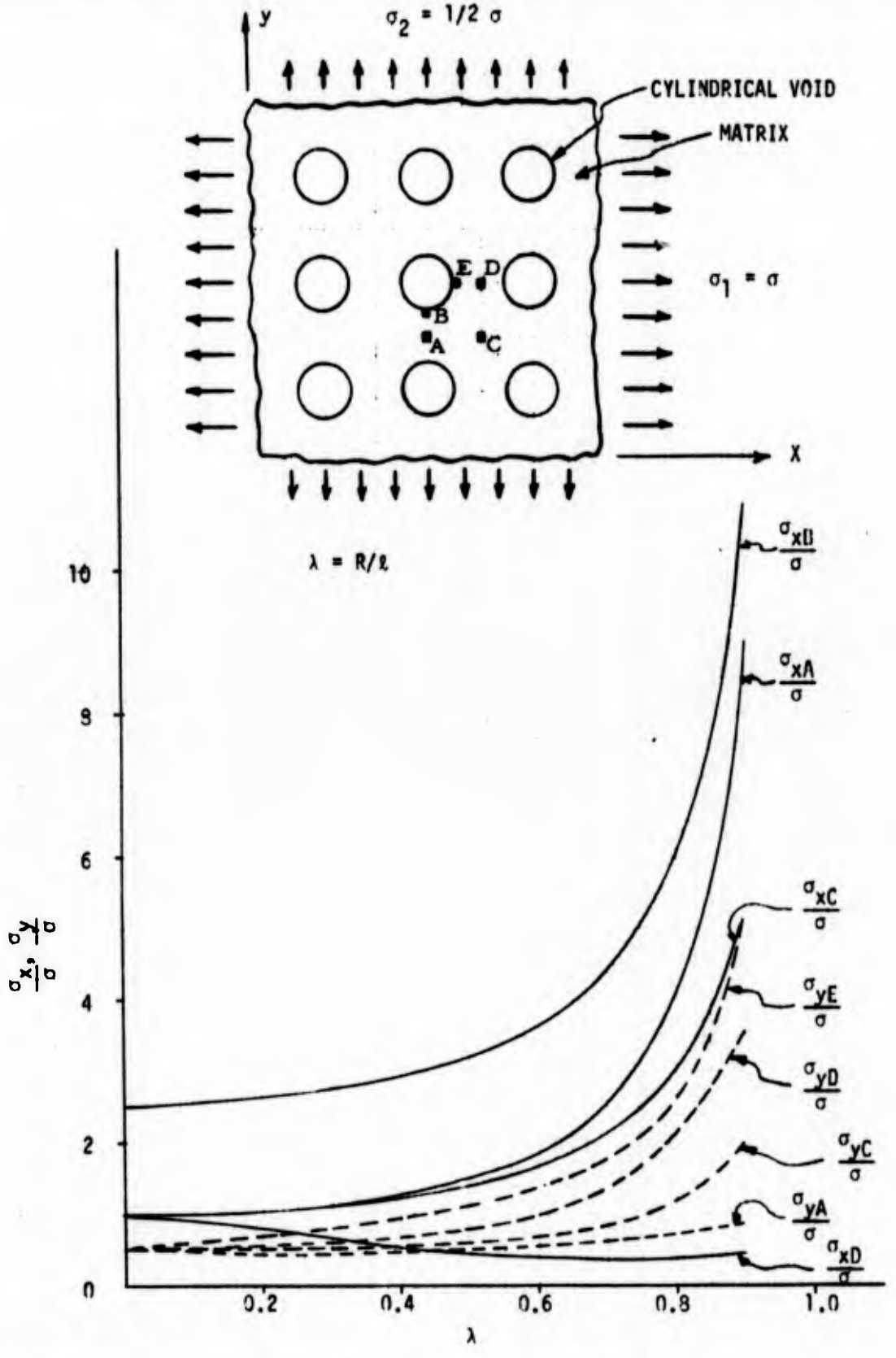

Figure 20. Stress Concentrations in a Porous Solid Subjected to Biaxial Loading (Biaxial Stress Ratio of 2:1)

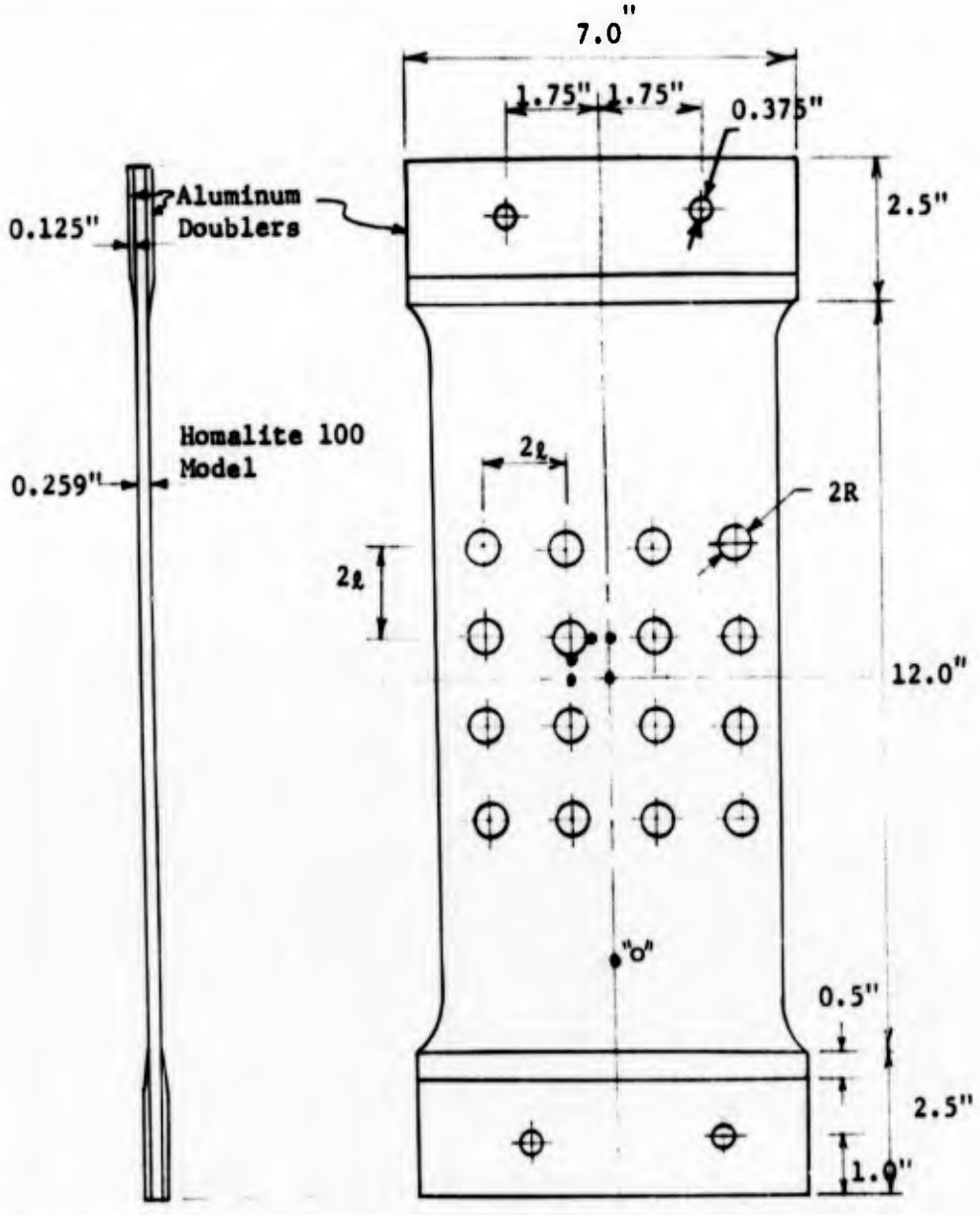

NOTE: Stresses Measured at these (•) Locations

Specimen Configuration	2ℓ (In.)	R (In.)	λ=R/ℓ	k_v^* (%)	Test Technique
1	1.586	0.200	0.252	5	Photoelasticity and Strain Gages
2	1.586	0.284	0.358	10	
3	1.586	0.346	0.437	15	
4	1.586	0.400	0.505	20	
5	1.586	0.490	0.618	30	

* Nominal

Figure 21. Photoelastic Test Specimen for Determining Internal Stresses in a Solid with Cylindrical Voids

Typical fringe patterns around the holes in four of the specimen configurations are shown in Figures 22 and 23. In addition, to the fringe patterns, these figures also show the location of the strain gages. Figure 22 shows the close-up view of the fringe pattern around the central holes, while Figure 23 shows the fringe patterns around all 16 holes in specimens with two different void contents.

The experimentally obtained stress concentrations in plates with various volume fractions of voids are presented in Tables B-1 through B-5 of Appendix B. Biaxial strains and biaxial stress concentrations are given at five points within the perforated plate, as shown in Table B-1, and also at a point away from the holes, Point O. Tables B-1 through B-5 also show the differences between the principal stresses at various locations, as obtained by strain gages and by photoelasticity. Except for Point D, where the stresses and strains were extremely small and difficult to measure, the principal stress differences obtained by the two test techniques at Locations A, B, C, E, and O show good correlation. Most of the results obtained by the two test methods agree within 5 percent.

The test-theory comparison of the internal stress concentrations in plates with voids is shown in Figures 24, 25, and 26. The theoretical stress concentrations at various locations were calculated from Equations 8 through 17.

3.3 INTERNAL STRESSES FROM AXIAL AND SHEAR LOADING

In a composite containing fibers, matrix, and cylindrical voids aligned with the fiber direction, the stresses in the matrix in the direction of the void axis will generally be quite small if such a composite is subjected to external stresses in the direction of the fibers. The latter can readily be established using the law of mixtures. In view of the above, only an approximate equation is sought here for the stresses in a matrix containing cylindrical voids and subjected to externally applied stresses in the direction-of-void axis (see Figure 27). Applying the law of mixtures to the latter problem yields the following approximate expression for the stresses in a matrix

$$\sigma_z = (1 - k_v)\,\sigma_3 = (1-\frac{\pi}{4}\lambda^2)\,\sigma_3 \qquad (21)$$

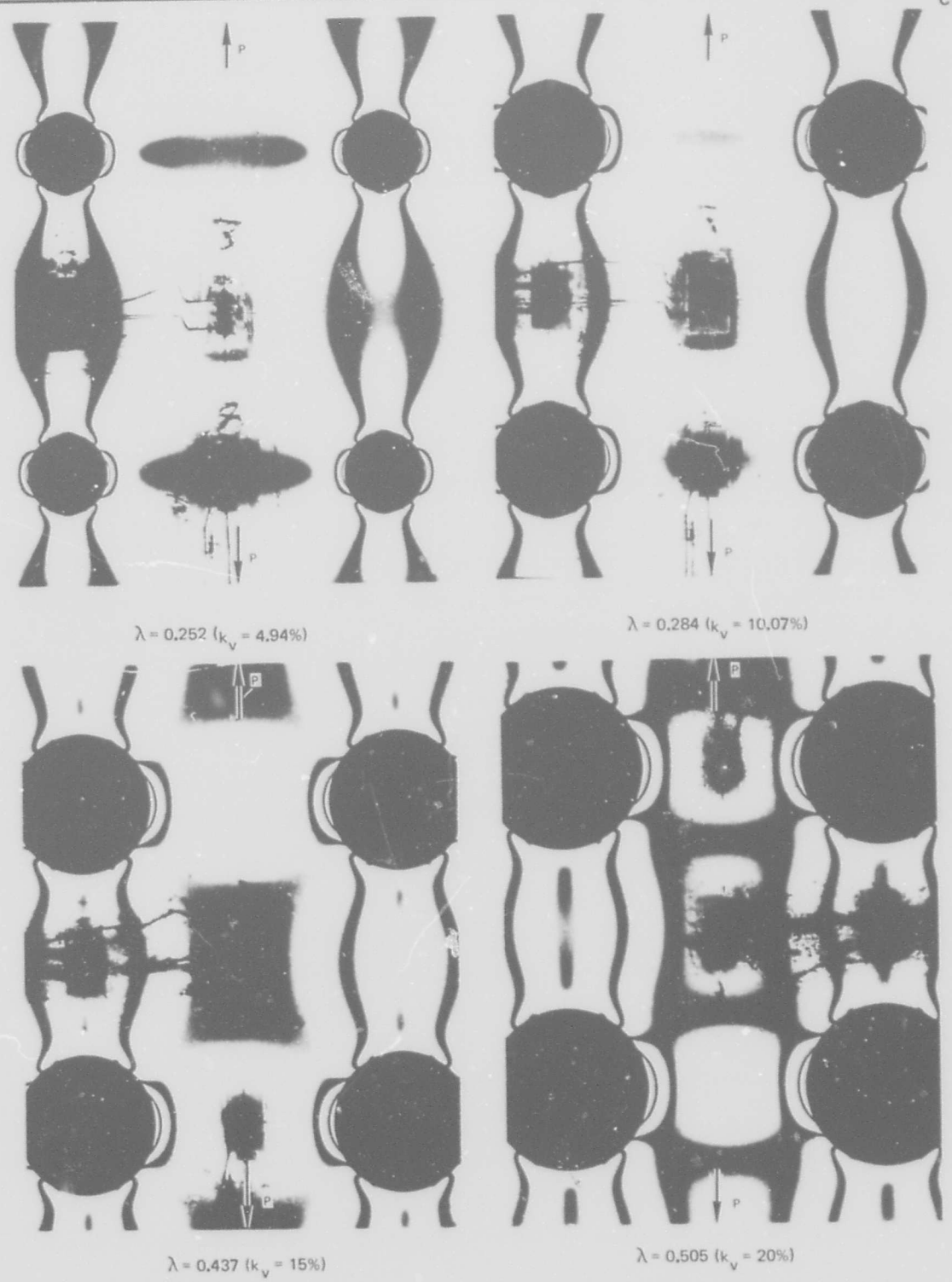

Figure 22. Photoelastic Fringe Pattern in Plates with Various Contents of Cylindrical Voids (Load P = 1,220.1 lb)

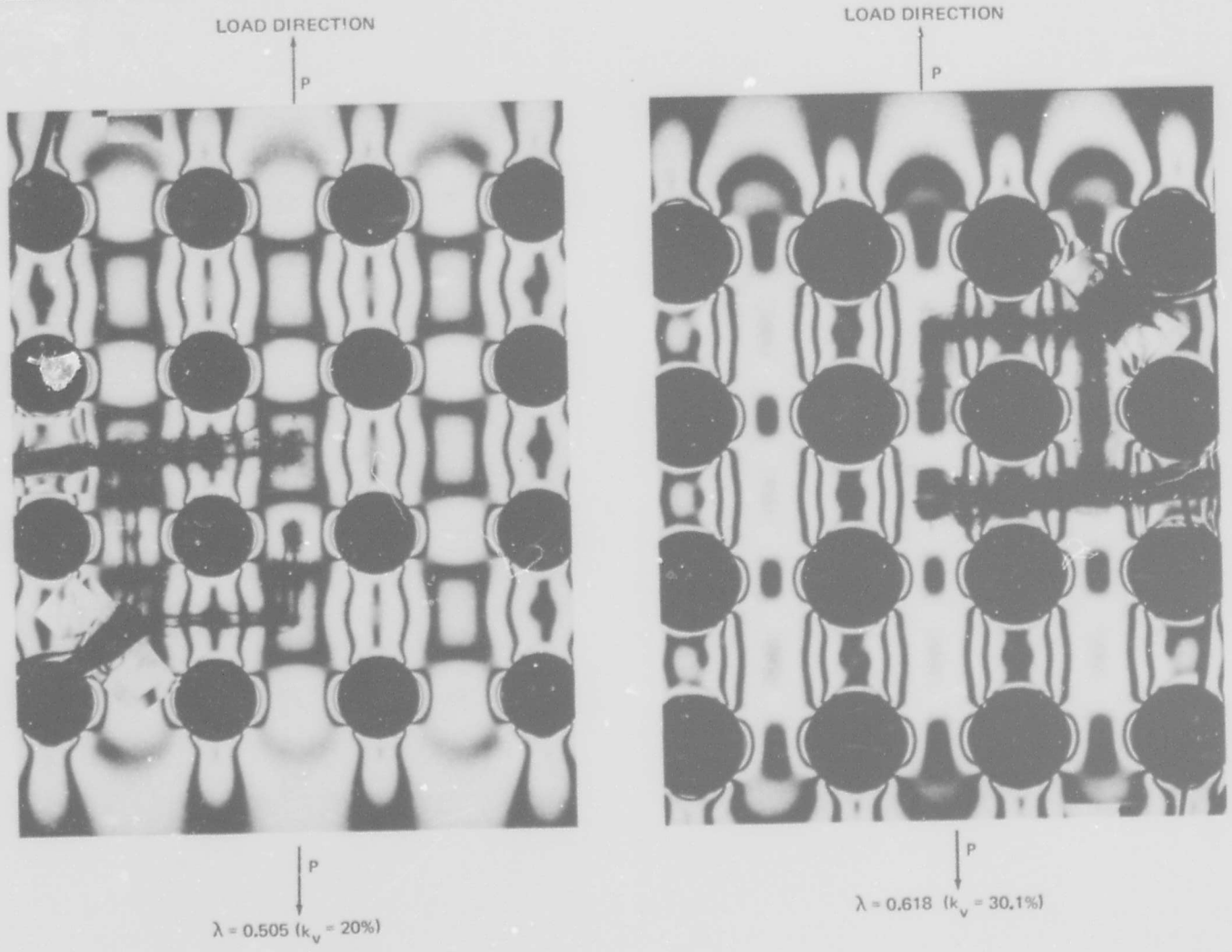

Figure 23. Overall View of the Photoelastic Fringe Pattern in Plates with Cylindrical Voids (Load P = 1,220.1 lb)

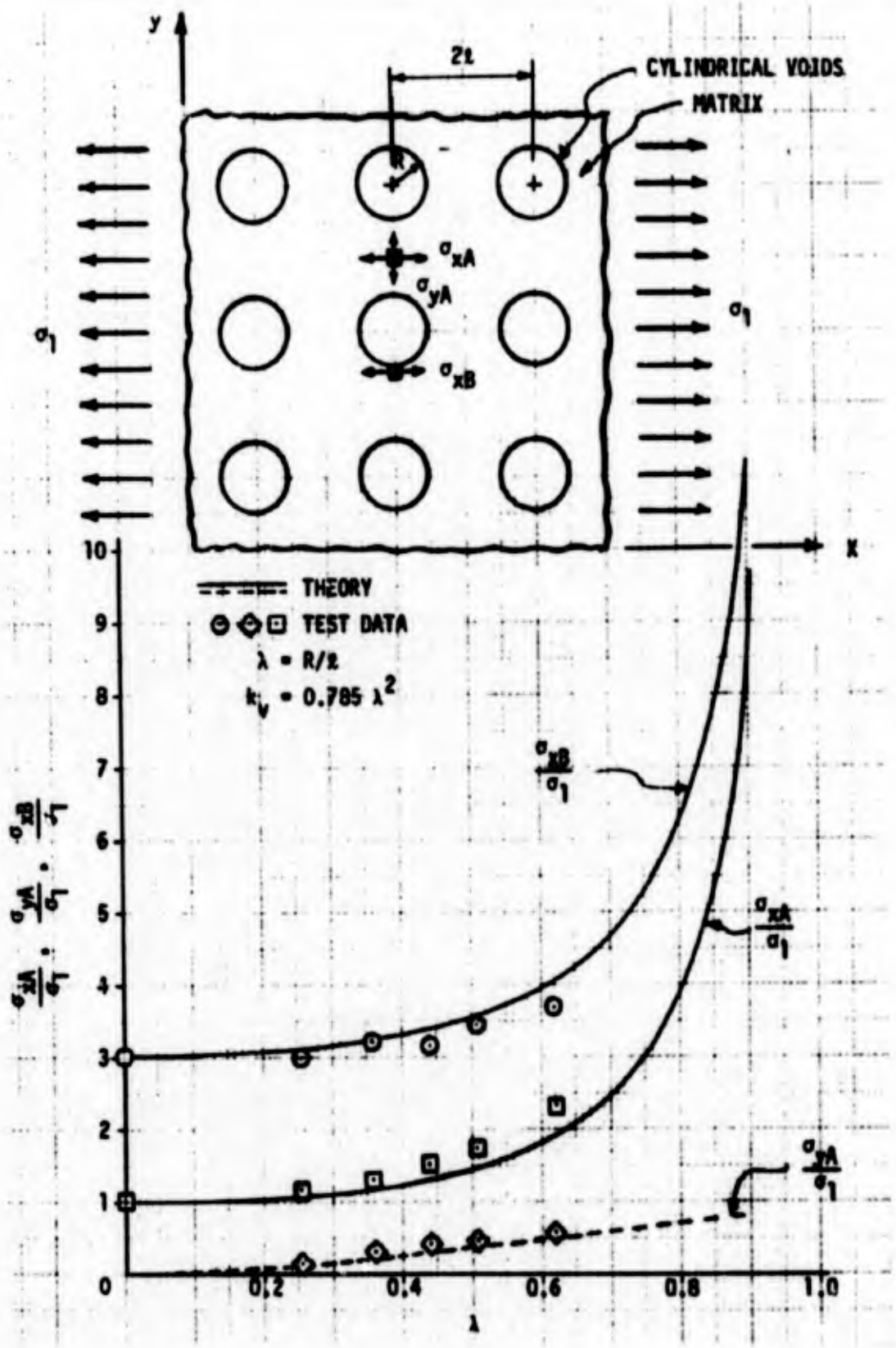

Figure 24. Test-Theory Comparison of Internal Stresses at Locations A and B

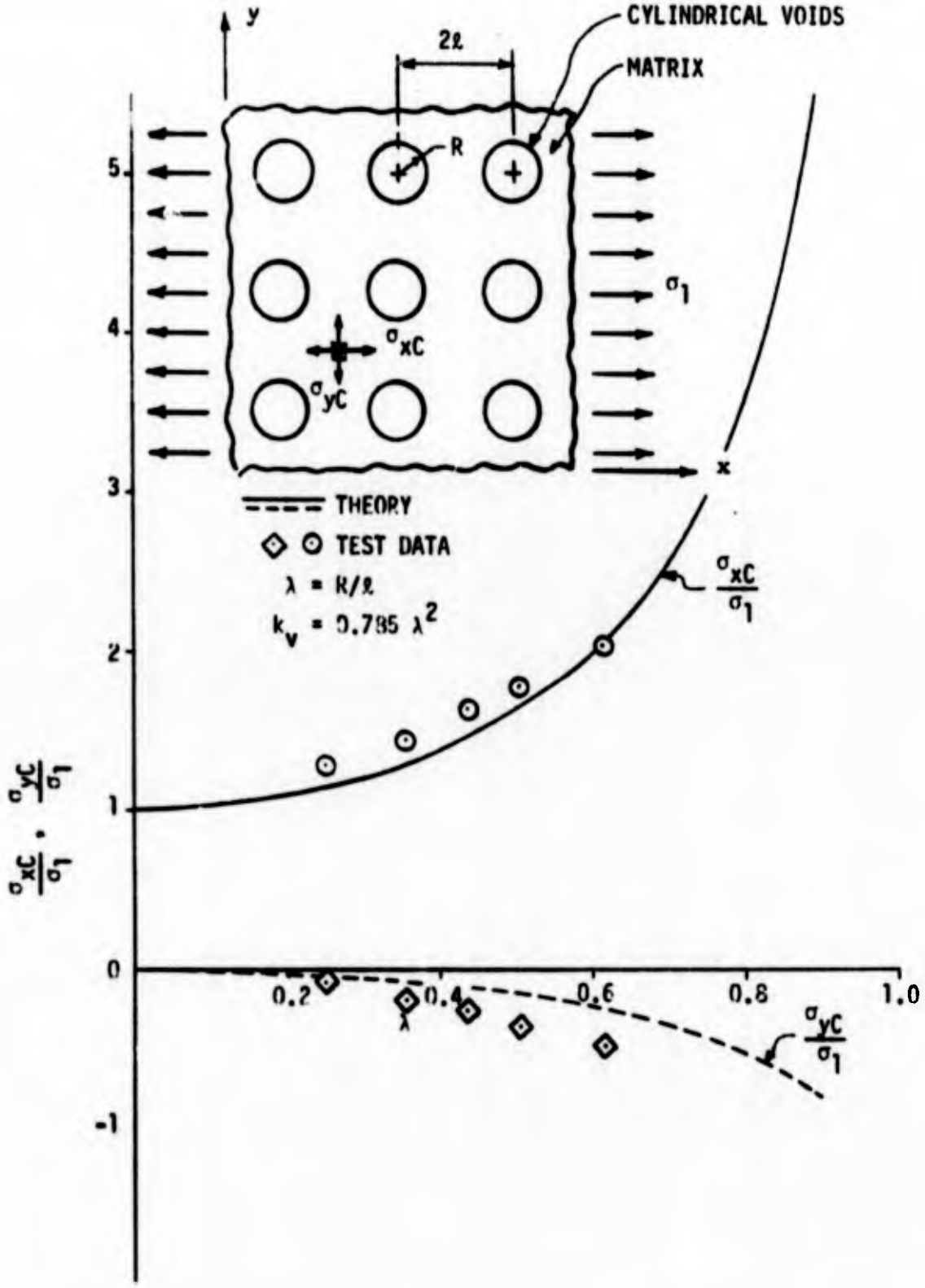

Figure 25. Test-Theory Comparison of Internal Stresses at Location C

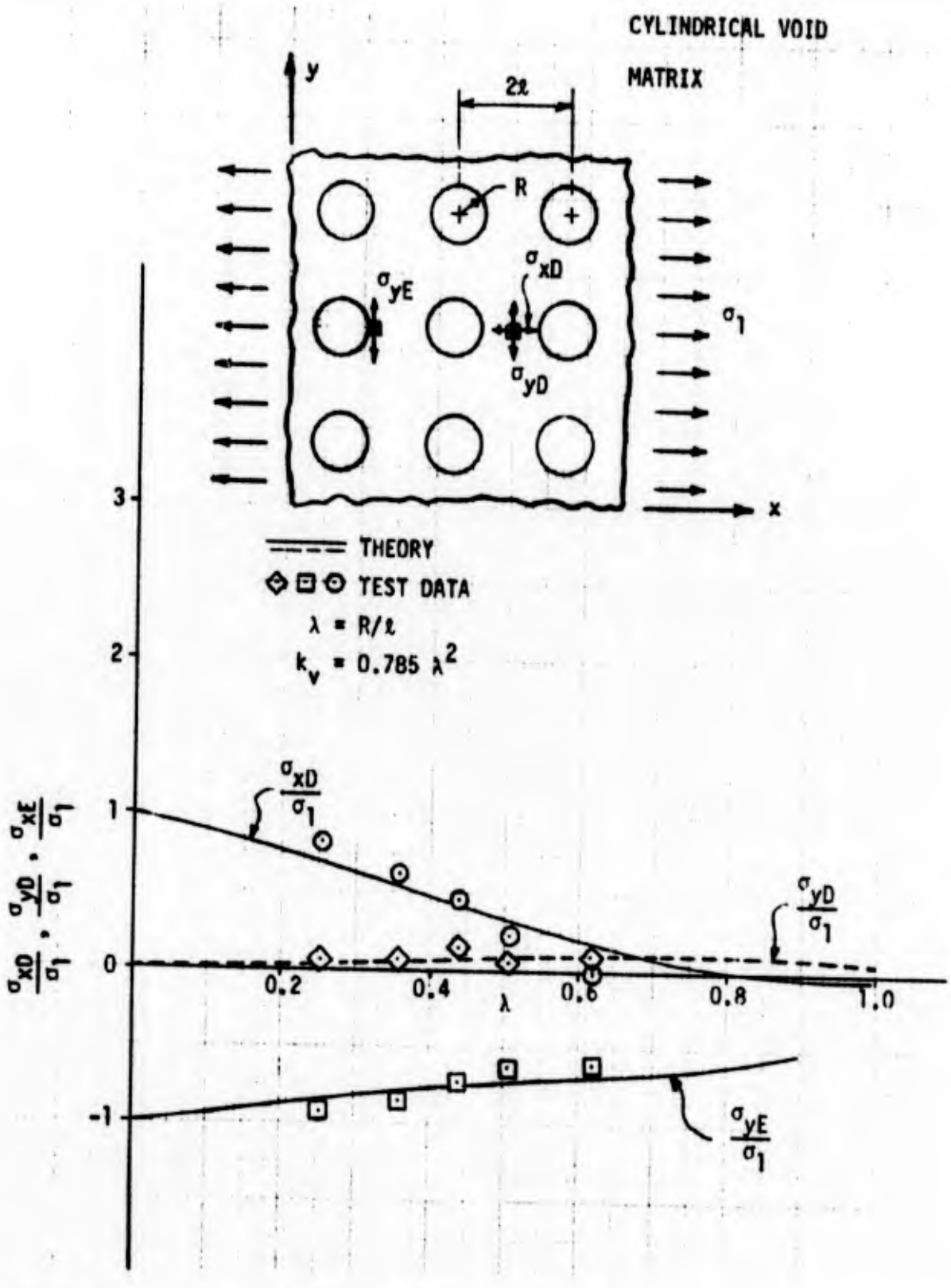

Figure 26. Test-Theory Comparison of Internal Stresses at Locations D and E

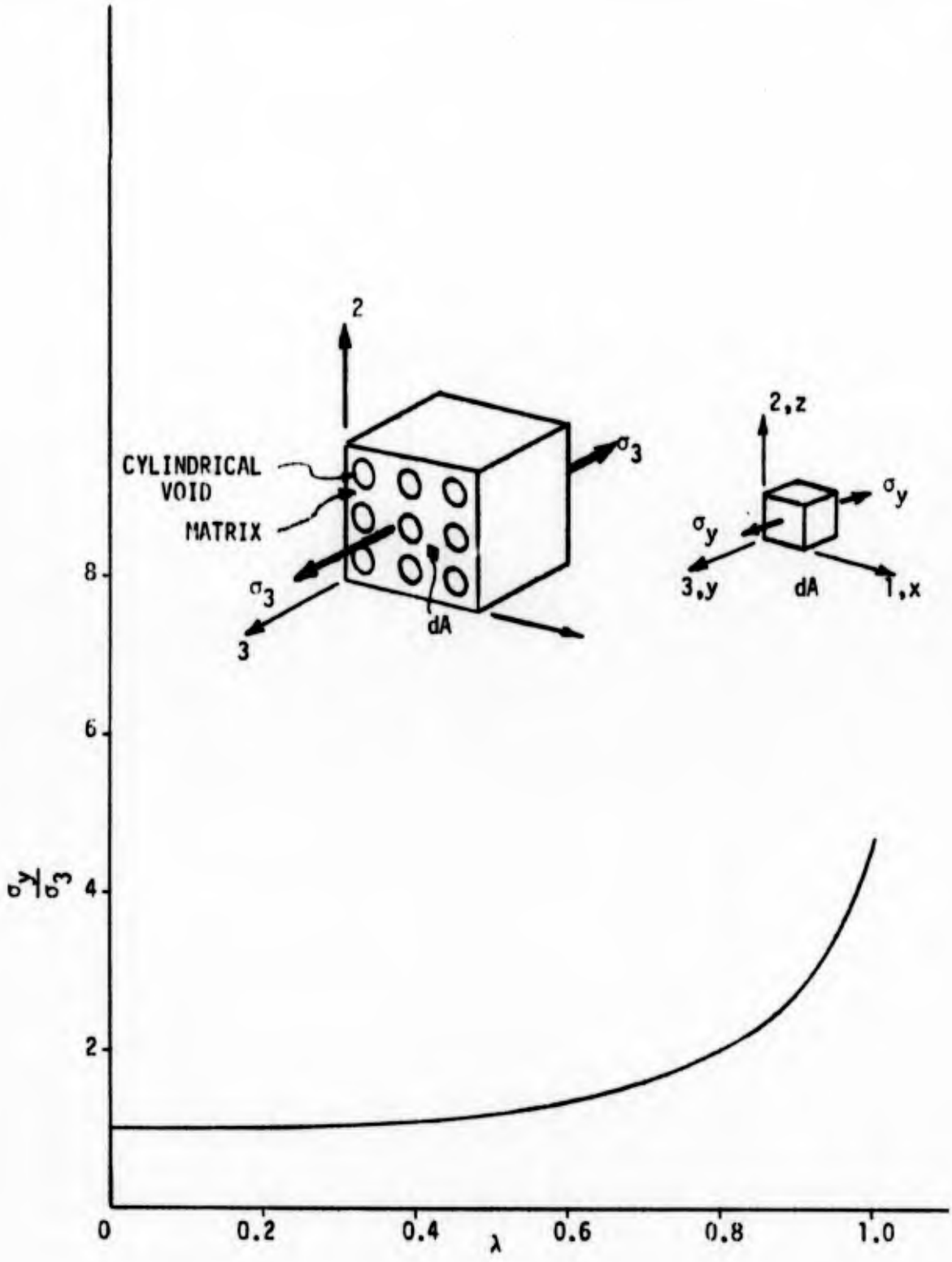

Figure 27. Internal Stresses in Porous Solids Subjected to Loads in the Direction of Cylindrical Void Axis

or

$$\frac{\sigma_z}{\sigma_3} = K_{zC} \text{ where } K_{zC} = (1 - \frac{\pi}{4}\lambda^2)$$

where, as shown in Figure 27, σ_3 is the remotely applied stress in the direction of void axis and σ_z is the stress in the matrix. The variation of σ_z as a function of λ is shown also in Figure 27.

If a solid containing cylindrical voids is subjected to shear loading, as shown in the diagram in Figure 28, the maximum internal shear stresses in the matrix can be obtained from the following approximate expression

$$\tau_{xz} \approx \frac{\tau_{13}}{1-\lambda} \tag{22}$$

or

$$\frac{\tau_{xz}}{\tau_{13}} = K_{xzA} = \frac{1}{1-\lambda} \tag{22}$$

which follows readily from the elementary considerations presented in Appendix A. The variation of τ_{xz}/τ_{13} as a function of λ is shown in Figure 28.

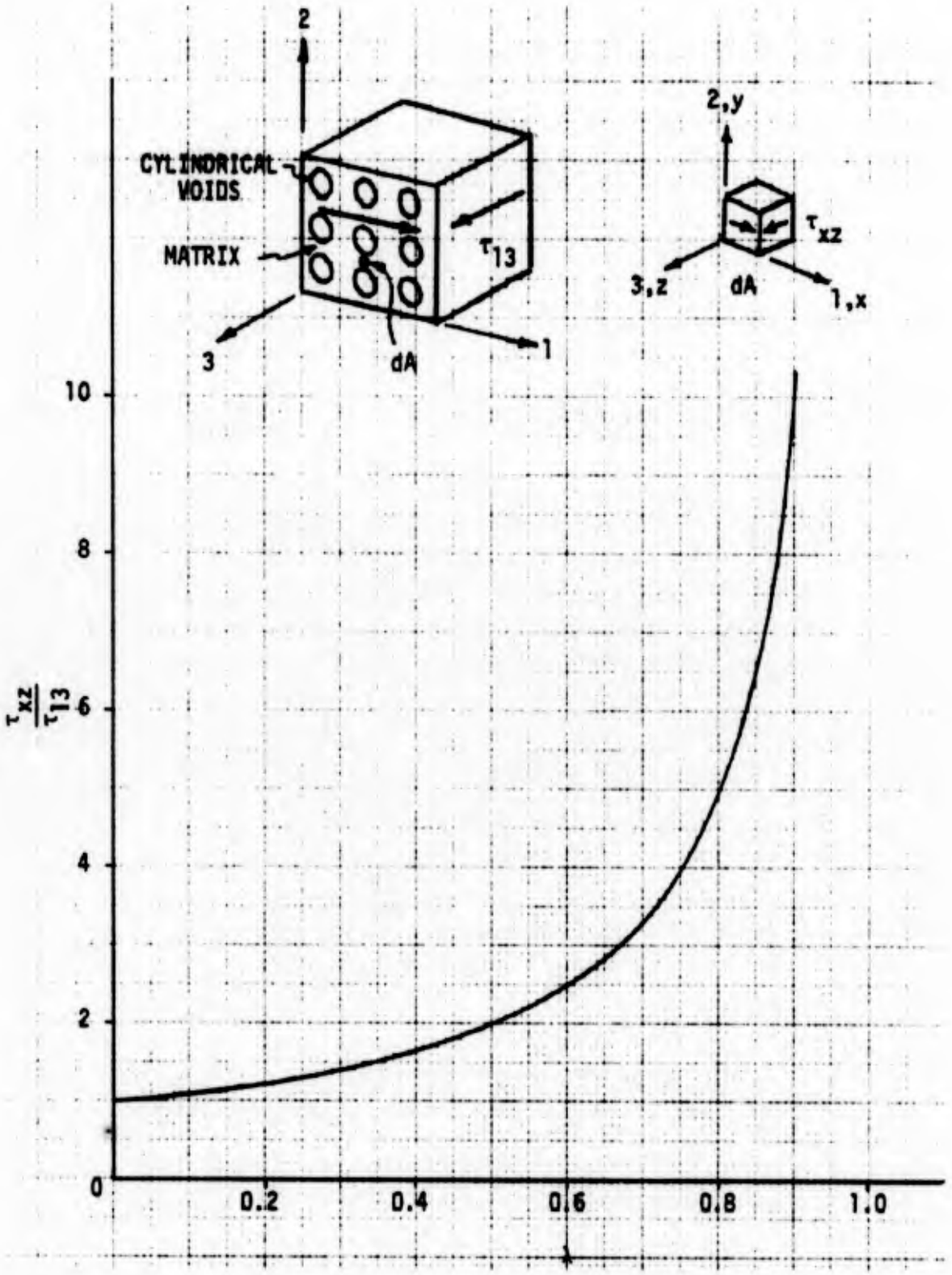

Figure 28. Maximum Internal Shear Stresses in Solids Containing Cylindrical Voids

Section 4
STRESS INTERACTION FROM FIBERS AND VOIDS

If the internal triaxial stresses in a void-free fiber-reinforced composite subjected to transverse loading, σ_T (see Table 1 of Section 1), and the triaxial stress concentrations due to voids (Equations 20) are known, the stress concentrations in a composite containing fibers and voids can be obtained by superposition.

4.1 THEORETICAL STUDIES ON FIBER-VOID STRESS INTERACTION UNDER TRANSVERSE LOADING

For an idealized composite model (shown in Figure 29), the stresses, including fiber-void stress interaction, at the points of interest (A, B, C, D, and E) can be obtained by superposition, and are

$$
\left.
\begin{aligned}
\sigma^*_{xA} &= \left(K_{xA}K_x + K_{yD}K_y\right)\sigma_T \\
\sigma^*_{yA} &= \left(K_{yA}K_x + K_{xD}K_y\right)\sigma_T \\
\sigma^*_{xB} &= \left(K_{xB}K_x + K_{yE}K_y\right)\sigma_T \\
\sigma^*_{yB} &= 0 \\
\sigma^*_{xC} &= \left(K_{xC}K_x + K_{yc}K_y\right)\sigma_T \\
\sigma^*_{yC} &= \left(K_{yC}K_x + K_{xC}K_y\right)\sigma_T \\
\sigma^*_{xD} &= \left(K_{xD}K_x + K_{yA}K_y\right)\sigma_T \\
\sigma^*_{yD} &= \left(K_{yD}K_x + K_{xA}K_y\right)\sigma_T \\
\sigma^*_{xE} &= 0 \\
\sigma^*_{yE} &= \left(K_{yE}K_x + K_{xB}K_y\right)\sigma_T
\end{aligned}
\right\} \qquad (23)
$$

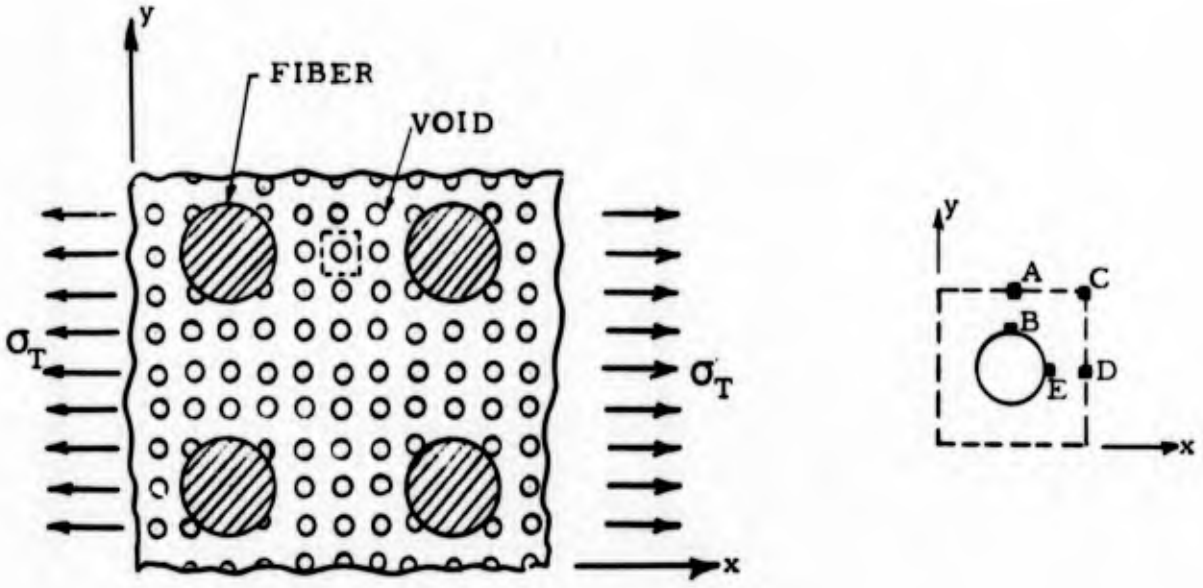

Figure 29. Idealized Model Composite Containing Fibers, Voids, and Matrix

where σ_T is the applied transverse stress, K_x and K_y are given in Table 1 of Section 1 and are a function of constituent properties, and fiber volume fraction and K_{xA}, K_{xB}, -- K_{yA}, K_{yB} -- are given by Equations 8 through 17. The terms K_x and K_y correspond to E_x/E_r^* where E_r^* is the Young's modulus of a matrix containing voids. In obtaining Equations 23, it was assumed that the matrix stresses σ_x and σ_y due to the fiber-induced matrix stress in the direction of cylindrical void axis are negligible. With this assumption the stress in the matrix normal to the plane of Figure 29 is

$$\sigma_z^* = K_z K_{zC} \sigma_T \tag{24}$$

where K_z is given in Table 1 of Section 1 and K_{zC} is given by Equation 21. Equations 23 and 24 give the triaxial stresses in the matrix of a composite consisting of fibers, cylindrical voids, and resin, and include the interaction of stress concentrations from fibers and voids. Typical results on the interaction of stress concentrations from fibers and voids are shown in Figure 30.

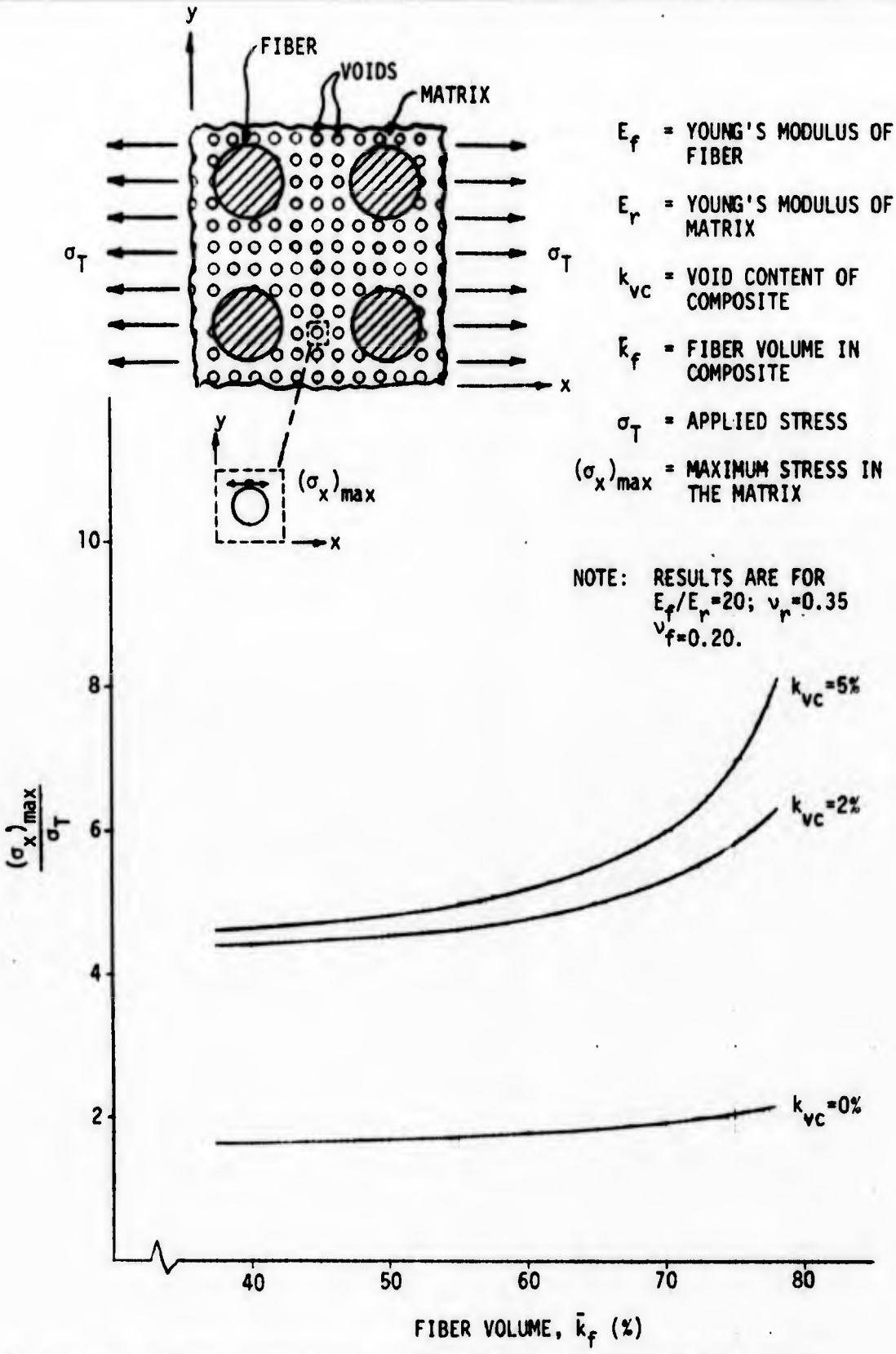

Figure 30. Interaction of Stress Concentrations from Fibers and Voids in a Composite Subjected to Transverse Loading

4.2 EXPERIMENTAL STUDIES ON FIBER-VOID STRESS INTERACTION UNDER TRANSVERSE LOADING AND TEST-THEORY COMPARISON

To establish the validity of the theory for determining the interaction of stresses from fibers and voids, large composite models were fabricated and tested in transverse tension. The test specimens consisted of a Homalite 100 matrix, aluminum disks to simulate fibers, and cylindrical voids.

Figure 31 and its accompanying table show the geometry of the test specimens for determining the interaction of stress concentrations from fibers and voids. Figure 32 shows the test setup for photoelastic measurement of stress interaction, while Figures 33 and 34 show photoelastic fringe patterns in the two specimens containing matrix, fibers, and voids.

As before (see Subsection 3.2), the photoelastic models were loaded in tension using dead weights. The load corresponding to the fringe patterns shown in Figures 33 and 34 was 871.5 lb. The stresses were measured at locations shown in Figure 31. The test results on the fiber-void stress interaction are presented in Table B-6 of Appendix B. Stresses at Locations a and e were measured as a cross-check for experimental errors. The stress concentration at Location a (single hole located away from inclusion or doubler) should be $3\sigma_1$. At Location e (in the matrix material) the stress should be equal to the applied stress, that is $\sigma_{xe} = \sigma_1$. From the results shown in Table B-6 it is seen that the stresses at locations a and e are approximately what they should be.

The experimentally obtained maximum stress concentrations in composite models containing fibers, voids, and matrix were compared with theoretical predictions. The test-theory comparison is shown in Table 5. Table 5 contains test data and two sets of theoretical results: (1) theoretical results for the problem of fiber-void stress interaction for the case when there are multiple voids between the fibers (see Figure 29) and (2) theoretical results for the case when there is a single void between adjacent fibers (Figure 31).

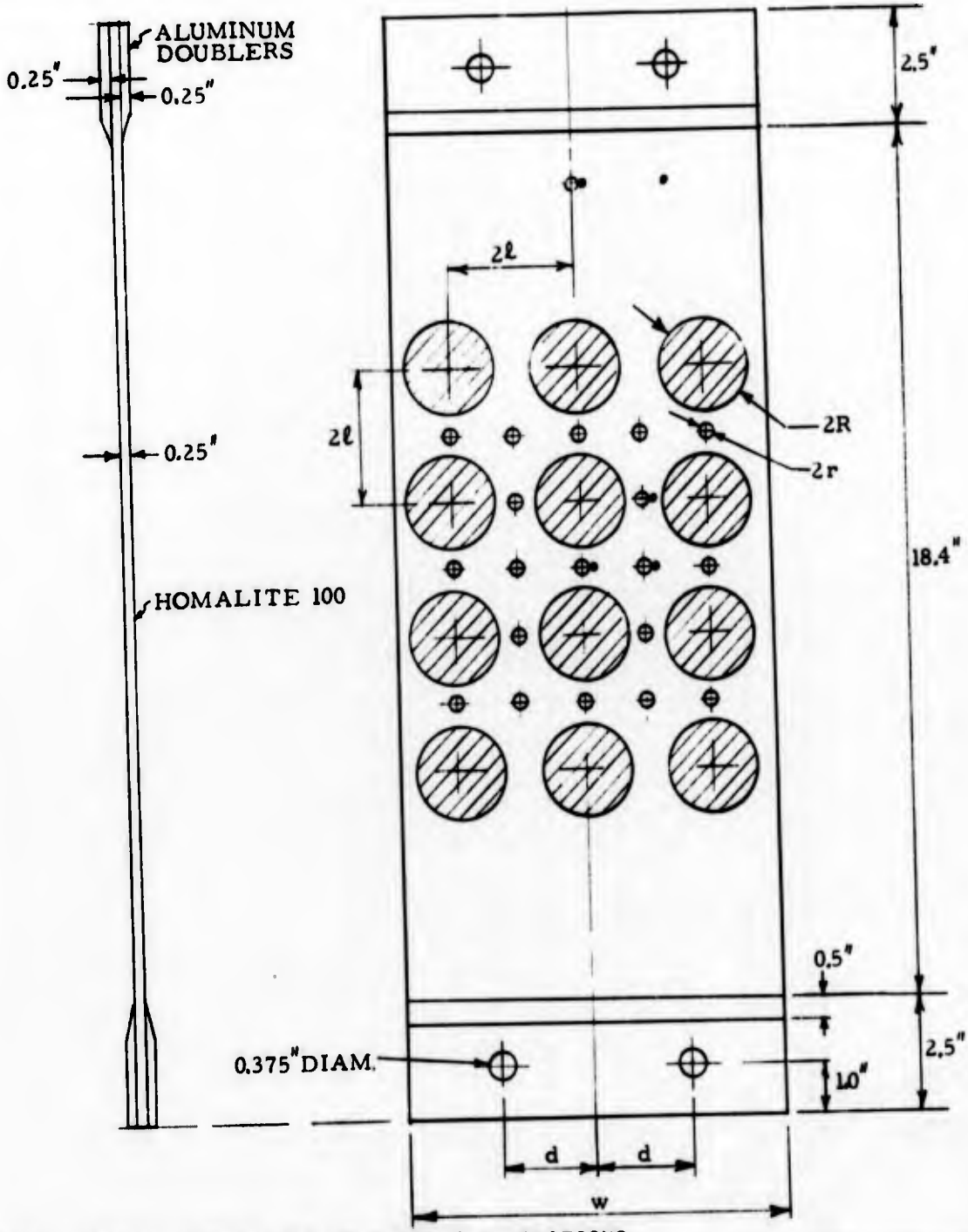

NOTE: STRESSES MEASURED AT THESE (•) LOCATIONS.

SPECIMEN	2ℓ (IN.)	2R (IN.)	2r (IN.)	d (IN.)	W (IN.)	VOID CONTENT (%)	FIBER VOLUME (%)
1	2.80	2.00	0.183	2.10	8.40	1.01	40.07
2	2.40	2.00	0.183	1.80	7.20	1.37	54.54

Figure 31. Photoelastic Test Specimen for Determining Stress Interaction from Fibers and Voids

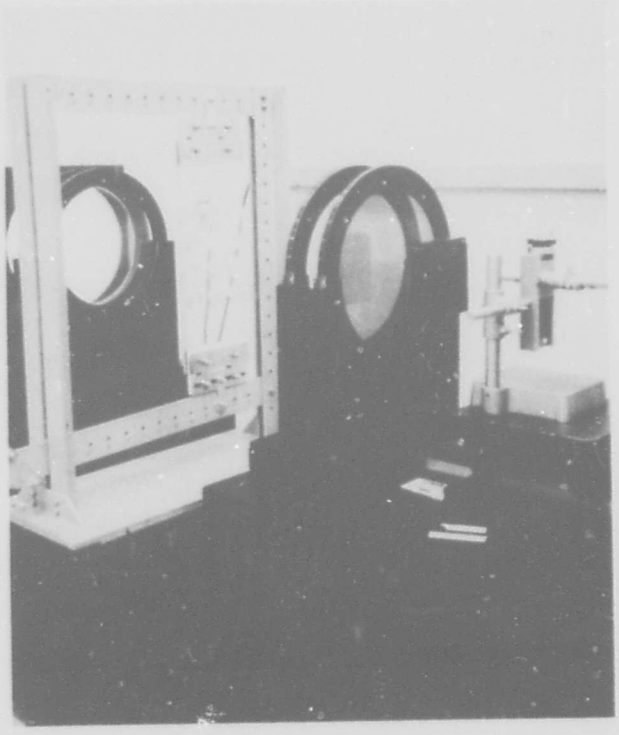

Figure 32. Photoelastic Test Setup for Determining Stress Interaction from Fibers and Voids

The solution for Case 1 was obtained using the approach given in Subsection 4.1. The solution for Case 2 was obtained as follows:

A. The effective Young's modulus of matrix between adjacent fibers and its variation in direction y was determined by reducing E_r in proportion to the area occupied by the void.

B. The load transfer between the adjacent fibers was calculated using the reduced Young's modulus of the matrix and equations given in the Appendix of Reference 1. The results of these calculations are shown in Figure 35.

C. Since stress, S, acting at a distance beyond y = 3r does not influence the stresses at y = r (see Figure A-2 and Reference 7) an average effective load acting on the element of matrix with void was calculated by numerically integrating P_x between -2r to +2r measured from the edge of the hole (or from y = +3r to y = -r from the center of the hole).

D. The average load $\overline{P}_x$ was then used in the equations of Appendix A to calculate the stress at the edge of the void located midway between the fibers.

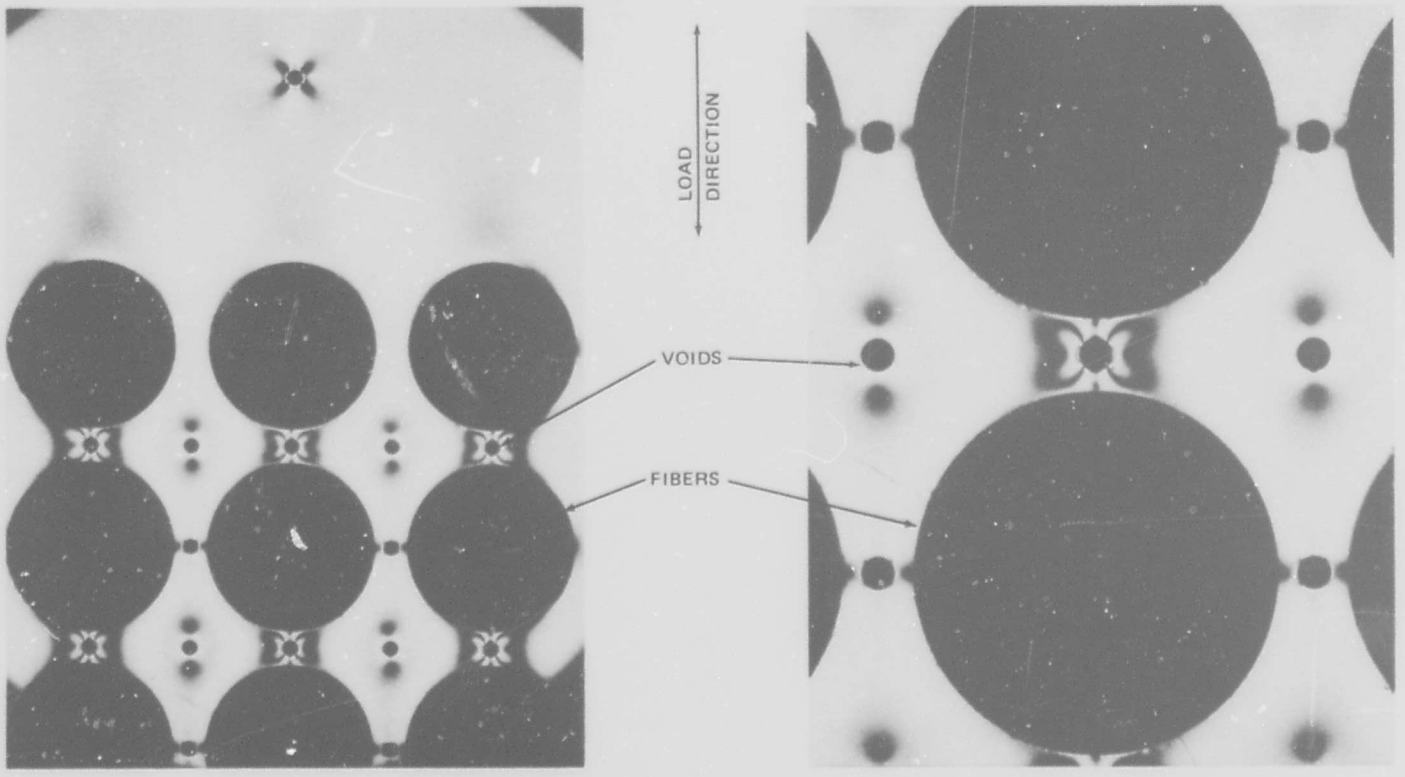

Figure 33. Photoelastic Fringe Pattern in Specimen 2 (k_{vc} = 1.37%, k_f = 54.54%)

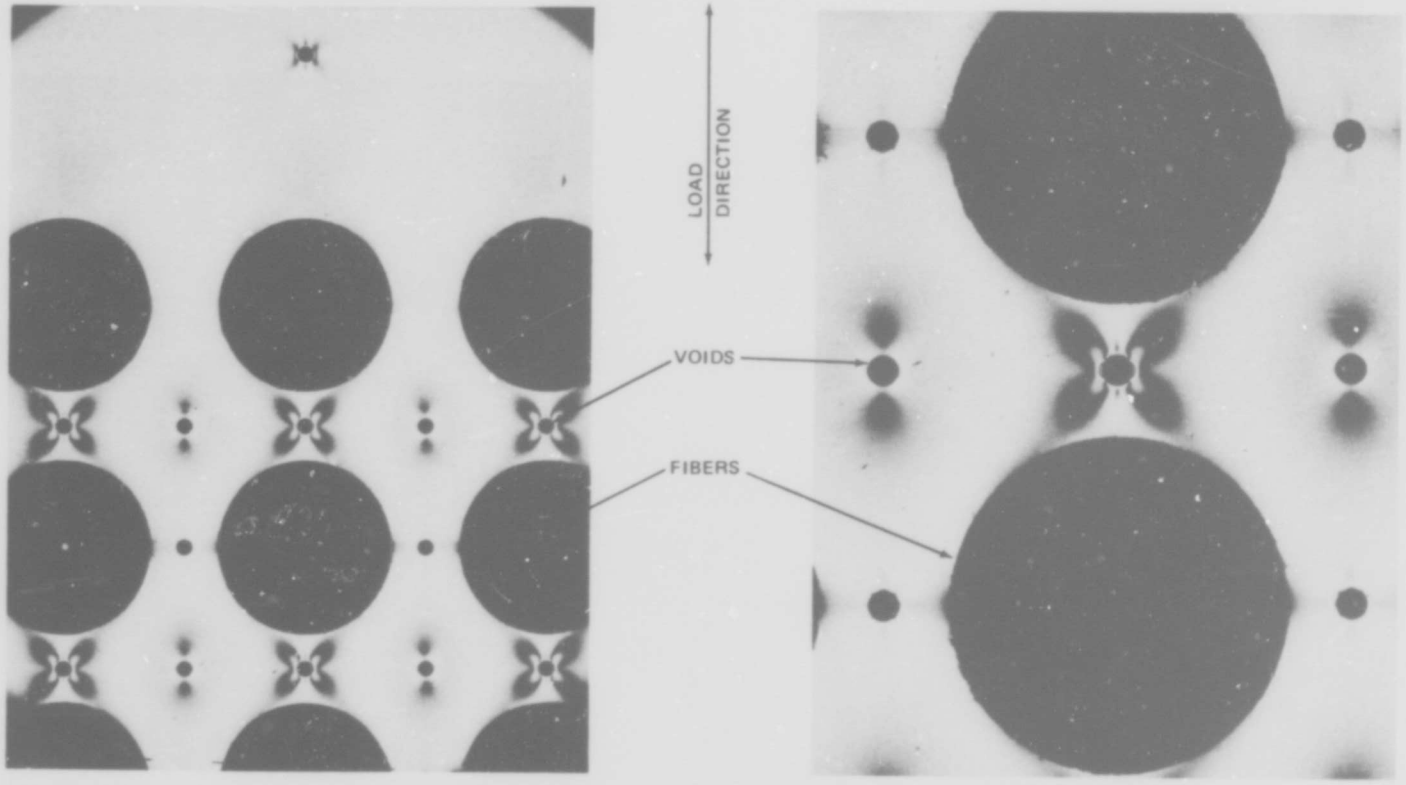

Figure 34. Photoelastic Fringe Pattern in Speciman 1 (k_{vc} = 1.01%, k_f = 40.07%

TABLE 5

TEST-THEORY CORRELATION OF FIBER-VOID STRESS INTERACTION*

LOCATION*	STRESS CONCENTRATION σ_x/σ_1 IN SPECIMEN #1 k_f = 40.07% k_{vc} = 1.01%			STRESS CONCENTRATION σ_x/σ_1 IN SPECIMEN #2 k_f = 54.54% k_{vc} = 1.37%		
	TEST	THEORY		TEST	THEORY	
		SINGLE INTERFIBER VOID	MULTIPLE INTERFIBER VOIDS		SINGLE INTERFIBER VOID	MULTIPLE INTERFIBER VOIDS
b	4.380	4.36	4.28	3.984	4.11	4.45
c	1.405	1.39	--	1.177	1.16	--

* see Table B-6 of Appendix B for locations where stress concentrations were measured.

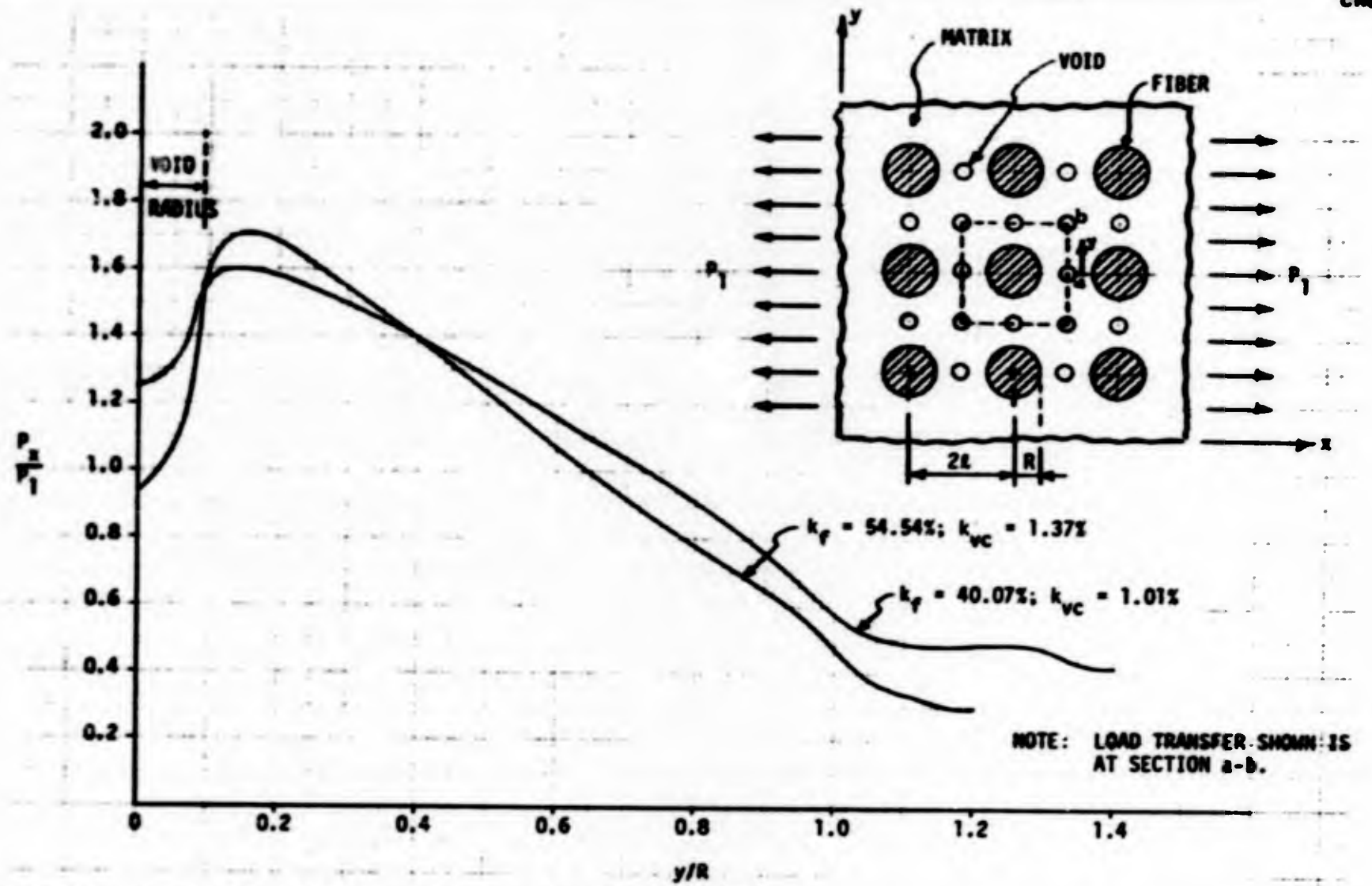

Figure 35. Interfiber Load Transfer in a Composite Containing Fibers, Voids, and Matrix

The results presented in Table 5 and in Table B-6 of Appendix B show the importance of the fiber-void stress interaction effects. The stress concentrations due to this interaction are significantly higher than the stress concentration due to fibers or voids alone. The importance of the fiber-void stress interaction is further illustrated in Figure 36.

4.3 THEORETICAL STUDIES ON FIBER-VOID STRESS INTERACTION UNDER SHEAR LOADING

If a composite consisting of fibers, voids, and matrix is subjected to in-plane shear stress τ_{LT}, the maximum stress in the matrix is approximately

$$\tau^*_{xz} \approx K_{xz} K_{xzA} \tau_{LT} \qquad (25)$$

where K_{xz} is the shear stress concentration due to fibers (given in Table 2 of Section 1) and K_{xzA} is the shear stress concentration due to voids (given by Equation 22). Figure 37 shows typical results on the fiber-void stress interaction in composites subjected to inplane shear loading. The accuracy of the results shown in Figure 37 has not yet been verified experimentally.

4.4 INFLUENCE OF UNBONDED FIBERS ON STRESS CONCENTRATIONS IN COMPOSITES SUBJECTED TO TRANSVERSE, SHEAR, OR AXIAL LOADING

If the composite contains unbonded fibers in addition to voids and fibers that are bonded to the matrix, the stress concentrations due to unbonded fibers can, as a first approximation, be assumed to be the same as the stress concentrations due to cylindrical voids.* Thus for a volume fraction of unbonded fibers = k_{if}, the resultant stresses in the matrix can be obtained from the equations given up to now, if one sets $k_{if} = k_{vc}$. For a composite containing cylindrical voids and unbonded fibers in the amounts of k_{vc} and k_{if}, respectively, the internal stresses due to both can be obtained by replacing k_{vc} with $k_{vc} + k_{if}$ in the equations that were presented.

---

* This assumption is partially justified by the results presented in Reference 8.

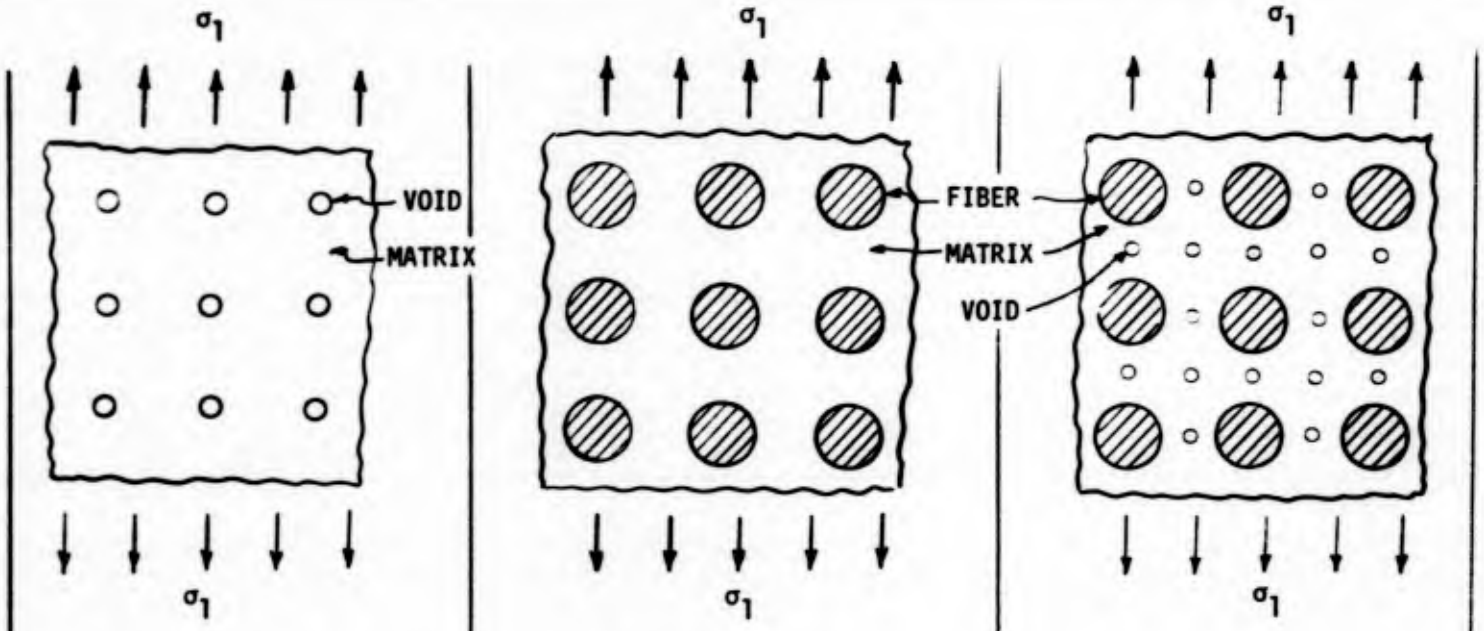

	MATERIAL WITH VOIDS ONLY k_v = 1.37%	MATERIAL WITH FIBERS ONLY k_f = 55%	MATERIAL WITH FIBERS AND VOIDS k_{vc} = 1.37%; k_f = 55%
TEST $\frac{\sigma_{max}}{\sigma_1}$	~ 3.0	1.62	3.98
THEORY $\frac{\sigma_{max}}{\sigma_1}$	3.03	1.696	4.11

Figure 36. Interaction of Stresses from Fibers and Voids

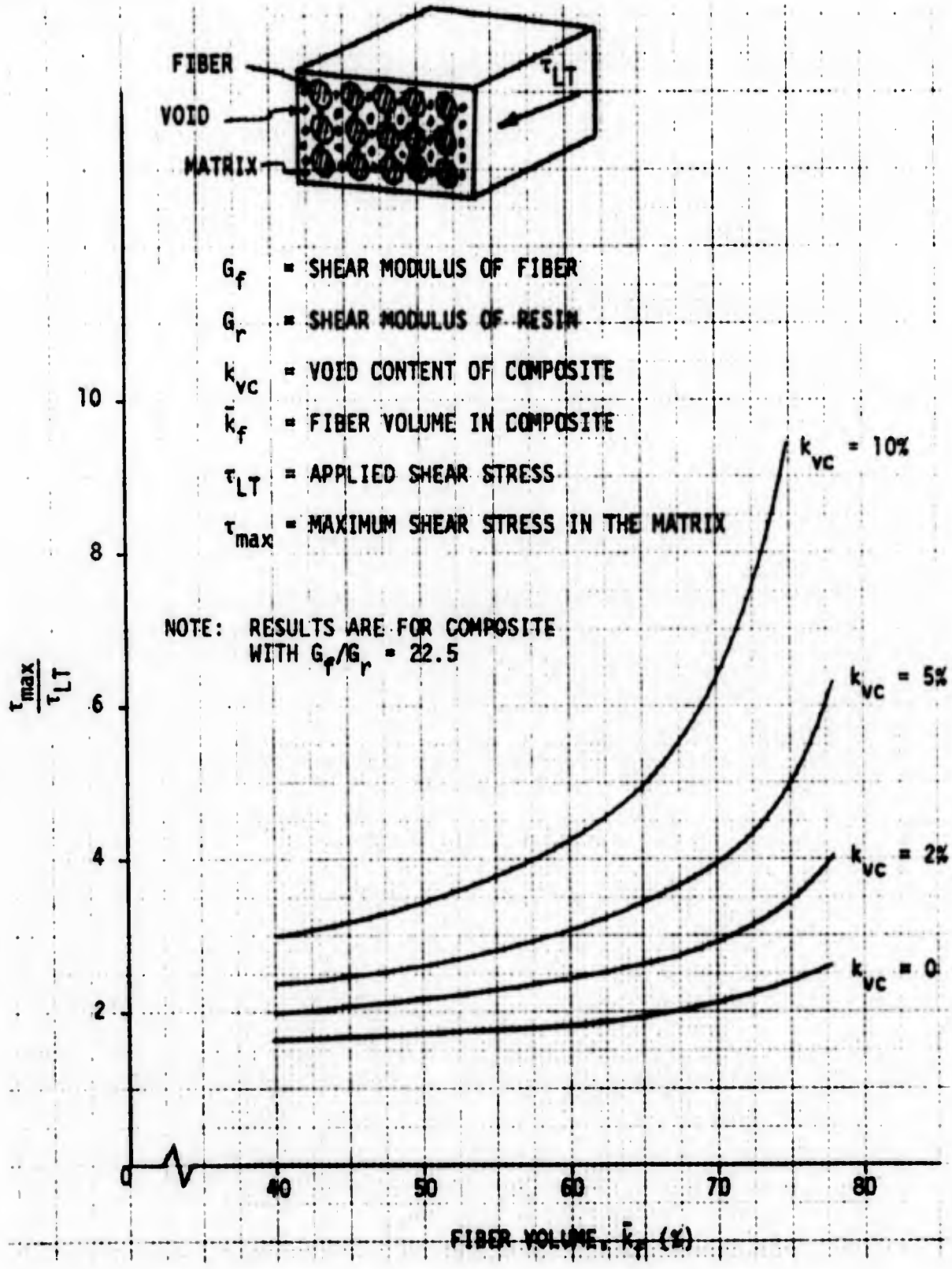

Figure 37. Interaction of Stress Concentrations from Fibers and Voids in a Composite Subjected to Shear Loading

Section 5

FAILURE CRITERIA FOR POROUS SOLIDS AND FOR COMPOSITES CONTAINING FIBERS, MATRIX, VOIDS, AND INEFFECTIVE FIBERS

Prior to formulation of failure theories for composites subjected to transverse and shear loading, studies were conducted on the failure modes of brittle and ductile matrix materials. The results of these studies were then used to formulate the failure theories for composites.

5.1 STRENGTH OF BRITTLE AND DUCTILE MATRIX AS INFLUENCED BY VOIDS

To establish the failure of a brittle matrix as influenced by porosity, specimens of the type shown in Figure 12 were fabricated and tested in tension. These specimens were made of Homalite 100, which exhibits nearly linear stress-strain behavior to failure (Figure 13).

Initially, the specimens were prepared by drilling holes (of predetermined size and spacing) in the specimens, without taking any special precautions for eliminating residual stresses. After the specimens had been prepared, examination of them under polarized light revealed the presence of residual stresses, as shown in Figure 38. Since the residual stresses are expected to influence the strength of the matrix, appropriate modifications were made in the hole drilling procedure to eliminate them. It was found that by using a carbide drill and drilling at a slow rate, while continuously dousing the end of the drill with WD40 as a coolant, resulted in test specimens that were free of any residual stresses, as shown in Figure 39. The figure shows two specimens of identical geometry and identical hole pattern. The holes in the specimen on the left side of the figure were prepared by conventional drilling, while those in the specimen on the right were prepared as described above (using an end mill and WD40). Both specimens were photographed under polarized light. It is clearly seen that the specimen on the right in Figure 39 is free of residual stresses.

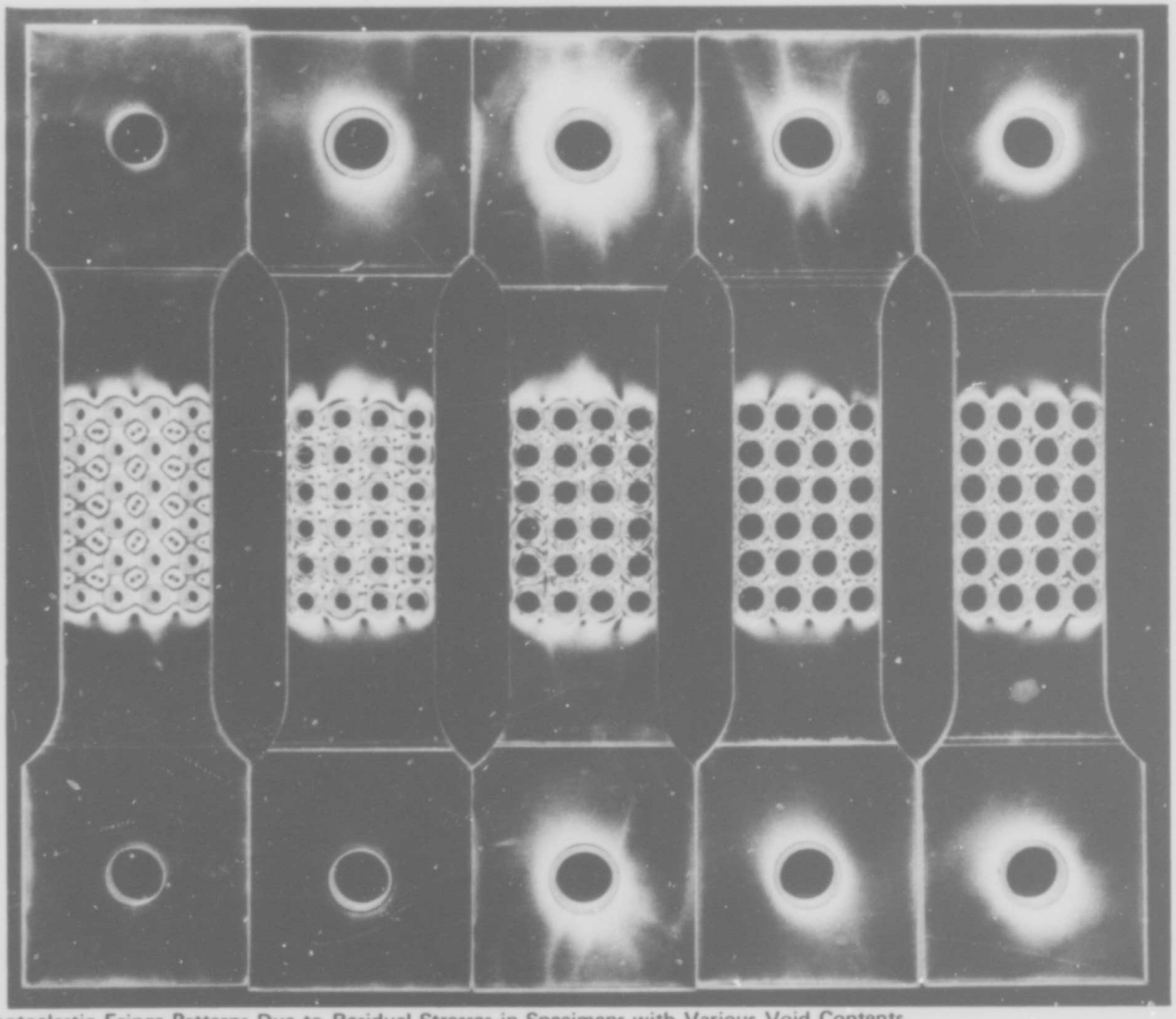

Figure 38. Photoelastic Fringe Patterns Due to Residual Stresses in Specimens with Various Void Contents

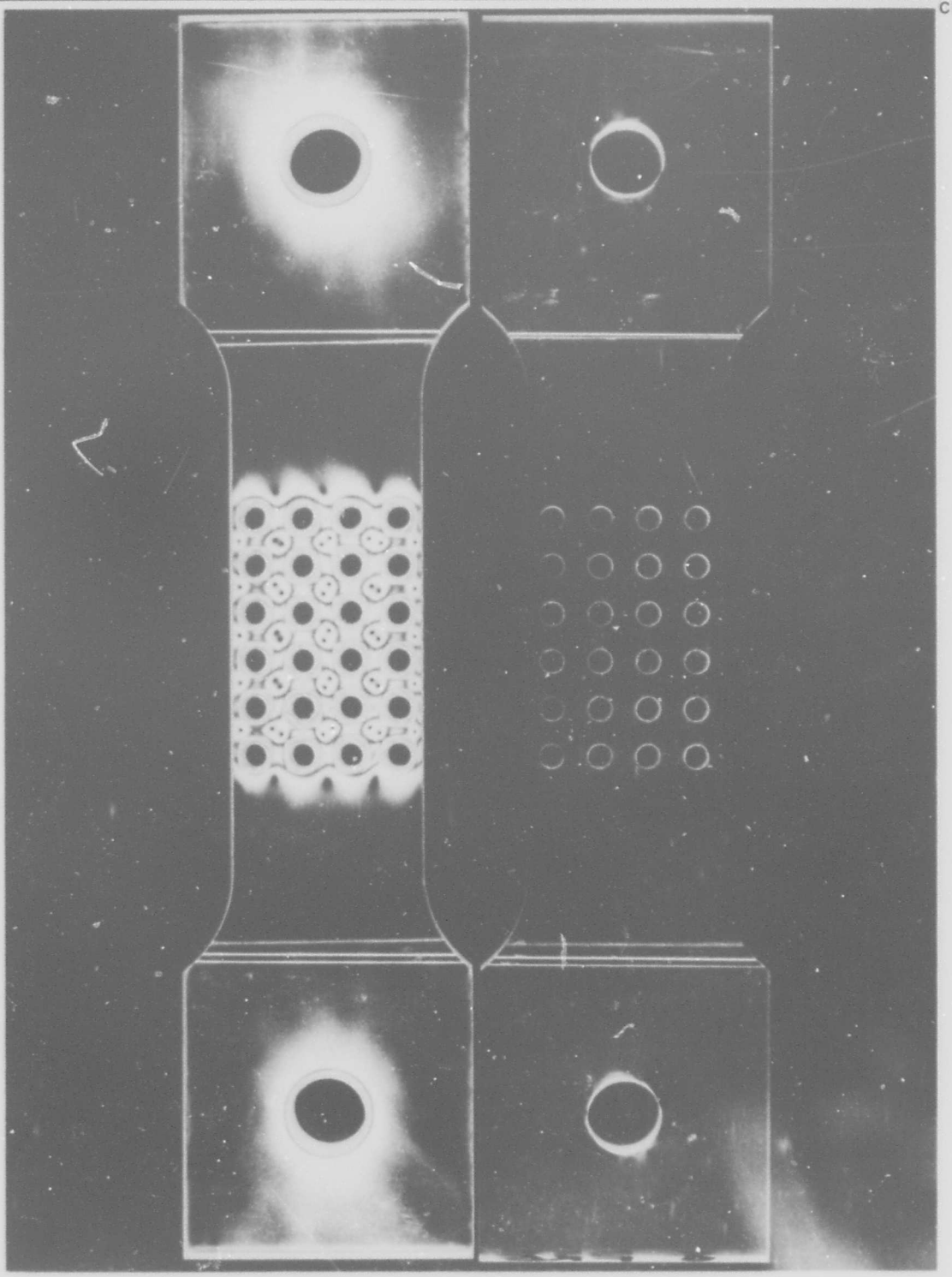

(a) (b)

Figure 39. Typical Tensile Specimens with Voids. Specimen (a) Contains Residual Stresses; Specimen (b) is Free of Residual Stresses

The test data for the tensile strengths of brittle matrix specimens with various void contents are shown in Table 4, while Table 3 shows the tensile strength data for Homalite 100 tensile coupons without any voids.

The test-theory comparison of the tensile strength of a brittle matrix containing voids is shown in Figure 40. The theoretical curve was based on a maximum stress criterion. The expression for the failure stress follows from Equation 10 and is

$$\sigma_1 = \left[2 - \left(\frac{4k_v}{\pi}\right) - \left(\frac{4k_v}{\pi}\right)^2 \right] \frac{\sigma_o}{6} \tag{26}$$

where k_v is the volume fraction of voids, σ_o is the strength of the void-free matrix, and σ_1 is the strength of the porous solid. Good agreement is shown to exist between test data and the results predicted by Equation (26), especially in the region of practical interest ($k_v \leq 30$ percent, which corresponds to void contents in actual composites of ≤ 10 percent).

Although no tests were performed on the influence of porosity on the tensile strength of a ductile matrix, test data on the above were found in Reference 8. The experimental results given in Reference 8 are for the tensile strength of aluminum plates with square arrays of circular holes. The aluminum plate models were similar to the models made of Homalite 100 and shown in Figure 12. The test data as well as the theoretical prediction of the tensile strength of ductile material are shown in Figure 41. The theoretical curve was obtained from the following elementary equation

$$\sigma_1 = \left(1 - \sqrt{\frac{4k_v}{\pi}}\right) \sigma_o \tag{27}$$

where σ_1 is the tensile strength of the solid with voids, σ_o is the ultimate tensile strength of the void-free solid, and k_v is the volume fraction of voids. Each data point shown in Figure 41 is an average of two tests. Equation 27 applies to materials exhibiting elastic-plastic behavior. The normalized tensile strength of brittle and ductile materials as influenced by porosity is shown in Figure 42, where it can be seen that for materials with low void contents, ductility of the matrix has a significant influence on its strength.

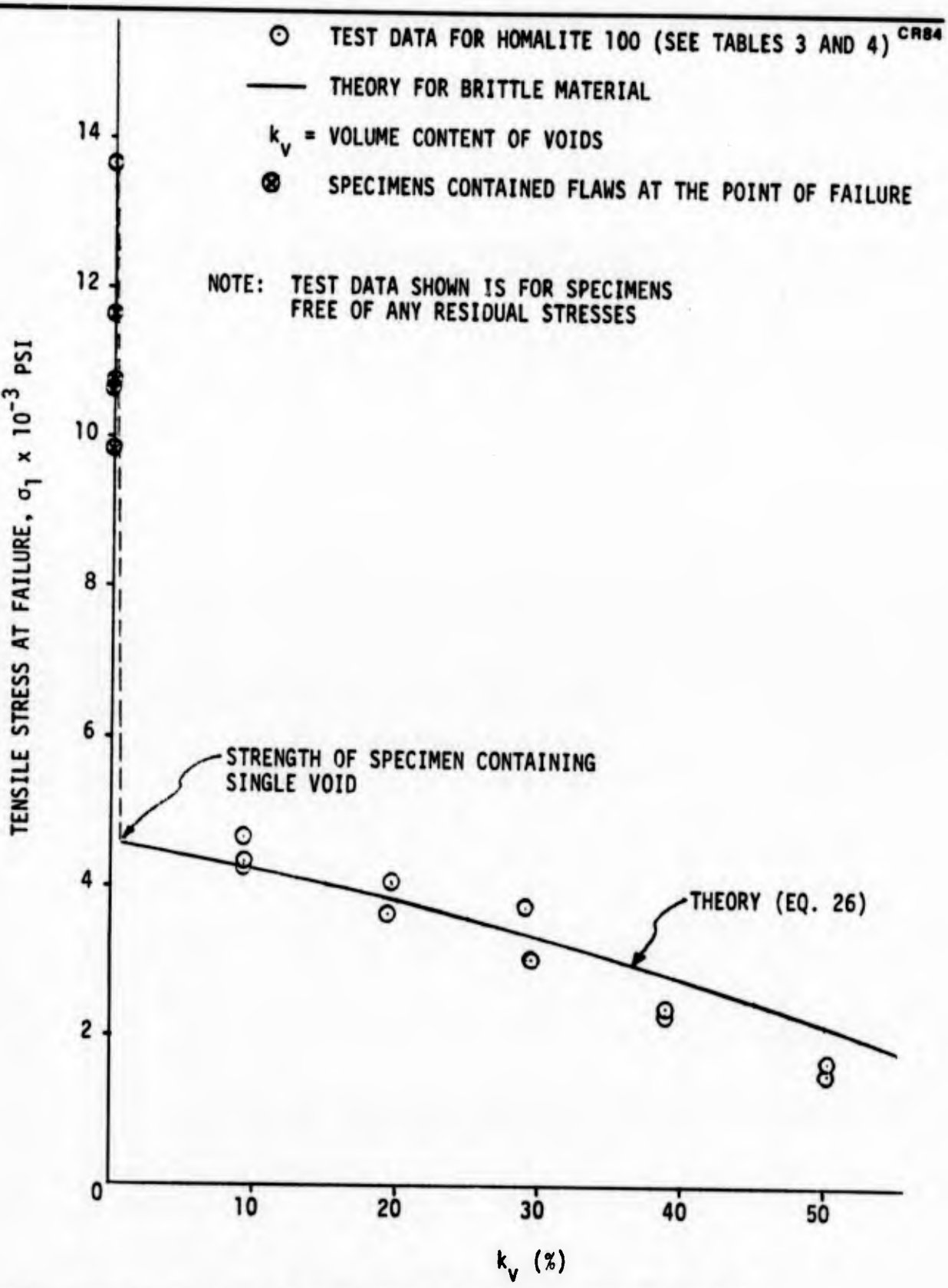

Figure 40. Test-Theory Comparison of Tensile Strength of Brittle Matrix Containing Cylindrical Voids Arranged in Square Array

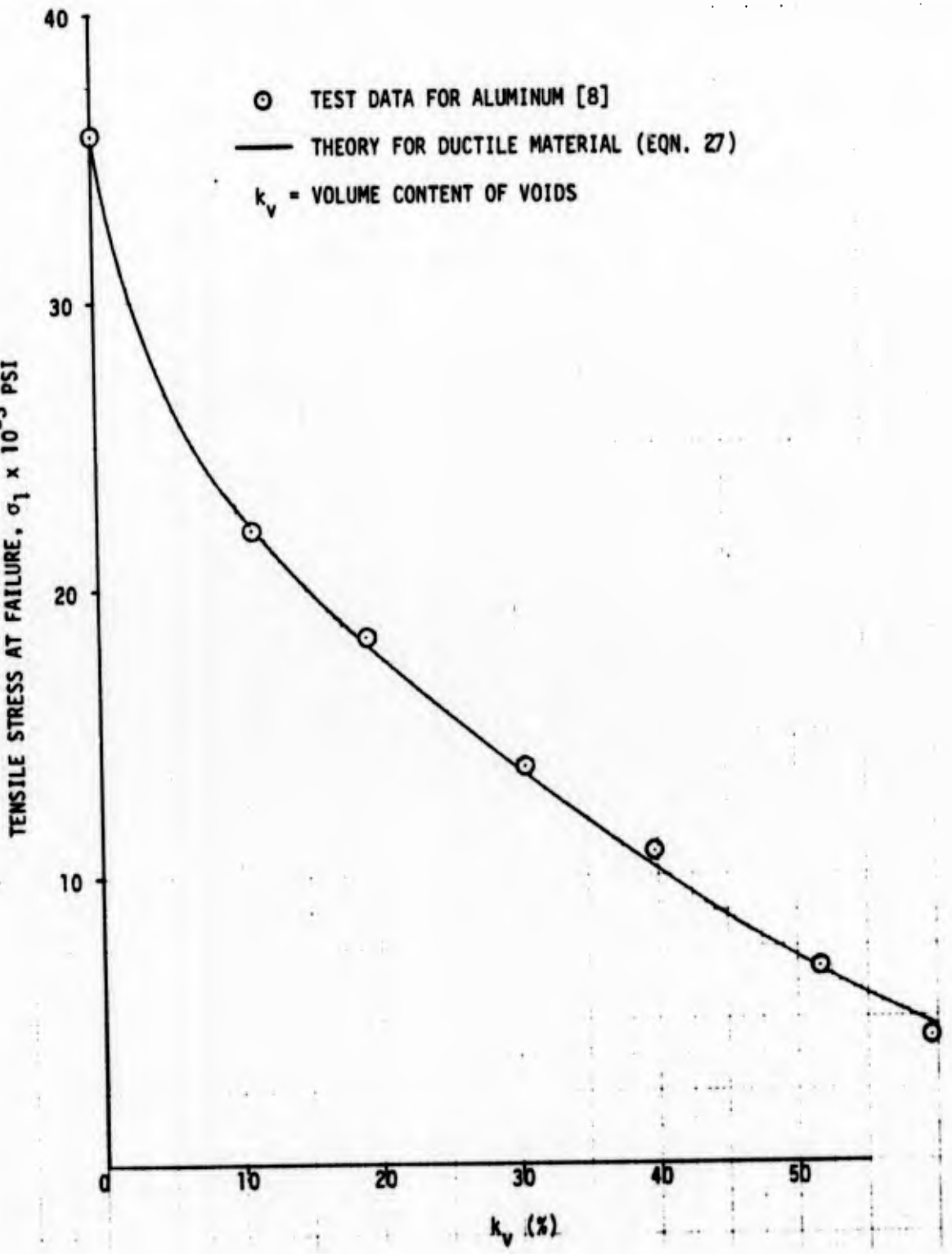

Figure 41. Test-Theory Comparison of Tensile Strength of Ductile Material Containing Cylindrical Voids Arranged in Square Array

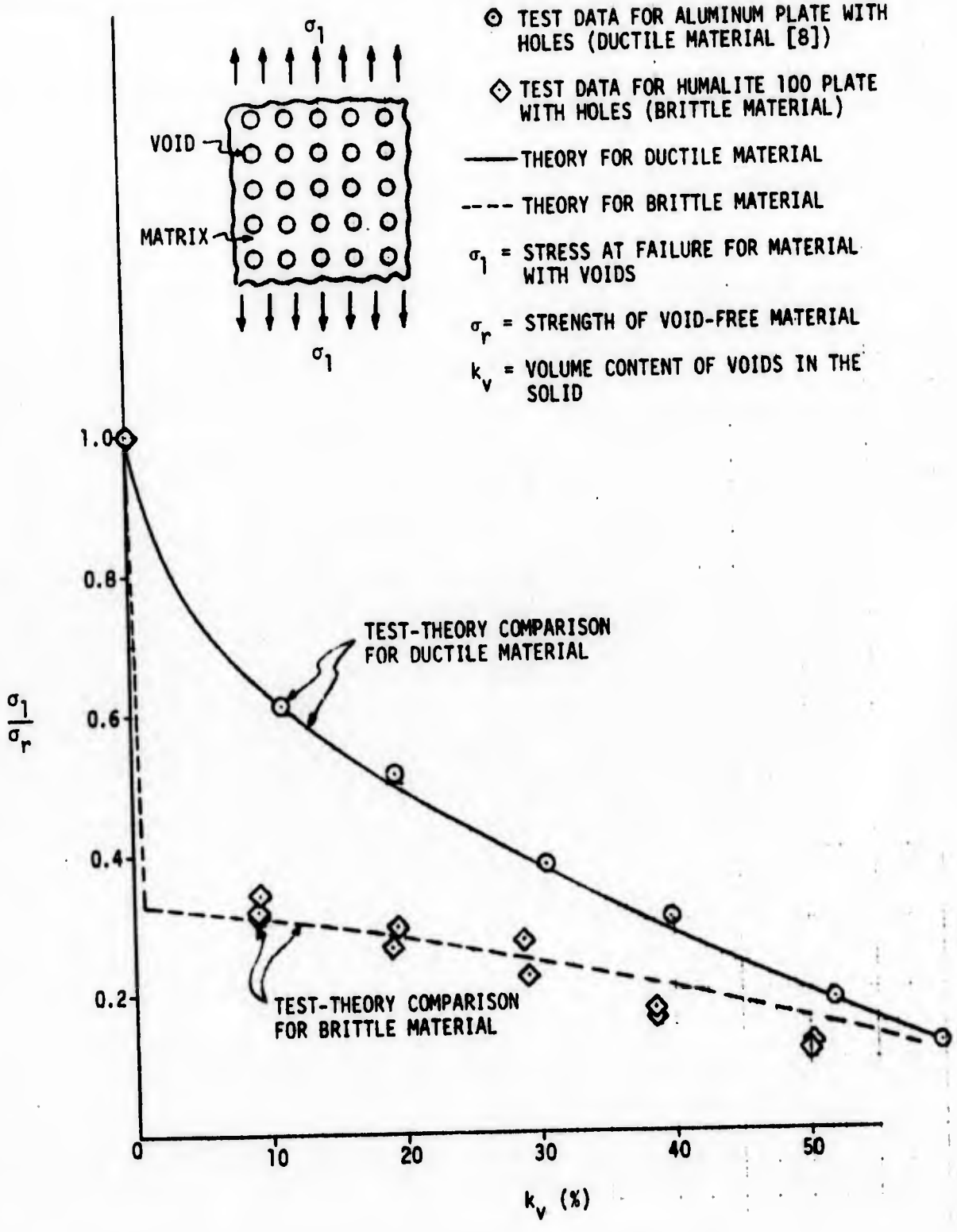

Figure 42. Influence of Porosity on Tensile Strength of Ductile and Brittle Materials

5.2 TRANSVERSE TENSILE STRENGTH OF COMPOSITES

The results presented above have been incorporated in the equations for predicting the transverse tensile strength of composites. For the case of a composite made with a brittle matrix and containing voids and unbounded fibers, the equation for transverse strength of such a composite is

$$\sigma_T^* = \frac{\sigma_r}{\bar{K}_{xr} K_x^* + \bar{K}_{yr} K_y^*} \tag{28}$$

where σ_r is the tensile strength of the resin, σ_T^* is the tensile strength of the composite, and K_x^* and K_y^* are the stress concentration factors due to fibers, and can be obtained from Table 1. These factors are evaluated for E_f/E_r^* where E_r^* is the Young's modulus of the resin containing voids, and is given in Figure 9.

The two remaining terms, $\bar{K}_{xr}$ and $\bar{K}_{yr}$ are the stress concentration factors due to voids, and can be obtained from Equations 10 and 17, respectively, by substituting λ^* for λ where

$$\lambda^* = \sqrt{\frac{4\left(k_{vc}+\bar{k}_{if}\right)}{\pi\left|1-\left(\bar{k}_f-\bar{k}_{if}\right)\right|}} \tag{29}$$

and

k_{vc} = void content in a composite
$\bar{k}_{if}$ = volume fraction of unbonded or ineffective fibers
$\bar{k}_f$ = total volume fraction of fibers in a composite

The term λ^* essentially gives the nondimensional void and/or ineffective fiber spacing in a porous resin reinforced with fibers, whereas λ gives the nondimensional void spacing in a matrix that does not contain any fibers. In deriving Equation 28 it was assumed that the composite contained at least one critical void. In view of this assumption

$$\frac{\sigma_T^*}{\sigma_r} \neq 1$$

if k_{vc}, $\bar{k}_{if}$ and $\bar{k}_{f}$ are set equal to zero.

Since the matrix materials used in actual composites do exhibit some ductility (see Figures 45, 46, and 47 of Section 6), a failure criterion was also formulated for the transverse strength of composites made with a non-brittle matrix. Here use is made of the Hencky-von Mises distortion energy criterion to account for interaction of triaxial stresses in the matrix of a composite subjected to transverse loading. Even though the latter criterion actually predicts yield stresses rather than strength, it can be modified and used to predict failure of many materials as discussed in Reference 19. For an isotropic solid subjected to triaxial stresses the Hencky-von Mises criterion is (Reference 20)

$$F^2 = \sigma_x^2 + \sigma_y^2 + \sigma_z^2 - \left(\sigma_x\sigma_z + \sigma_x\sigma_y + \sigma_y\sigma_z\right) \tag{30}$$

where σ_x, σ_y, and σ_z are the triaxial stresses acting on the solid, and F is the yield stress, or the uniaxial tensile strength of the material if Equation 30 is used to predict failure. The criterion as given by Equation 30 is not directly applicable for predicting the strength of filamentary composites subjected to transverse loading, since such composites are orthotropic. The problem of material orthotropy can be resolved by applying the criterion to the internal triaxial stresses in the matrix, which result when a composite is subjected to transverse loading. Using this approach, the following equation is obtained for predicting the transverse tensile strength of composites

$$\begin{aligned}\sigma_T^* = \sigma_r \Big|&\left(\bar{K}_{xA}^* K_x^* + K_{yD}^* K_y^*\right)^2 + \left(K_{xD}^* K_y^* + K_{yA}^* K_x^*\right)^2 \\ &+ \left(K_{zr}^* K_z^*\right)^2 - \Big|\left(\bar{K}_{xA}^* K_x^* + K_{yD}^* K_y^*\right)\left(K_{xD}^* K_y^*\right. \\ &\left. + K_{yA}^* K_x^*\right) + K_{zr}^* K_z^*\left(\bar{K}_{xA}^* K_x^* + K_{yD}^* K_y^*\right) \\ &+ K_{zr}^* K_z^*\left(K_{xD}^* K_y^* + K_{yA}^* K_x^*\right)\Big|\Big|^{-1/2}\end{aligned} \tag{31}$$

where σ_r is the uniaxial tensile strength of the matrix, σ_T^* is the transverse tensile strength of the composite, K_x^*, K_y^*, and K_z^* are the triaxial stress concentrations due to fibers, and the remaining terms are the stress concentrations due to voids and ineffective fibers. The values of K_x^*, K_y^*, and K_z^* can be obtained from Table 1. The asterisk (*) used in these terms denotes that they have to be evaluated for E_f/E_r^* where E_r^* is the Young's modulus of the matrix containing voids. The remaining terms ($\overline{K}_{xA}^*$, K_{yD}^*, K_{xD}^*, K_{yA}^*, and K_{zr}^*) can be obtained from equations given in Section 3, modified according to Equation 29. The final expressions for these terms are

$$\overline{K}_{xA}^* = \frac{1}{1-\lambda^*} \tag{32}$$

$$K_{yD}^* = \left(\frac{1-\lambda^*}{2}\right)\left[(\lambda^*)^2 - \frac{3}{4}(\lambda^*)^4\right]\xi^* \tag{33}$$

$$K_{xD}^* = \left(\frac{1-\lambda^*}{2}\right)\left[2 - 5(\lambda^*)^2 + 3(\lambda^*)^4\right]\xi^* \tag{34}$$

$$K_{yA}^* = \frac{3\left[(\lambda^*)^2 - (\lambda^*)^4\right]}{2 - (\lambda^*)^2 - (\lambda^*)^4} \tag{35}$$

$$K_{zr}^* = \frac{1}{1 - \frac{\pi}{4}(\lambda^*)^2} \tag{36}$$

where λ^* is given by Equation 29 and is a function of void content, fiber volume fraction, and volume fraction of unbonded or ineffective fibers. The term ξ^* can be obtained from Equation 19 by substituting $\lambda = \lambda^*$ in the latter equation. Inasmuch as the tensile failure of a non-brittle material containing voids and subjected to transverse loading was found to be governed by the maximum average stress[†] acting on the ligament of matrix between two adjacent voids (see Figure 41 and Equation 27), use was therefore made of Equation 32 for the transverse stress concentration due to voids rather than of Equations 8 or 10, which give the stresses at the void boundary and midway between the voids. Equation 32 can be obtained from consideration of force

[†] Average stress at the point where the width of the matrix between two adjacent voids is minimum. The average stress at that point is maximum.

equilibrium at the point of interest, or by integrating σ_x, given by Equation A-30, between the limits y = R and y = ℓ, and dividing the result by (ℓ - R).

Having the expressions for the various terms appearing in Equation 31, the latter can be used to predict the transverse tensile strength of fiber-reinforced composites containing fibers, voids, and unbonded or ineffective fibers. If the composite contains no voids or ineffective fibers, it can be readily shown that

$$\left.\begin{aligned} \overline{K}^{\circ}_{xA} &= K^{\circ}_{xD} = K^{\circ}_{zr} = 1 \\ K^{\circ}_{yD} &= K^{\circ}_{yA} = 0 \\ K^{\circ}_{x} &= K_x \\ K^{\circ}_{y} &= K_y \\ K^{\circ}_{z} &= K_z \end{aligned}\right\} \qquad (37)$$

and Equation 31 reduces to

$$\sigma^{\circ}_{T} = \sigma_r \left\{K_x^2 + K_y^2 + K_z^2 - \left(K_x K_y + K_z K_x + K_z K_y\right)\right\}^{-1/2} \qquad (38)$$

which is the transverse tensile strength of the composite with no voids or unbonded fibers. The terms K_x, K_y, and K_z given in the above equation can be obtained directly from Table 1. If the material contains only voids and no fibers, then

$$K^{\circ}_{x} = 1,\ K^{\circ}_{y} = K^{\circ}_{z} = 0,\ \lambda^{\circ} = \lambda,\ k_{vc} = k_v$$

and Equation 31 reduces to

$$\sigma_T^{\circledast} = \bar{K}_{xA}\,\sigma_r\left[1 + \frac{K_{yA}}{\bar{K}_{xA}}\left(\frac{K_{yA}}{\bar{K}_{xA}} - 1\right)\right]^{-1/2} \tag{39}$$

or

$$\sigma_T^{\circledast} = \bar{K}_{xA}\,\sigma_r = \left(1 - \sqrt{\frac{4k_v}{\pi}}\right)\sigma_r \tag{40}$$

Since

$$\frac{K_{yA}}{\bar{K}_{xA}} = \frac{3(\lambda^2 - \lambda^4)(1 - \lambda)}{2 - \lambda^2 - \lambda^4} = \frac{3\lambda^2(1 - \lambda)}{2 + \lambda^2}$$

and

$$\frac{K_{yA}}{\bar{K}_{xA}}\left(\frac{K_{yA}}{\bar{K}_{xA}} - 1\right) \ll 1$$

Equation 40 is identical to Equation 27.

Typical results for the transverse tensile strength of composites made with brittle and ductile matrix materials are shown in Figure 43. These results were calculated from Equations 28 and 31. An example of applying Equation 31 to predict the transverse tensile strength of composites is given in Appendix C.

5.3 SHEAR STRENGTH OF COMPOSITES

An approach similar to that presented in the previous section was employed to predict the shear strength of composites from the properties of their constituents and the composite's microstructure. The equation for the shear strength of a composite is

$$\tau_{LT}^{\circledast} = \frac{\tau_r}{K_{xz}^{\circledast}\,K_{xzA}^{\circledast}} \tag{41}$$

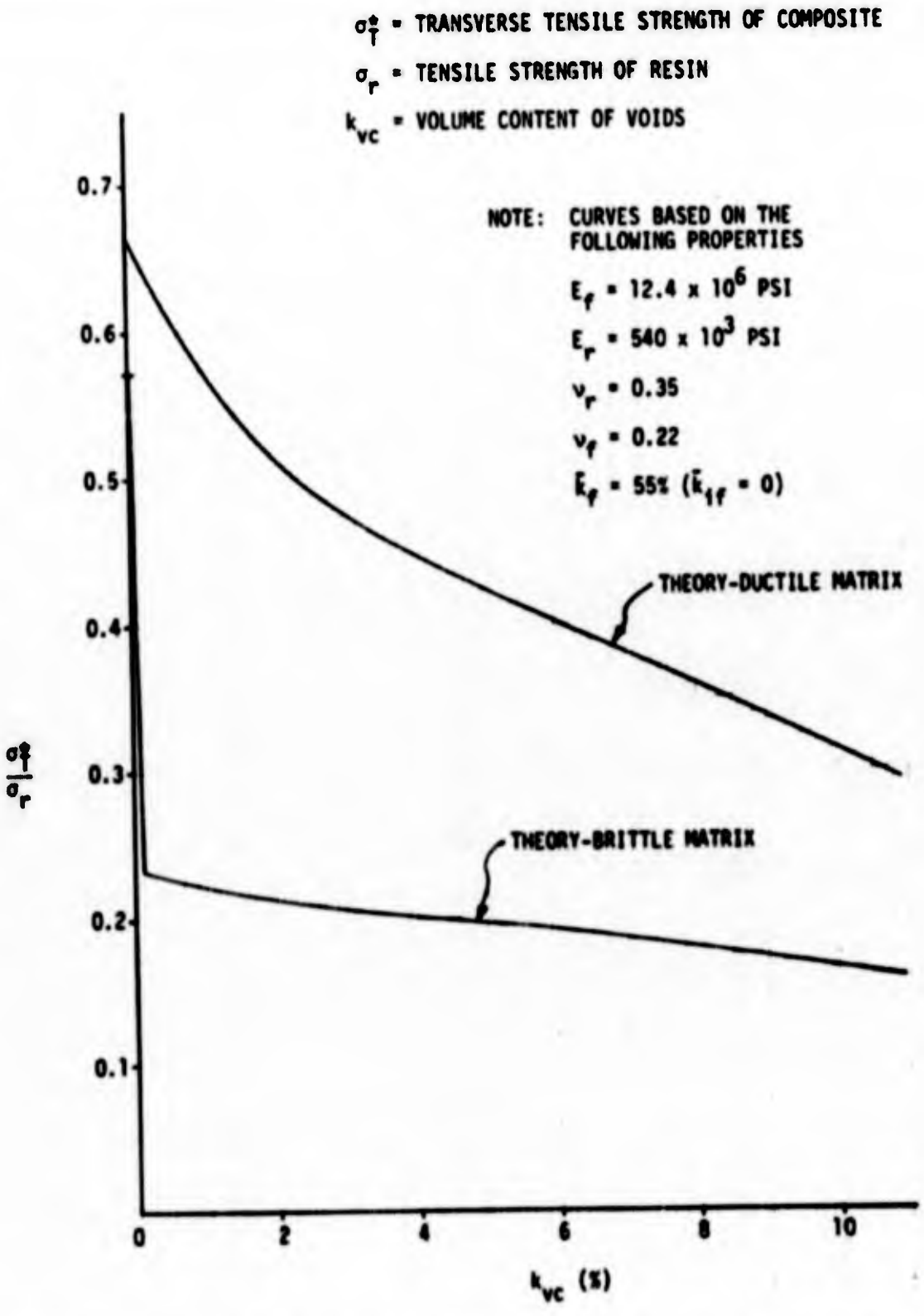

Figure 43. Typical Theoretical Results for the Transverse Tensile Strength of Composites as Influenced by Porosity, Matrix Ductility, and Resin Strength

where τ_r is the shear strength of the matrix and K^*_{xz} is the shear stress concentration due to fibers, and can be obtained from Table 2.

$$K^*_{xz} = \frac{\tau_M}{\tau_{LT}}$$

As before, the asterisk (*) denotes that K^*_{xz} has to be evaluated for G_f/G^*_r, where G^*_r is the effective shear modulus of the matrix with voids, and is given in Figure 10. The term K^*_{xzA} appearing in Equation 41 is the shear stress concentration due to voids or unbonded fibers, and can be obtained by combining Equations 22 and 29

$$K^*_{xzA} = \left\{ \frac{1}{1 - \left[\frac{4\left(k_{vc} + \bar{k}_{if}\right)}{\pi\left[1 - \left(\bar{k}_f - \bar{k}_{if}\right)\right]} \right]^{1/2}} \right\} \qquad (42)$$

Typical results for the predicted shear strength of composites are shown in Figure 44.

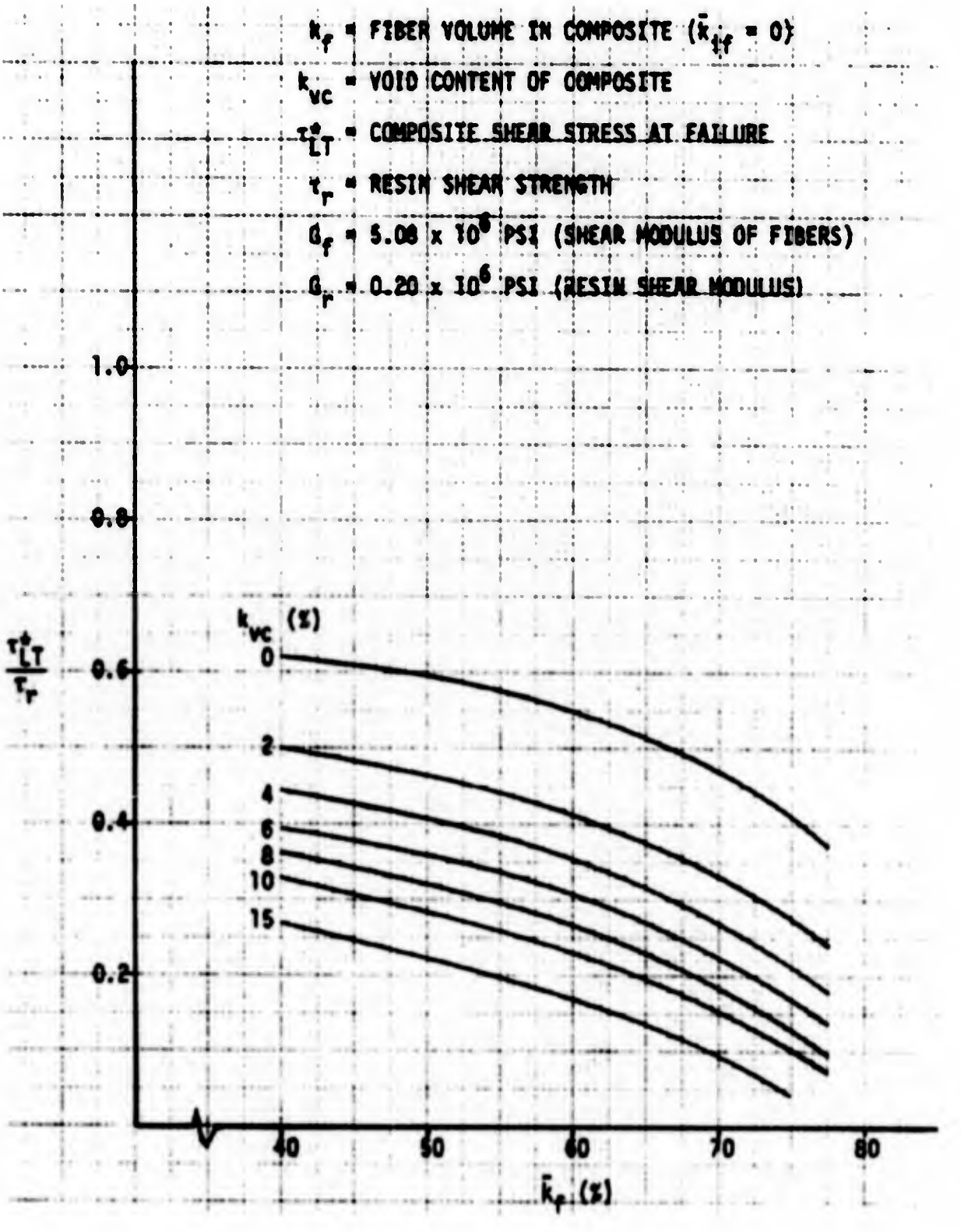

Figure 44. Typical Theoretical Results for the Shear Strength of Composites as Influenced by Porosity, Constituent Properties, Fiber Content, and Resin Shear Strength

Section 6

FABRICATION AND TESTING OF ACTUAL COMPOSITES FOR VERIFICATION OF FAILURE THEORIES

To establish the accuracy of the failure theories for predicting the transverse and shear strength of composites, 24 unidirectional composite panels were fabricated, and appropriate test specimens were prepared from the various panels. Three different types of fibers and two different resins were employed in fabricating the panels: S-glass fibers, Modmor II graphite fibers, boron fibers, 1004 epoxy resin, and SC1008 phenolic resin. In addition to the above, resin castings were prepared and tested to characterize the matrix materials.

6.1 MATRIX MATERIALS AND THEIR PROPERTIES

The matrix materials were characterized for specific gravity, ultimate tensile strength, Young's modulus, Poisson's ratio, and ultimate strain to failure. Moreover, stress-strain curves were obtained for the two resin systems, 1004 epoxy resin and SC1008 phenolic resin. The test specimens were prepared from resin castings. The 1004 epoxy resin casting was prepared by stacking layers of resin film (≈ 3 inch wide by 0.005 inch thick) in a mold, pulling the vacuum on the mold with resin, and heating the mold at 2 degrees per minute to 350°F. The resin was cured for 2 hours at 350°F. Dog-bone-shaped tensile coupons with provisions for pin loading were then machined from the resin casting. Inasmuch as specimen preparation and detailed characterization of SC1008 phenolic was not planned in this program, SC1008 resin castings* available from some previous work performed at MDAC were used for making the test specimens. In addition to dog-bone-shaped tensile

* The casting was made by placing the resin in a mold, slowly raising the temperature from 70°F to ~300°F over a 7-day period, curing the resin at ~300°F for 3 hours, and cooling the casting in the oven over 1.5-day period. This cure cycle was found necessary to obtain void-free resin castings.

specimens, specimens with square cross sections were also prepared for measuring the resin shear strength. Moreover, several of the specimens made with SC1008 resin were post-cured at 350°F for 4 hours to establish the influence of post-curing on the resin properties.

The measured properties of the two resins are given in Table D-1 of Appendix D and summarized in Table 6. Both strain gages and a lightweight Instron extensometer were used to determine the Young's moduli of the resins. The Young's moduli obtained with strain gages were somewhat higher than those obtained with the Instron extensometer. The strain gages were found to have a significant influence on the tensile strength of resins. The tensile strength of specimens instrumented with strain gages was found to be ≈ 34 to 52 percent lower than the tensile strength of specimens without strain gages. Table 7 shows the influence of strain gages on the tensile strength of resin, and on the tensile strength of Homalite 100. It is noted here that all the specimens for which data are presented failed in the test section.

Typical stress-strain curves for the 1004 epoxy resin, SC1008 phenolic resin, and post-cured SC1008 phenolic resin are shown in Figures 45, 46, and 47.

6.2 FIBER MATERIALS AND THEIR PROPERTIES

Three types of reinforcing fibers were used to make the composites: S-glass fibers, Modmor II graphite fibers, and boron fibers. No tests were conducted on the properties of the fibers, so these were obtained from the literature, primarily from Reference 10. The fibers and their properties are summarized in Table 8.

6.3 FABRICATION OF COMPOSITE SPECIMENS

In order to verify the failure criteria, unidirectional composite specimens were prepared from various combinations of fibers and resins. The various specimens were made from flat panels having unidirectional fiber orientation. Both filament winding and prepregs were used to make the panels. The composites made of S-glass and 1004 epoxy resin were made by winding filaments of glass rovings onto a mandrel covered with a thin film of 1004 epoxy, taking the resultant prepreg off the mandrel, cutting it up into squares ≈ 8 inch by 8 inch, and stacking these squares in a mold. The assembly was

TABLE 6

AVERAGE PROPERTIES OF RESINS

MATERIAL	SPECIFIC GRAVITY	TENSILE PROPERTIES				SHEAR PROPERTIES	
		YOUNG'S MODULUS (10^{-6}psi)	POISSON'S RATIO	STRENGTH X 10^{-3}	FAILURE STRAIN (%)	SHEAR MODULUS† X 10^{-6}psi	SHEAR STRENGTH
CAST 1004 EPOXY	1.255	0.537	0.347	11.95	>2.8	0.200	--
CAST SC1008 PHENOLIC	1.22	0.559	0.352	11.88	4.9	0.207	>12.62*
CAST AND POST CURED SC1008 PHENOLIC	1.22	0.645	--	16.26	>2.7	0.238††	--

† Calculated from $G=E/2(1+\nu)$

†† Based on $\nu=0.352$

* Distance between grips was ~0.4 inches; data not considered valid because of the possible end effects.

TABLE 7

INFLUENCE OF STRAIN GAGES ON THE TENSILE STRENGTH OF RESIN

MATERIAL	TENSILE STRENGTH X 10^{-3} psi		% STRENGTH REDUCTION DUE TO STRAIN GAGE (AVERAGE)
	SPECIMEN WITH STRAIN GAGE	SPECIMEN WITHOUT STRAIN GAGE	
1004 Epoxy	7.345 8.520	11.690 12.770 11.400	33.6
SC1008 Phenolic	6.610	11.460 11.810 11.565 11.540 11.545 11.655	43.0
Homalite 100	4.420 6.550 5.850 4.910	10.620 13.660 11.630 9.810 10.780	51.9

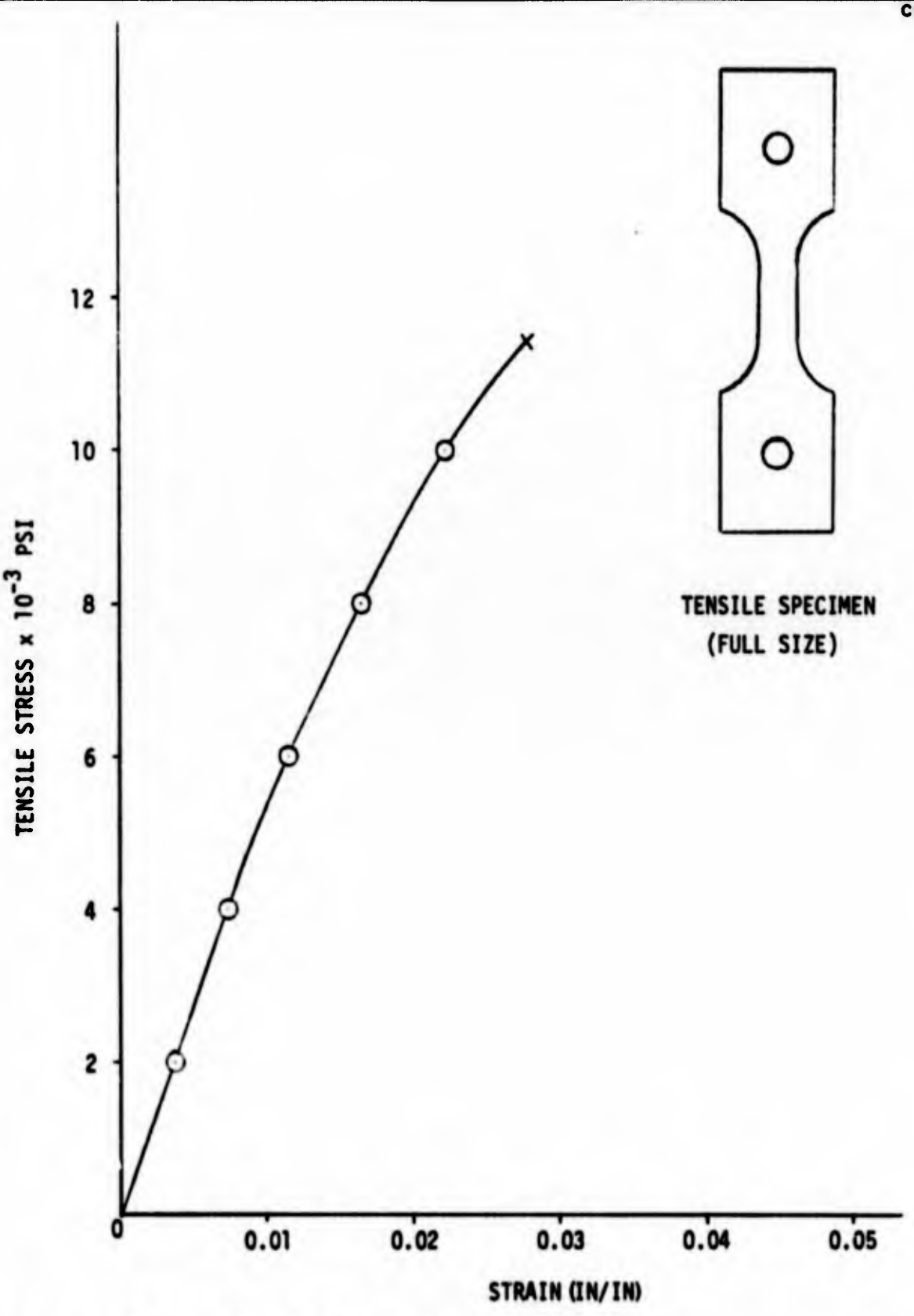

Figure 45. Typical Stress-Strain Curve for Cast Epoxy 1004 Resin

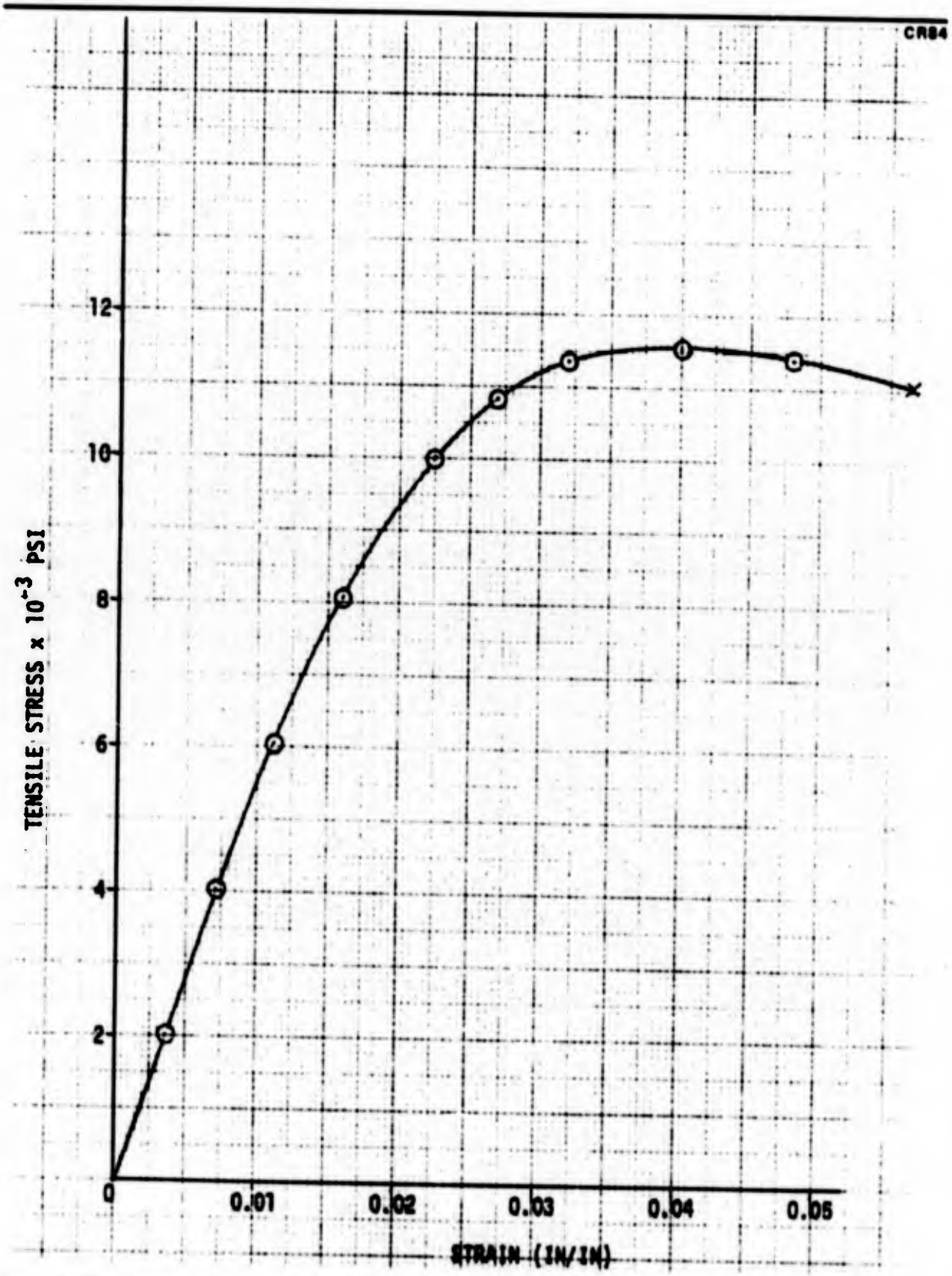

Figure 46. Typical Stress-Strain Curve for Cast SC1008 Phenolic Resin

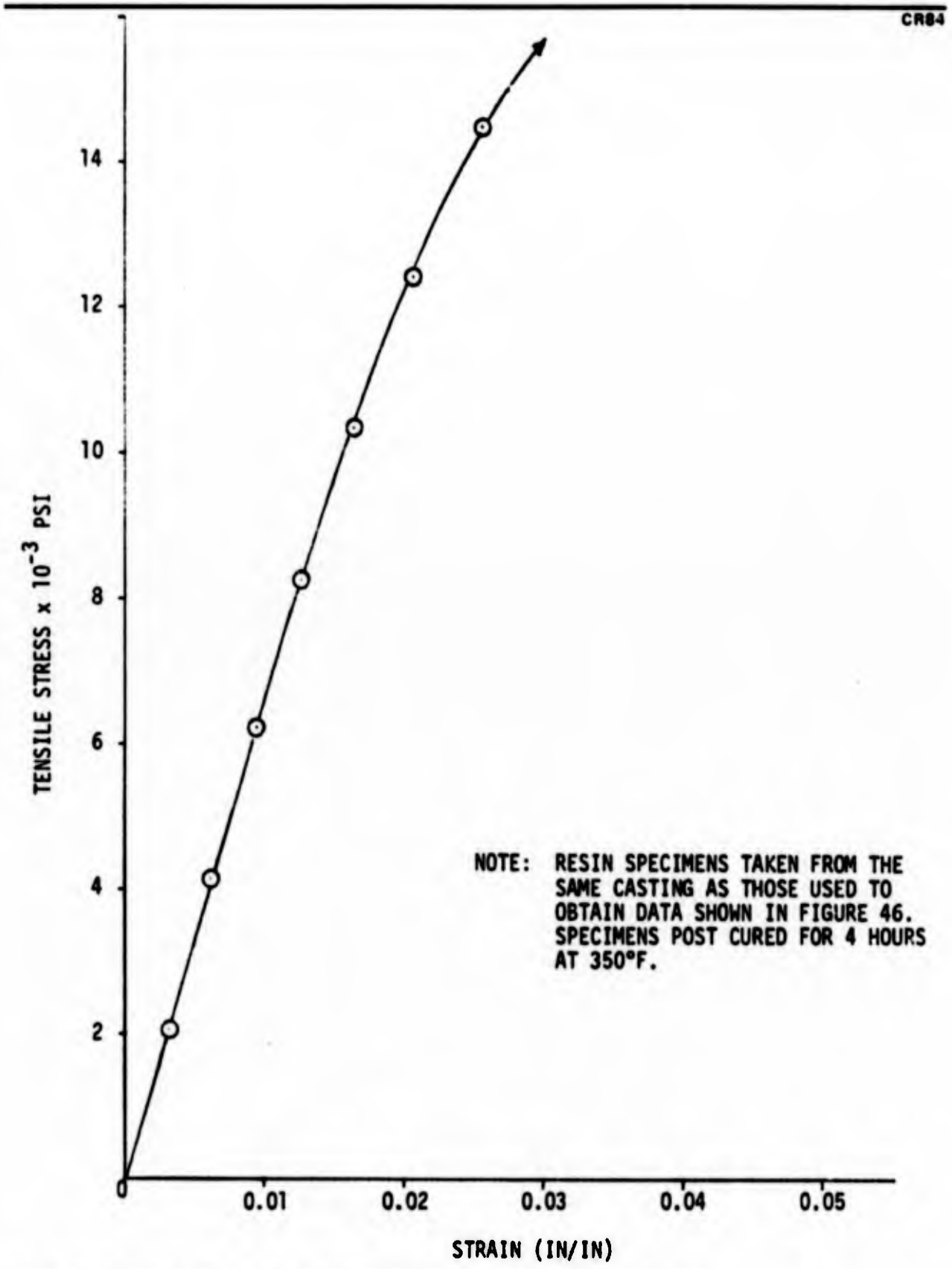

Figure 47. Typical Stress-Strain Curve for Cast and Post-Curved SC1008 Phenolic Resin

TABLE 8

REINFORCING FIBERS AND THEIR PROPERTIES

FIBER TYPE	YOUNG'S MODULUS X 10^{-6} psi		SHEAR MODULUS 10^{-6} psi	POISSON'S RATIO (ν_{fLT})	SPECIFIC GRAVITY
	AXIAL (E_{fL})	TRANSVERSE (E_{fT})			
S-GLASS	12.4	12.4 (1)	5.17 (2)	0.20	2.48
MODMOR II	40.0	1.6 (3)	1.2 (4)	0.20	1.71
BORON	60	60 (1)	22.9 (2)	0.20	2.60

(1) Assumed

(2) Calculated from $G=E/2(1+\nu)$

(3) Estimated from data on crystals given in [11]

(4) The same value used as that given for Thornel 40 [12]

then cured as described later. Composite panels were also made from prepregs purchased from Narmco Whittaker and U.S. Polymeric. These included:

A. Modmor II fibers in 1004 epoxy resin
B. Boron fibers in 1004 epoxy resin
C. S-glass fibers in SC1008 phenolic resin
D. Modmor II graphite fibers in SC1008 phenolic resin.

The boron prepregs contained 104-glass scrim cloth.

To achieve various fiber and void contents, processing parameters were varied. The processing parameters employed in fabricating the various composite panels are presented in Table 9. The nominal size of the various panels was 6 inch by 6 inch by 0.10 inch. After the panels were made, the top and bottom surfaces of each panel were ground to remove any resin-rich areas. Following the surface grinding, three transverse tension and three interlaminar shear specimens were machined from each panel.

6.4 TRANSVERSE TENSILE STRENGTH DATA FOR COMPOSITES

The approximate dimensions of the transverse tension specimens were ≈0.10 inch by 0.75 inch by 4.0 inch. Two transverse tension specimens from each panel were straight-sided, while the third specimen was a dog-bone shape. Transverse tension strength and Young's modulus were measured from the transverse tension specimens. The Young's modulus was measured using a lightweight Instron extensometer.

The transverse tension strength test data for various composites are presented in Tables D-2, D-3, D-4 and D-5 of Appendix D, whereas Tables 10, 11, and 12 show the average values. In addition to performing the transverse tension tests, determinations were made of the specific gravity, fiber content, and void content of all composite specimens. The specific gravity of the various specimens was determined by gravimetric technique and also from the measured dimensions and weights of each specimen. The fiber and resin weight fractions in the various specimens were determined by the following techniques:

Table 9 (page 1 of 2)

PROCESSING VARIABLES IN COMPOSITE PANEL FABRICATION

Type of Composite	Panel Number	Number of Plies of Composite	Number of Plies of Bleeder Cloth	External Pressure During Cure (psi)	Cure Cycle
Glass/Epoxy	2	22	4	50	Vacuum; 4 to 6°/min to 275°F; 0.5 hr at 275°F; apply pressure; raise temp. to 350°F; cure 2 hr.
	3	15	6	50	Same as No. 2.
	4	18	6	Vacuum	Same as No. 2, except for different external pressure.
	5	18	6	Vacuum	Same as No. 4.
	27	6[1]	3	Vacuum	Same as No. 4.
	15	18	6	25	Same as No. 2, except for pressure.
	28	6	3	100	Same as No. 2, except for pressure.
	10	18	6	190	Same as No. 2, except for pressure.
Glass/Phenolic	22	13	4	Vacuum	R.T. to 220°F at 3°/min with vacuum; dwell 1.5 hr at 220°F; raise temp. to 300°F at 3°/min; cure 2 hr at 300°F.
	29	13	4	25	Same as No. 22, except apply 25 psi after 1.5-hr dwell at 220°F, and cure under pressure.
	8	13	6	50	Vacuum; raise temp. to 250°F at max. heat rise; dwell at 250°F for 10 min; bump several times; increase temp. to 350°F; bump once; raise pressure to 50 psi; cure 2 hr.
	20	13	4	100	R.T. to 220°F at 3°/min; apply 100 psi at 220°F; dwell 1 hr; increase temp. to 300°F; cure 2 hr at 300°F and 100 psi.

(1) 0.06-inch roving spacing

Table 9 (page 2 of 2)

Type of Composite	Panel Number	Number of Plies of Composite	Number of Plies of Bleeder Cloth	External Pressure During Cure (psi)	Cure Cycle
Graphite/Epoxy	6	22	6	Vacuum	Same as No. 5
	24	22	6	Vacuum	Vacuum; R. T. to 275°F at 4 to 6°/min; dwell 0.25 hr at 275°F; increase temp. to 350°F; cure 2 hr at 350°F.
	11	22	6	50	Same as No. 2.
	9	22	6	190	Same as No. 2, except for different external pressure.
	30	22	2	25	Same as No. 29.
Graphite/Phenolic	19	22	2	Vacuum	Same as No. 22.
	7	22	6	50	Same as No. 8.
	21	22	2	100	Same as No. 20.
Boron/Epoxy	14	22	6	50	Vacuum; rise temp. to 275°F at maximum heat rise; apply 50 psi; vent bag; increase temp. to 350°F; cure 2 hr.
	13	22	6	190	Same as No. 14, except for different pressure.
	25	20	4	Vacuum	Vacuum; raise temp. to 200°F at 6°/min; dwell 2 hr at 200°F; increase temperature to 300°F; cure at 300°F for 2 hr under vacuum.
	26	20	4	100	Same as No. 25, except apply 100 psi when temperature gets to 200°F; cure under pressure.

Notes: Panels 25 and 26 were made with 5505 resin; Panels 2, 3, 4, 5, 27, 15, 28, 10, 6, 24, 11, 9, 14, and 13 were made with 1004 epoxy resin; Panels 22, 29, 8, 20, 19, 30, 7, and 21 were made with SC1008 phenolic resin.

TABLE 10

AVERAGE PROPERTIES OF GLASS-EPOXY AND GLASS-PHENOLIC COMPOSITES†

SPECIMEN DESIGNATION	RESIN CONTENT (% by wt)	APPARENT FIBER CONTENT, k_f (%)	VOID CONTENT k_{vc} (%)	TRUE FIBER CONTENT $\bar{k}_f$ (%)	TRANSVERSE YOUNG'S MODULUS E_T (10^6 psi)	TRANSVERSE TENSILE STRENGTH σ_T (psi)	INTERLAMINAR SHEAR STRENGTH τ_{LT} (psi)
(1)							
4	18.14	69.6	3.79	66.9	2.61	4,505	10,620
5	29.50	54.7	8.01	50.4	1.72	3,077	9,817
27	23.72	62.0	4.97	59.2	2.22	3,740	12,127
15	33.62	50.0	1.58	49.3	1.68	5,922	13,627
2	34.64	48.9	0.97	48.4	1.65	7,780	11,558
28	21.64	64.0	0.89	63.5	2.66	9,560	14,070
10	29.64	54.6	0.76	54.3	1.89	8,690	14,193
3	23.29	62.5	1.00	61.9	2.40	8,850	14,327
(2)							
22	24.49	60.3	13.1	52.4	1.41	(1,351)*	8,473
29	29.06	54.6	1.63	53.8	1.77	(1,220)*	9,060
8	24.58	60.7	4.6	59.5	--	(402)*	3,443
20	(22.8)**	60.1	(2.5)	58.4	--	--	4,342

† Each data point is an average of 3 tests.

* Specimens were curved; data not valid.

** Obtained from edge of panel.

(1) Specimens made with glass/epoxy.

(2) Specimens made with glass/phenolic.

TABLE 11

AVERAGE PROPERTIES OF GRAPHITE-EPOXY AND GRAPHITE-PHENOLIC COMPOSITES†

SPECIMEN DESIGNATION	RESIN CONTENT (% by wt)	APPARENT FIBER CONTENT, k_f (%)	VOID CONTENT k_{vc} (%)	TRUE FIBER CONTENT $\bar{k}_f$ (%)	TRANSVERSE YOUNG'S MODULUS E_T (10^6 psi)	TRANSVERSE TENSILE STRENGTH σ_T (psi)	INTERLAMINAR SHEAR STRENGTH τ_{LT} (psi)
(1)							
6	38.68	53.7	2.37	52.5	1.016	6,277	11,787
9	34.86	57.8	1.33	57.0	1.009	6,773	13,973
11	35.04	57.6	1.20	56.9	1.007	5,650	12,280
24	37.69	54.8	7.83	50.5	0.933	4,188	7,313
30	35.12	57.6	2.57	56.1	1.133	2,930	10,873
(2)							
19	29.58	62.9	10.50	56.3	1.089	2,520	4,400
7	28.09	64.6	9.30	58.6	1.186	3,507	7,247
21	30.54	61.8	1.27	61.1	1.086	(1,144)*	9,408

* Panel from which the specimen was cut was curved; data not valid

† Each data point is an average of 3 tests.

(1) Specimens made with graphite/epoxy.

(2) Specimens made with graphite/phenolic.

TABLE 12

AVERAGE PROPERTIES OF BORON-EPOXY COMPOSITES*

SPECIMEN DESIGNATION	RESIN CONTENT (% by wt)	APPARENT FIBER CONTENT, k_f (%)	VOID CONTENT k_{vc} (%)	TRUE FIBER CONTENT k_f (%)	TRANSVERSE YOUNG'S MODULUS E_T (10^6 psi)	TRANSVERSE TENSILE STRENGTH σ_T (psi)	INTERLAMINAR SHEAR STRENGTH τ_{LT} (psi)
14 (1)	24.08	60.3	3.60	58.1	2.403	6,672	13,687
13	24.55	59.7	5.00	56.7	3.373	9,528	14,560
25 (2)	26.25	57.4	8.37	52.8	2.270	7,007	13,000
26	24.05	60.2	2.37	58.7	3.377	12,047	16,607

* These composites contained 104 glass scrim cloth.
Each data point is an average of 3 tests.

(1) Specimens made with 1004 Epoxy.

(2) Specimens made with 5505 Epoxy.

A. Using resin burnout for glass epoxy and glass phenolic composites.
B. Using hot nitric acid digestion for graphite epoxy and graphite phenolic composites.
C. Using hot sulphuric acid digestion for boron epoxy composites.

The composite samples used in resin and fiber content determinations came from transverse tension specimens after the latter were tested. To ensure that the acids did not attack either the graphite fibers or the boron fibers, uncoated graphite and boron fibers were placed in beakers of acid and exposed to the same environment as the composite test specimens on which the acid digestion tests were being performed. No appreciable weight loss due to exposure of fibers to acid was found in either type of fiber. The fiber weight loss was less than 0.5 percent.

Following the determination of the specific gravity of composites, and the weight fractions of fibers and resin in each composite, the apparent and true fiber volume fractions and void contents were determined from the following equations.

Apparent fiber volume fraction k_f

$$k_f = \frac{1}{1 + \frac{w_r}{w_f}\frac{\rho_f}{\rho_r}} \tag{43}$$

Void content k_{vc}

$$k_{vc} = 1 - \frac{\rho_m}{\frac{\rho_f - \rho_r}{1 + \frac{w_r}{w_f}\frac{\rho_f}{\rho_r}} + \rho_r} \tag{44}$$

True fiber volume fraction, $\bar{k}_f$,

$$\bar{k}_f = \left(1 - k_{vc}\right) k_f \tag{45}$$

where

w_r = weight fraction of resin

w_f = weight fraction of fibers

ρ_r = density of resin

ρ_f = density of fibers

ρ_m = measured density of composite

The results for k_f, $\bar{k}_f$, and k_{vc} are also presented in Tables D-2, D-3, D-4, and D-5 of Appendix D, as well as Tables 10, 11, and 12 in this section.

6.5 INTERLAMINAR SHEAR STRENGTH DATA FOR COMPOSITES

The approximate dimensions of the interlaminar shear specimens were 0.10 inch by 0.375 inch by 1.0 inch. The span-to-thickness ratio for interlaminar shear specimens was kept 4:1. Only the interlaminar shear strength was measured from these tests. Quarter-inch diameter pins were used for supports and for applying the load. Several of the specimens were also tested using an 0.125-inch-diameter loading pin. No trend was found as a result of using different size pins. The interlaminar shear strength data are also shown in Tables D-2, D-3, D-4, and D-5 of Appendix D, as well as in Tables 10, 11, and 12 in this section. The latter three tables show the average test results.

Section 7

COMPARISON OF MEASURED TRANSVERSE TENSILE AND INTERLAMINAR SHEAR STRENGTH WITH MICRO-MECHANICS FAILURE THEORY PREDICTIONS

To establish the validity of the micromechanics failure criteria for transverse and shear strength of composites, the test data presented in Section 6 was compared with the theoretical predictions based on equations of Section 5.

7.1 TEST-THEORY COMPARISON OF THE TRANSVERSE TENSILE STRENGTH OF COMPOSITES

Inasmuch as the transverse strength of composites is a function of the volume fraction of ineffective fibers, $\bar{k}_{if}$, (see Equations 29 to 36) the volume fraction of such fibers had to be estimated before test-theory comparison of the transverse strength could be made. This was done by plotting the theoretical and experimental results for the transverse Young's modulus of the composites, and postulating that any difference between the two sets of results in due to voids and ineffective fibers Reference 14. Figures 48 and 49 show such plots for composites made with glass and graphite fibers. Moreover, examples are shown there on how the apparent volume fractions of ineffective fibers were estimated. By plotting E_T versus k_f rather than $\bar{k}_f$, the influence of porosity on E_T was subtracted. Therefore, in accordance with the above hypothesis, the difference between k_f, corresponding to the theoretical value of E_T, and k_f corresponding to the experimental value of E_T is the apparent volume fraction of the ineffective fibers, k_{if}. For any given data point, the true volume fraction of ineffective fibers, $\bar{k}_{if}$, is equal to

$$\bar{k}_{if} = \left(1-k_{vc}\right) k_{if} \tag{47}$$

where k_{vc} is the void content of a given specimen, from which the experimental E_T was measured. The estimated ineffective fiber volume fractions for the specimens made with glass and graphite fibers, as well as other pertinent data,

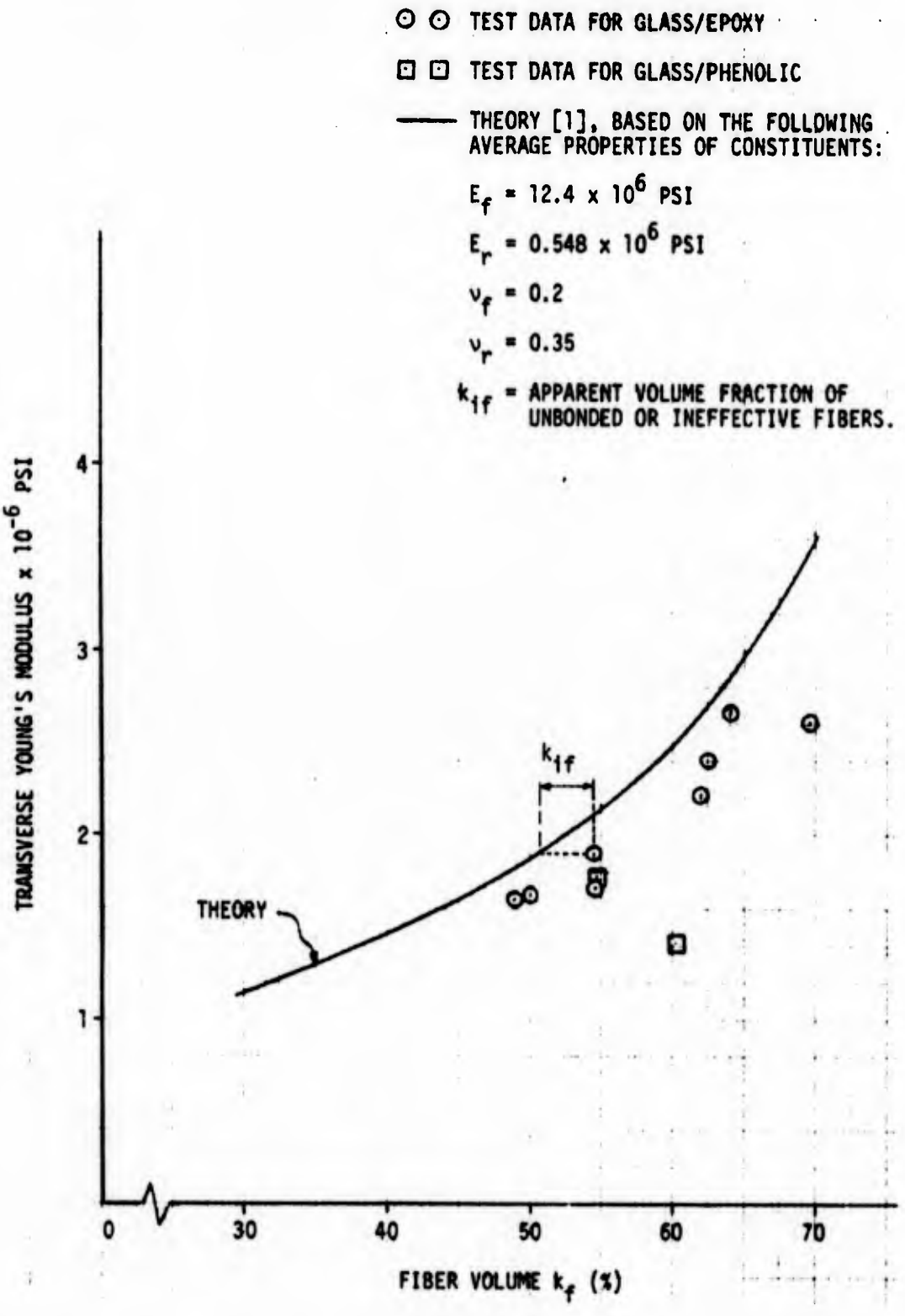

Figure 48. Test-Theory Comparison of Transverse Young's Modulus of Composites Made with S-Glass Fibers

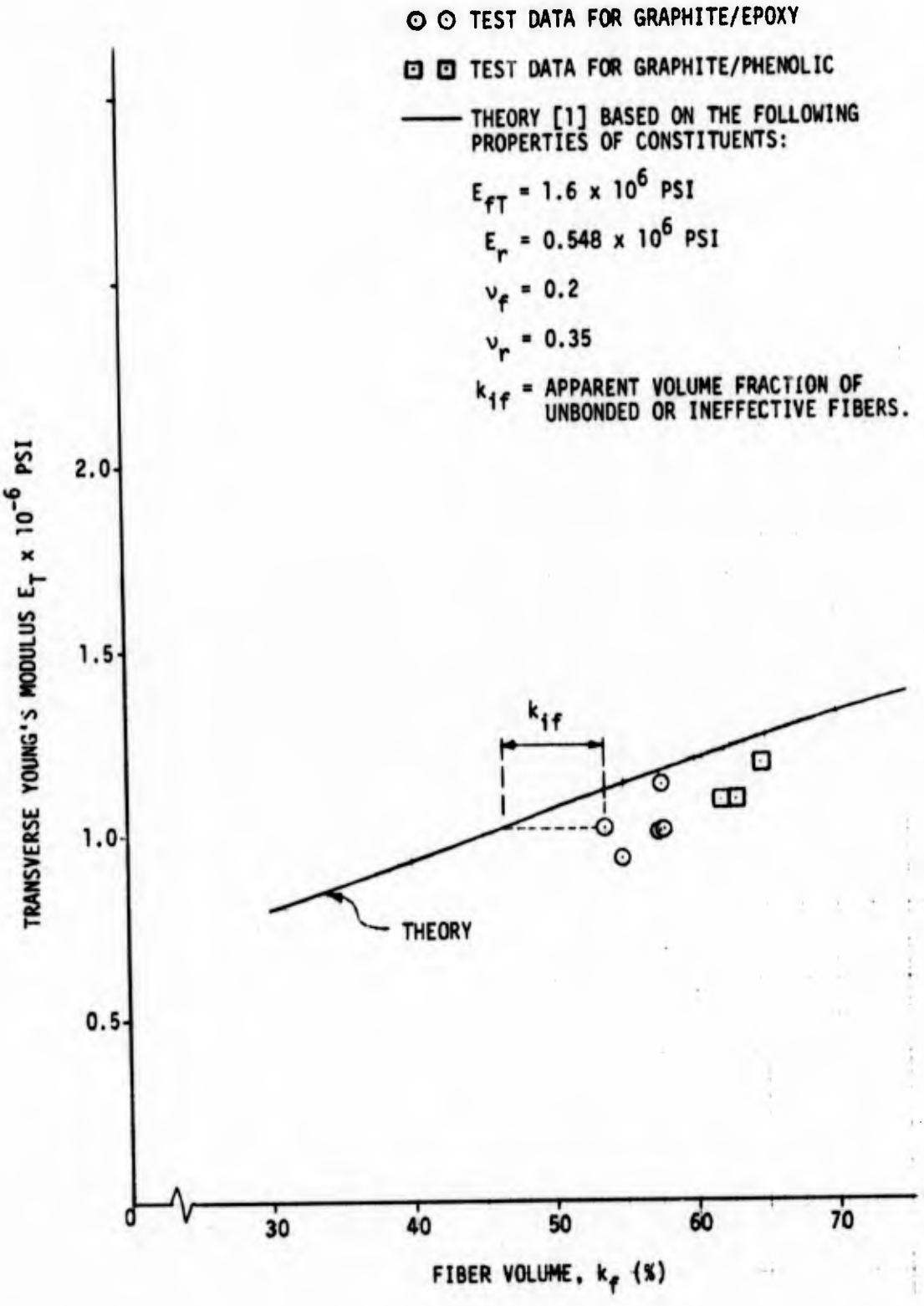

Figure 49. Test-Theory Comparison of Transverse Young's Modulus of Composites Made with Graphite Fibers

are presented in Table 13. Using the data given in Table 13 and the equations of Section 5, theoretical predictions were made of the transverse tensile strength of the composites. Figures 50 and 51 show the test-theory comparison, as well as the constituent properties and other data that were used to obtain the theoretical curves. The failure theory described in Section 5 is based on the assumption that the fibers are isotropic, therefore the determination of predicted strength of composites made with glass fibers was straightforward, since such fibers are generally assumed to be isotropic. The above assumption does not, however, apply to composites made with graphite fibers, inasmuch these fibers are strongly orthotropic, as shown in the previous section. The influence of fiber orthotropy was accounted for approximately by assuming that the internal stresses in the matrix of the composite are governed by E_{fT} in directions x and y, and by E_{fL} in direction z, that is

$$K_x^*, K_y^* = f\left(E_{fT}, \ldots\ldots\ldots\right)$$

$$K_z^* = f\left(E_{fL}, \ldots\ldots\ldots\right)$$

Except for the above modification, the theoretical curve shown in Figure 51 was determined in the same way as the curve shown in Figure 50. Each test point shown in Figures 50 and 51 is an average of three tests (see Tables 10, 11, and 12 and Tables D-2, D-3, and D-4 of Appendix D).

Except for one test point in Figure 51, the test-theory correlation is fairly good. The fact that some of the test data are higher than the theoretically predicted values could be attributed to:

A. Experimental errors.
B. Errors in the void, resin, and fiber content determinations.
C. The properties of the in situ resin in composites may be different than those measured from resin castings
D. Assumptions made in the theory formulation. Residual stresses, void shape, size, and distribution, fiber array and fiber-matrix interface may influence σ_T^*.
E. Processing parameters that were employed may influence matrix properties and thereby σ_T^*.

The correlation of measured and predicted strength properties using data corresponding to each specimen is also expected to yield improvements in test-theory agreement. As noted in Figures 50 and 51, the theoretical curves shown in these figures are based on average $\bar{k}_f$ corresponding to all composites for which data are shown therein. Items A through E, and other items involving theory refinement will be investigated in the future.

Further test-theory comparison of the transverse tensile strength of composites is presented in Figure 52. The test data shown there are from Figure 50 and from the literature (References 14 and 15). The composites for which test data was found were made from different resins than those used in the present program, therefore the transverse tensile strength of composites, σ^*_T, was normalized with respect to tensile strength of various resins.

No test-theory comparison is presented herein for the transverse tensile strength of boron epoxy composites. The reason for this is that the failure theory applies to composites containing fibers, matrix, voids, and ineffective fibers, whereas the boron composites contained 104-glass scrim cloth in addition to the above variables. Therefore, the theory as presented in Section 6 is not applicable to such composites. The failure theory can, however, be extended to such composites if the influence of scrim cloth on internal stresses due to fibers, voids, and ineffective fibers is established. No attempt was made to do this in the present program.

7.2 TEST-THEORY COMPARISON OF THE INTERLAMINAR SHEAR STRENGTH OF COMPOSITES

The test-theory comparison of the interlaminar shear strength of composites made with S-glass fibers and graphite fibers and two different resin systems is shown in Figures 53 and 54. The test data from Section 6 is compared therein with the theoretical results predicted by Equation 41. In calculating the theoretical results shown there, it was assumed that the fiber contents, void contents, and the volume fractions of ineffective fibers in the interlaminar shear specimens were the same as in the transverse tension specimens

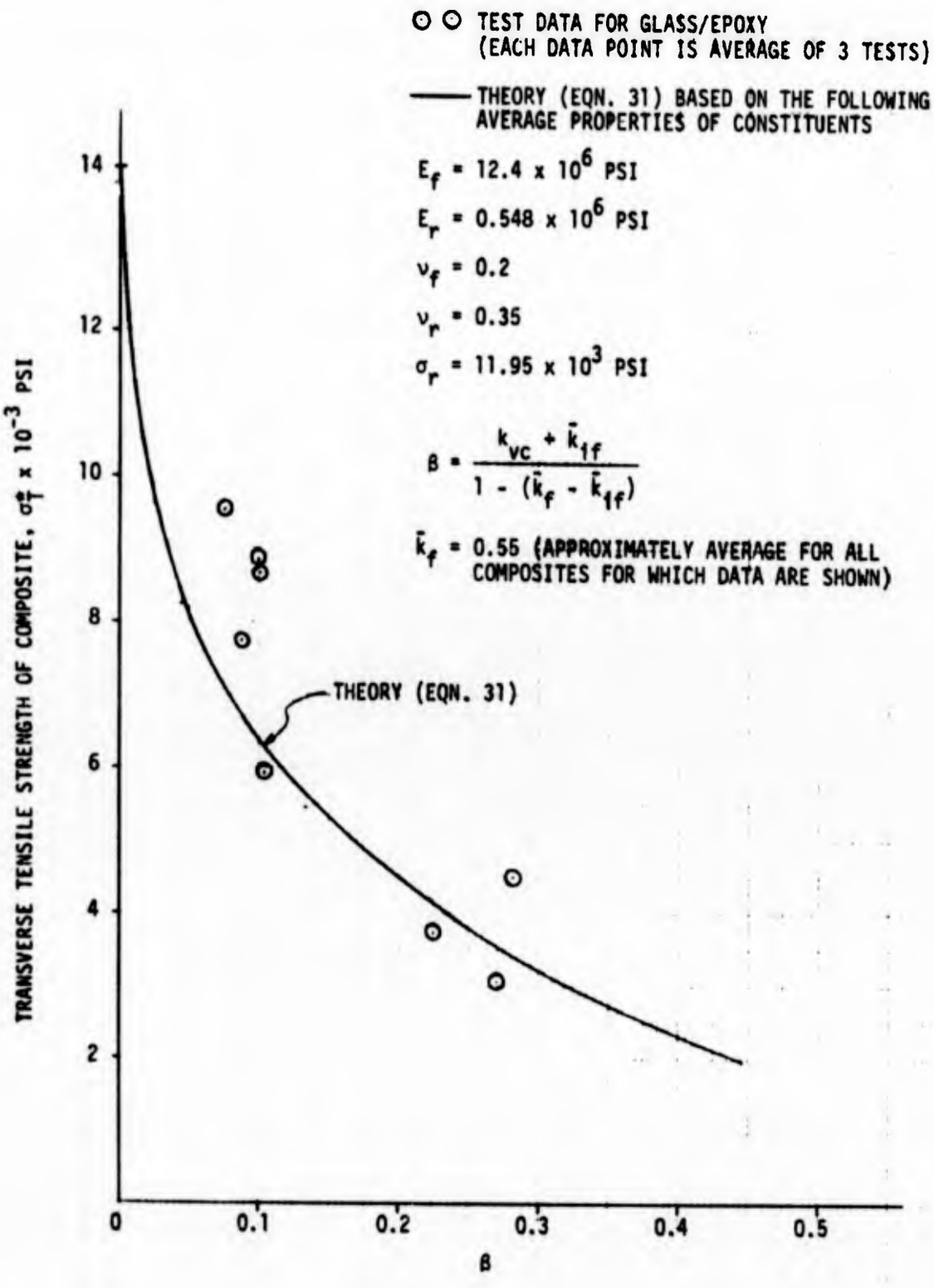

Figure 50. Test-Theory Comparison of the Transverse Tensile Strength of Composites Made with Glass Fibers

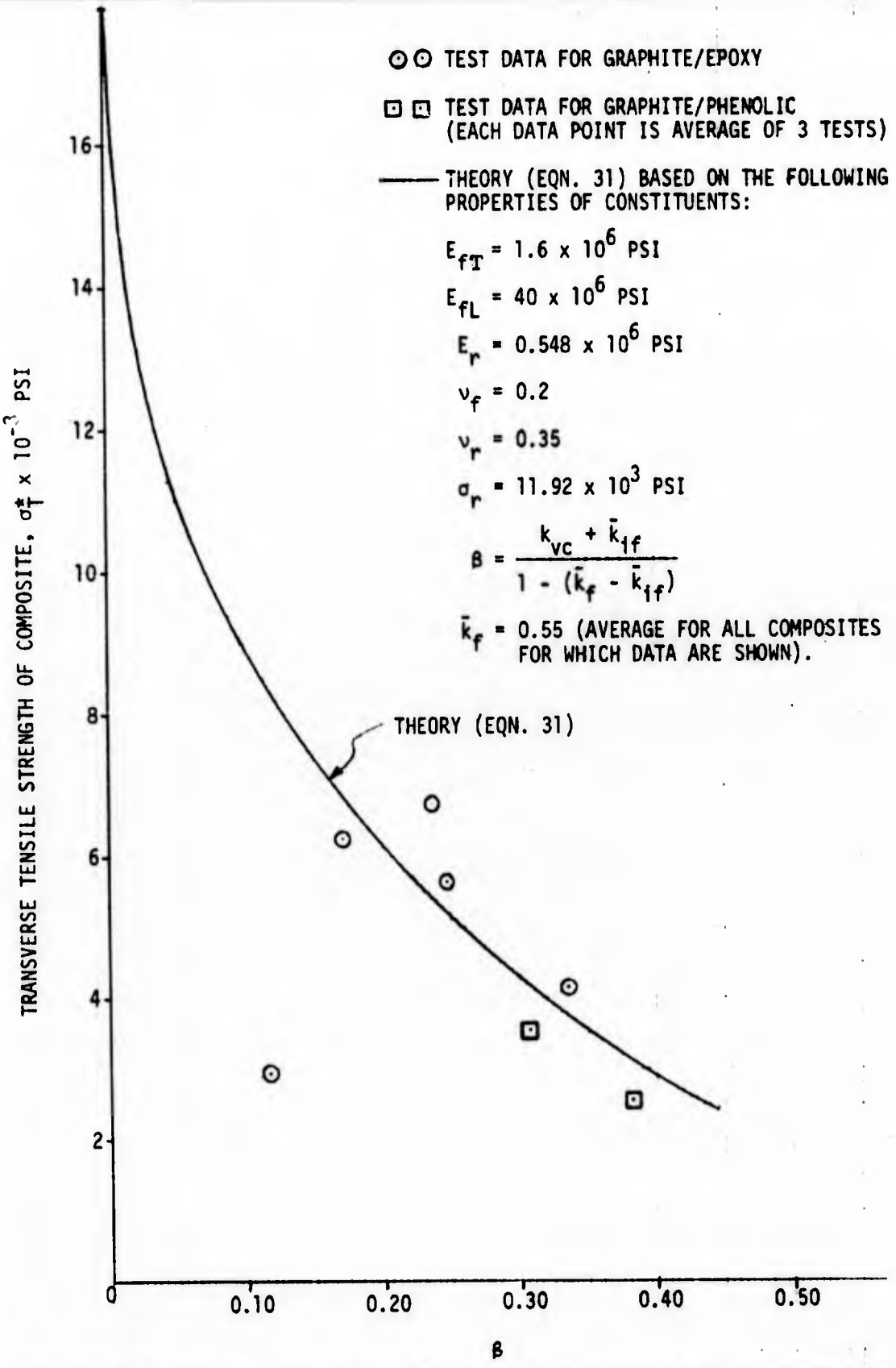

Figure 51. Test-Theory Comparison of Transverse Tensile Strength of Composites Made with Graphite Fibers

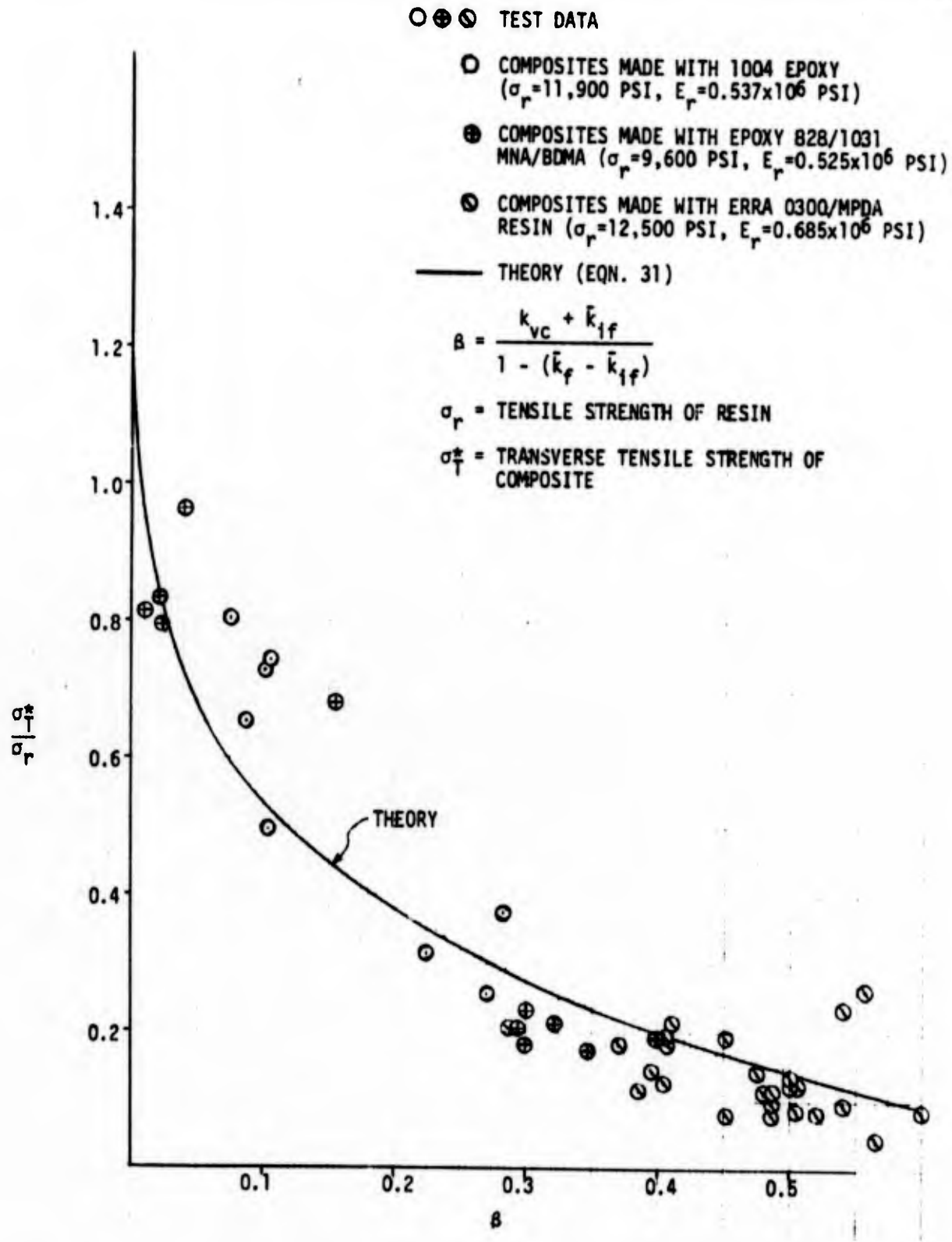

Figure 52. Test-Theory Comparison of the Transverse Tensile Strength of Composites Made with S-Glass Fibers and Different Resins

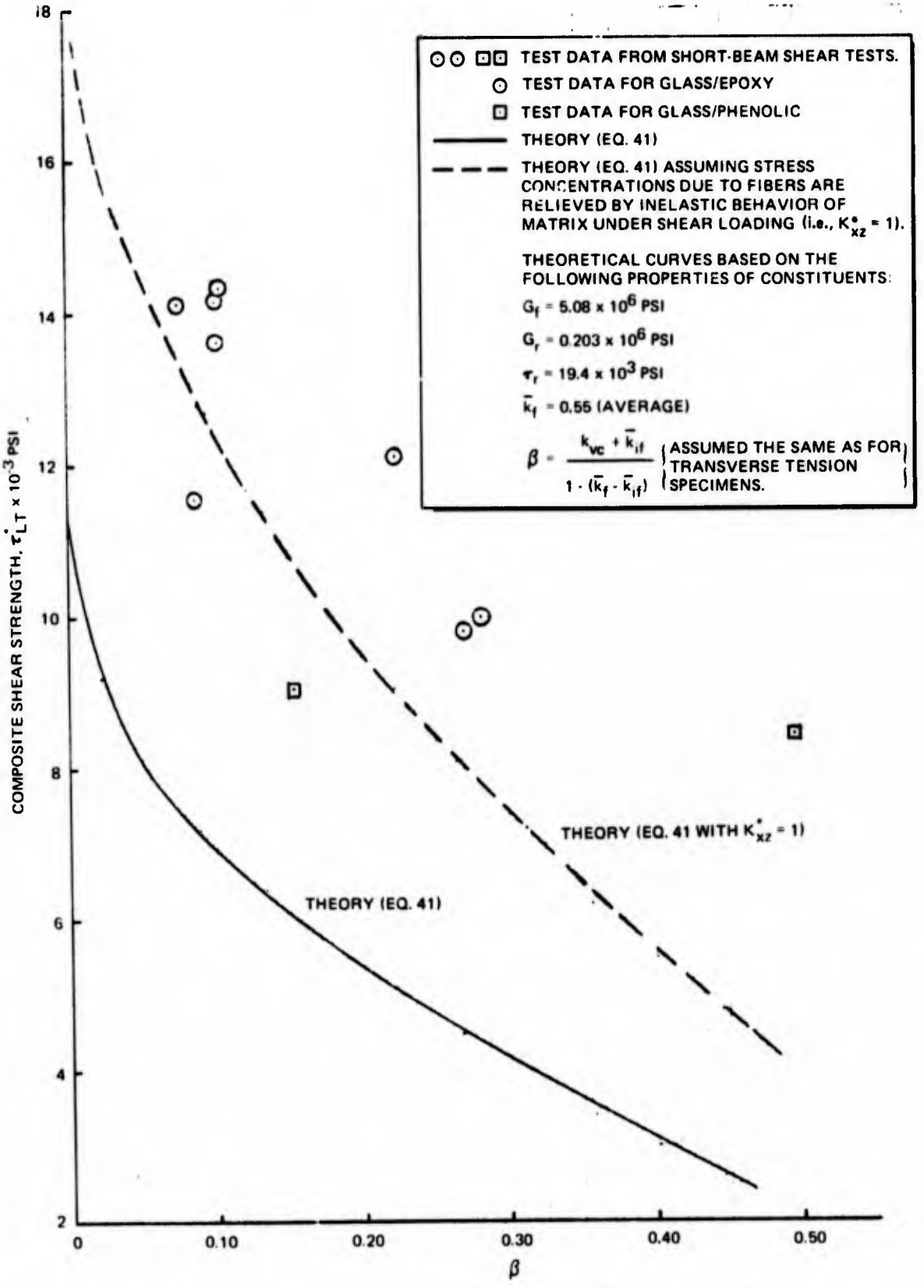

Figure 53. Test – Theory Comparison of Shear Strength of Composites Made with Glass Fibers

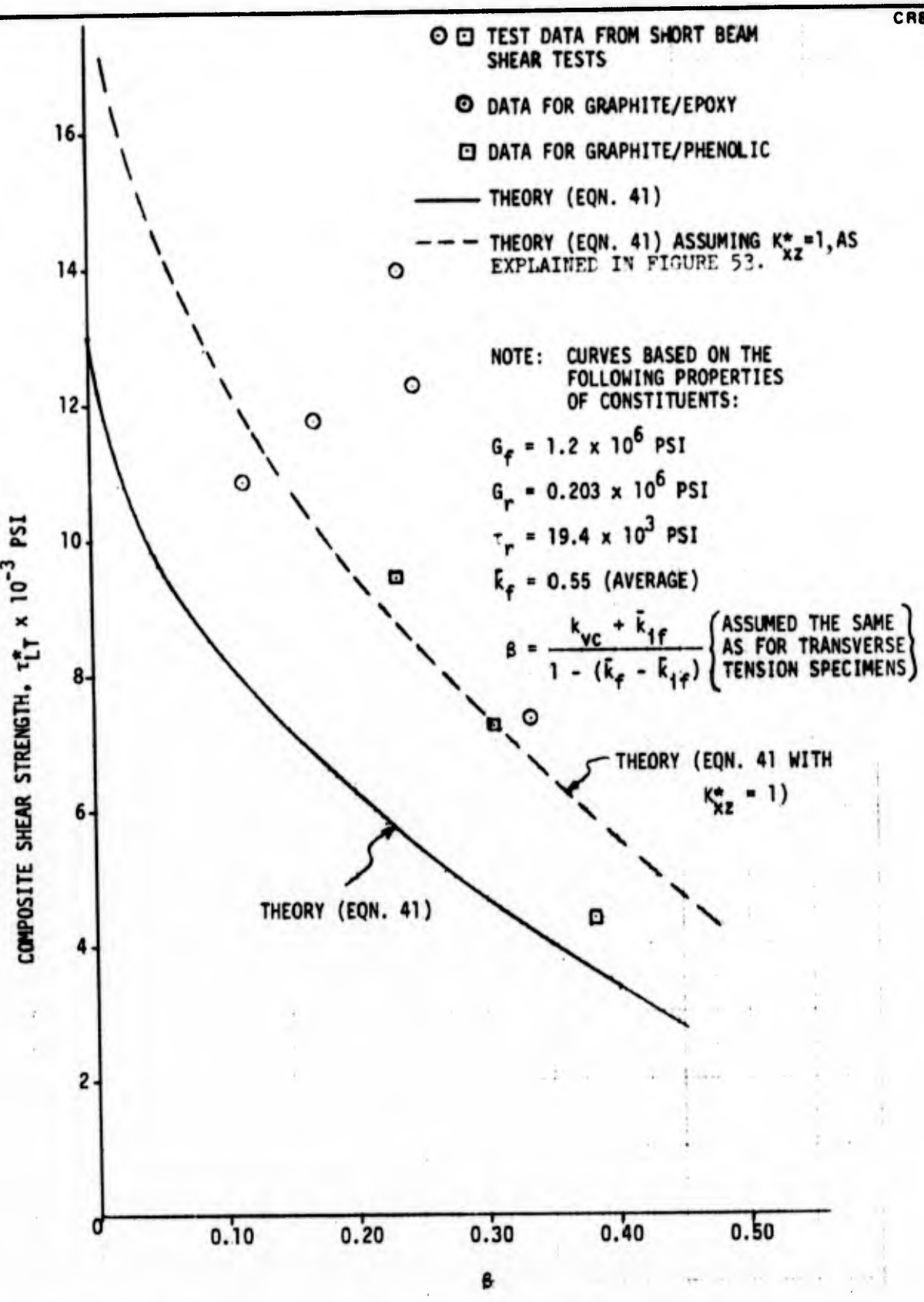

Figure 54. Test-Theory Comparison of Shear Strength of Composites Made with Graphite Fibers

(see Table 13). Moreover, since the shear strength of the resins was not measured experimentally, the latter was estimated from the following equation

$$\tau_r \approx \frac{\sqrt{2}\ \sigma_{tr}\ \sigma_{cr}}{\left[\left(\sigma_{tr}\right)^2 + \left(\sigma_{cr}\right)^2 - \left(\sigma_{tr}\right)\left(\sigma_{cr}\right)\right]^{1/2}} \qquad (48)$$

where τ_r is the shear strength of the resin, σ_{tr} is the tensile strenght of the resin, and σ_{cr} is the compressive strength of the resin. Equation 48 was derived by resolving the shear stress acting on an element of resin into tensile and compressive stresses, and applying a Norris-type failure criterion (Reference 9) to predict failure (Reference 16). In doing this, the difference between tensile and compressive strength of resins was taken into account. The compressive strength of most resins is ~30 ksi, while the tensile strength of the resins investigated in this program was ≈12 ksi; therefore, with these values Equation 48 gives*

$$\tau_r \approx 19.4 \text{ ksi}$$

The latter value is in general agreement with results reported in Reference 17. From the results shown in Figures 53 and 54 it is apparent that the shear strength of the composites predicted by Equation 41 (solid curves) gives values significantly lower than those of the test data. Several factors could be responsible for this, mainly:

A. Inelastic deformations of resins under shear loading.

B. The fact that volume fractions of ineffective fibers in the short beam shear specimens may be lower than those found in the transverse tension specimens because the maximum shear stress acts over a much shorter gage length.

C. Non-applicability of the short beam shear test to determination of the shear strength of composites.

*See the end of this section for further discussion on the validity of Equation 48.

TABLE 13

INEFFECTIVE FIBER CONTENTS FOR COMPOSITES MADE WITH GLASS AND GRAPHITE FIBERS

SPECIMEN DESIGNATION	REINFORCING FIBER	RESIN	VOID CONTENT k_{vc} (%)	APPARENT FIBER VOLUME k_f (%)	TRUE FIBER VOLUME $\bar{k}_f$ (%)	ESTIMATED TRUE VOLUME OF INEFFECTIVE FIBERS $\bar{k}_{if}$ (%)
4	S-Glass	1004 Epoxy	3.79	69.6	66.9	7.70
5			8.01	54.7	50.4	7.45
27			4.97	62.0	59.2	5.42
15			1.58	50.0	49.3	4.13
2			0.97	48.9	48.4	3.86
28			0.89	64.0	63.5	1.98
10			0.76	54.6	54.3	4.26
3			1.0	62.5	61.9	3.46
22	S-Glass	SC1008 Phenolic	13.1	60.3	52.4	18.96
29			1.63	54.6	53.8	6.5
8			4.6	60.7	59.5	---
20			2.5	~60	58.4	---
6	Graphite	1004 Epoxy	2.37	53.7	52.5	7.02
9			1.33	57.8	57.0	11.64
11			1.20	57.6	56.9	12.64
24			7.83	54.8	50.5	13.19
30			2.57	57.6	56.1	2.92
19	Graphite	SC1008 Phenolic	10.5	62.9	56.3	10.0
7			9.3	64.6	58.6	4.9
21			1.27	61.8	61.1	10.2

D. Experimental errors. For example, the fiber, resin, and void contents in the short beam shear specimens may have been different than the values given in Table 13, which were used to obtain the theoretical curves.

Because resins generally exhibit inelastic behavior under shear loading, one would expect relief of stress concentrations due to fibers. The dashed curves shown in Figures 53 and 54 were calculated on this basis, that is assuming that $K^{*}_{xz} \rightarrow 1$ due to inelastic deformation of resin under shear loading. By making this assumption, a better correlation is obtained between test and theory.

Inasmuch as the gage length in the short-beam shear test is much smaller than the gage length in the transverse tension test, it is reasonable to expect that the ineffective fibers would not influence the short-beam shear strength as significantly, if at all, as they would the transverse tension strength. By assuming no influence of $\bar{k}_{if}$ on τ^{*}_{LT}, the results shown in Figure 55 were obtained. In calculating the dashed curve shown therein it was also assumed that the matrix undergoes inelastic deformations under shear loading, that is $K^{*}_{xz} \rightarrow 1$. The final equation for the shear strength of composites resulting from application of the above-stated assumptions to Equation 41 becomes

$$\tau^{*}_{LT} = \left[1 - \frac{4}{\pi}\left(\frac{k_{vc}}{1-\bar{k}_{f}}\right)\right]^{1/2} \tau_{r} \qquad (49)$$

As to item (C) given above, it has been shown in Reference 18 and other references that the shear strength obtained from the short-beam shear tests is generally higher than the shear strength obtained from the pure torsion tests. A simple explanation for this (Reference 16) seems to be that in the short-beam shear test the material located in the failure area is not under pure shear loading, as is assumed, but rather under combined loading (shear and compression), as shown in Figure 56. The compression component of the load comes from the load P applied to the beam. The compression stress

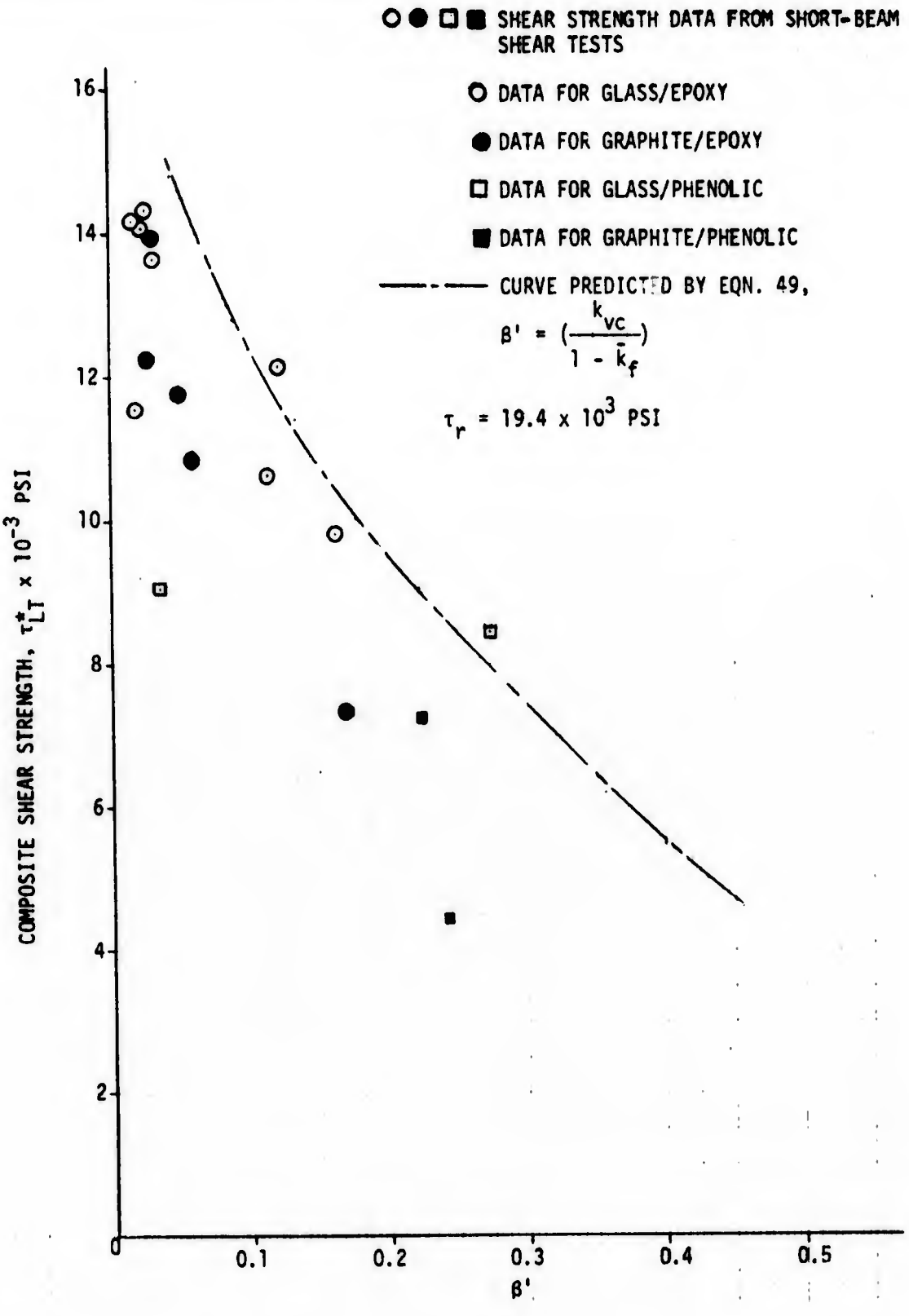

Figure 55. Test-Theory Comparison of Shear Strength of Glass- and Graphite-Fiber-Reinforced Composites

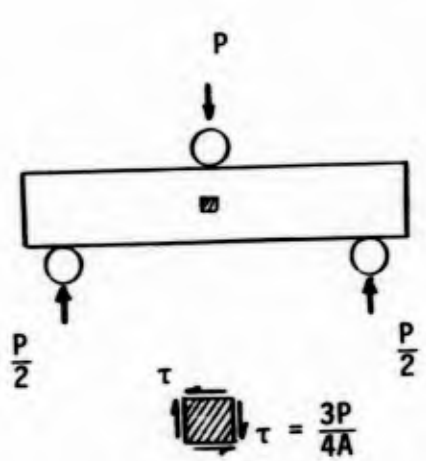

ASSUMED STRESSES
ACTING ON AN
ELEMENT OF MATERIAL

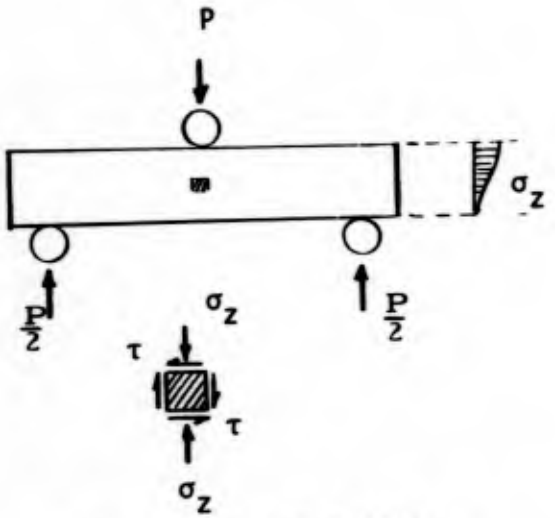

ACTUAL STRESSES ACTING
ON AN ELEMENT OF MATERIAL

Figure 56. Assumed and Actual Stresses Acting on the Failure Plane in the Short-Beam Shear Test

varies from a maximum at the point on the top surface of the beam, where the load is applied to zero at the bottom surface of the beam. The influence of combined loading on the apparent shear strength is shown in Figure 57 (Reference 16). It is seen there that under certain conditions the apparent shear strength obtained from the short-beam shear test can be almost twice as high as the true shear strength of the material.

Although no torsion tests were performed on composites, shear strength data obtained from such tests on graphite epoxy composites was found in the literature (Reference 19). Figure 58 shows the comparison of these results with the theoretically predicted shear strength.

The composites for which shear strength data are shown in Figure 58 were made of Thornel 40 graphite fibers and 828/1031 MNA/BDMA resin. The shear strength of these composites was obtained from torsion tests on solid rods. Although no void contents were given for individual specimens, it is shown in Reference 17 that the void contents varied from ≈0 percent to ≈4 percent. Consequently the predicted curve shown in Figure 58 was based on an average void content of 2 percent. Since sufficient data were not given in Reference 17 for estimating $\bar{k}_{if}$, the $\bar{k}_{if}$ was estimated from the data given in Table 13. The average void and ineffective fiber contents for graphite epoxy composites shown in Table 13 were k_{vc}=3.06 percent and $\bar{k}_{if}$=9.5 percent. From the above data the $\bar{k}_{if}$ corresponding to k_{vc}=2 percent was estimated to be 6.2 percent.

The elastic and mechanical properties of the 828/1031 epoxy resin were found in References 15 and 17, and are shown in Table 14. Neither reference gives a complete set of mechanical properties data. However, the combined data from the two references was found to be sufficient for estimating τ^{*}_{LT}. It is of interest to compare here the measured shear strength of the resin with the resin shear strength estimated by Equation 48. Substitution of σ_{tr}=9.6 ksi, σ_{cr}=58.5 ksi in Equation 48 gives

$$\tau_r = 14.6 \text{ ksi}$$

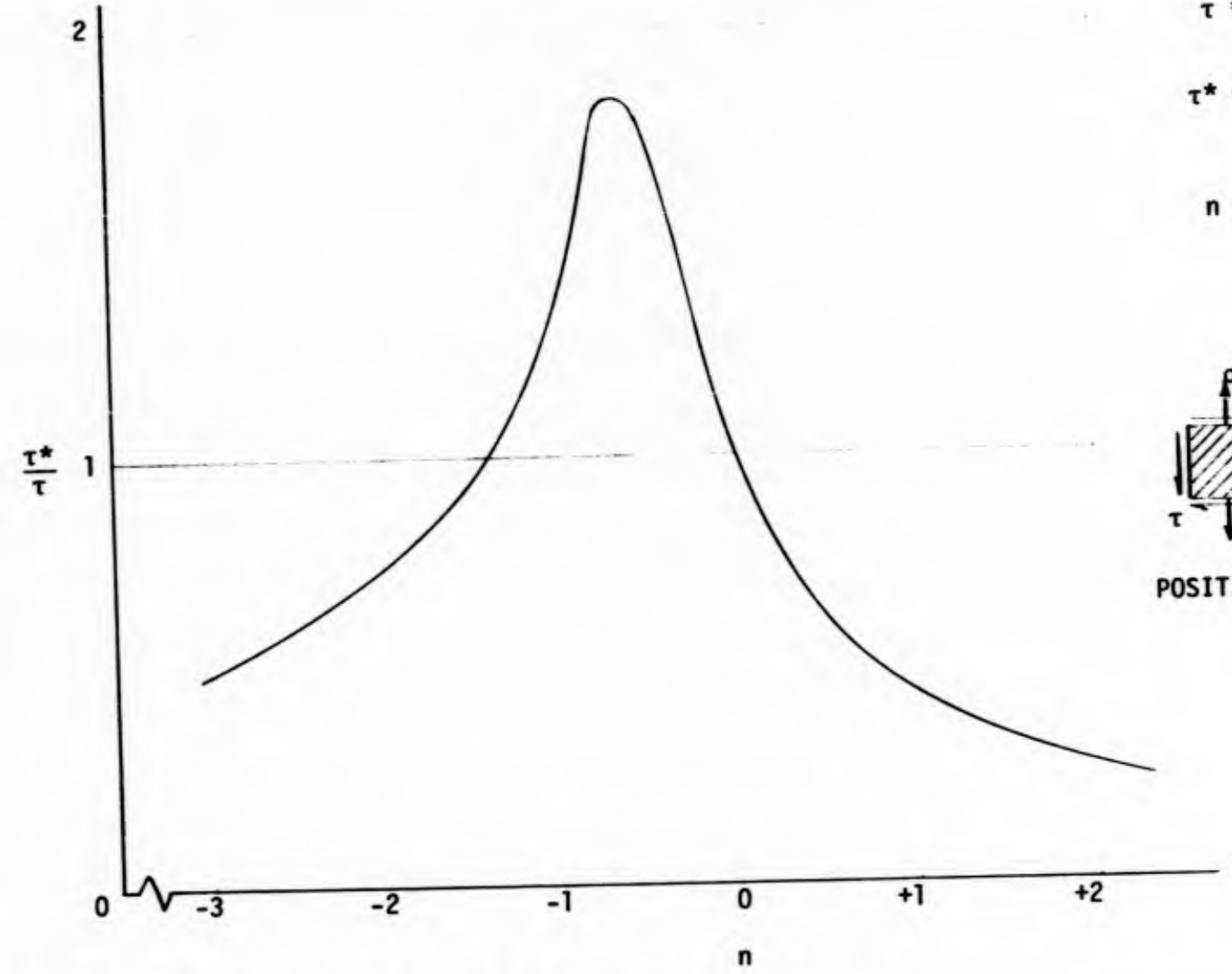

τ = TRUE SHEAR STRENGTH OF MATERIAL

τ* = APPARENT SHEAR STRENGTH OF MATERIAL UNDER COMBINED LOADING

n = σ/τ

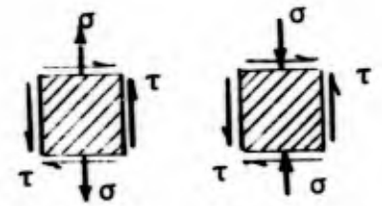

POSITIVE n NEGATIVE n

Figure 57. Influence of Combined Loading on Shear Strength

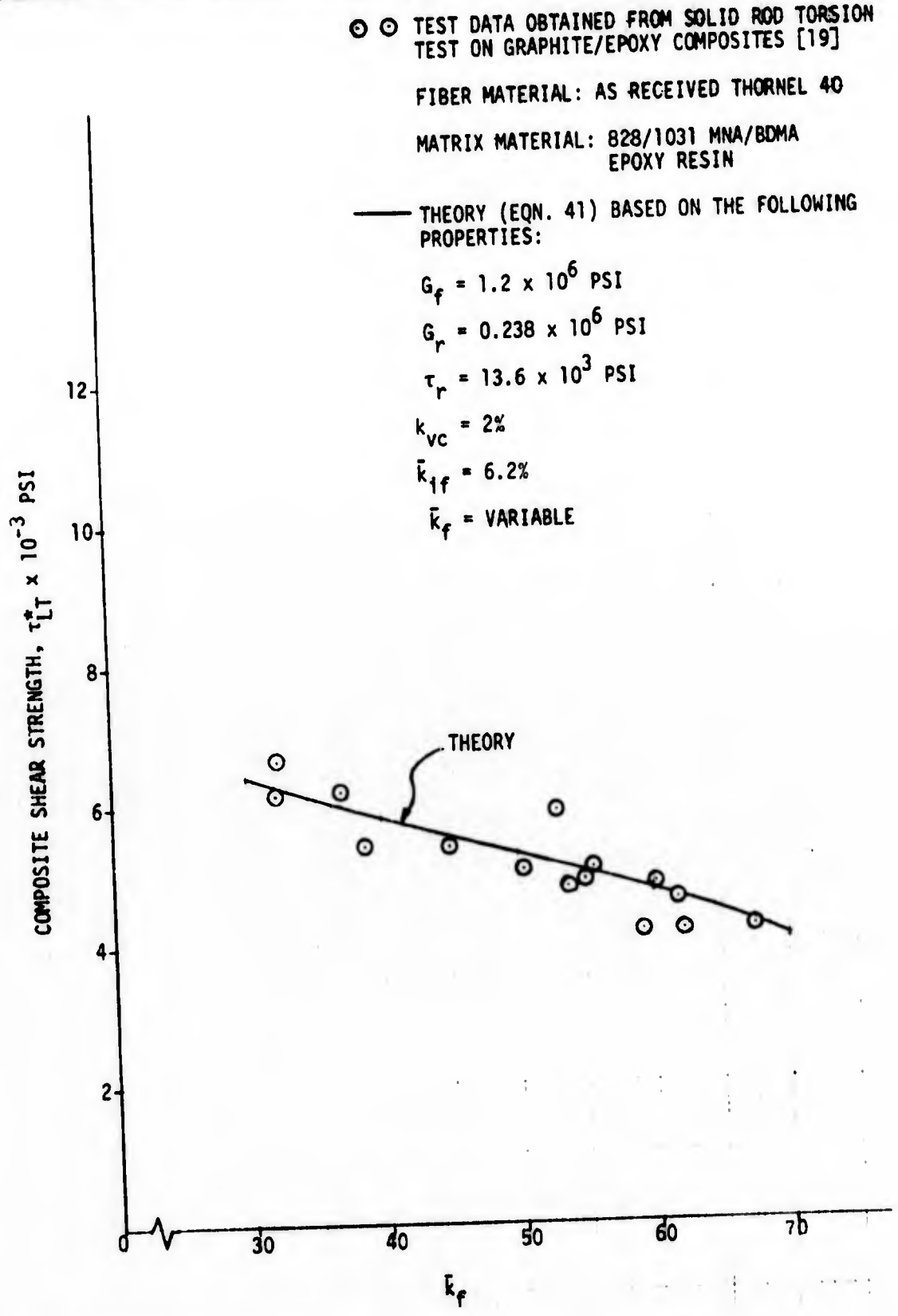

Figure 58. Comparison of Predicted Shear Strength with Test Data Obtained from Solid-Rod Torsion Test

TABLE 14

PROPERTIES OF SHELL EPON 828/1031 MNA/BDMA EPOXY RESIN

PROPERTY / REFERENCE	SHEAR MODULUS $G_r x10^{-6}$ psi	YOUNG'S MODULUS $E_r x10^{-6}$ psi (1)	POISSON'S RATIO ν_r (1)	TENSILE STRENGTH $\sigma_{tr} x10^{-3}$ psi	COMPRESSIVE YIELD STRENGTH $\sigma_{yr} x10^{-3}$ psi	COMPRESSIVE ULTIMATE STRENGTH $\sigma_{cr} x10^{-3}$ psi	SHEAR STRENGTH $\tau_r x10^{-3}$ psi
[15]	0.265	0.525	-----	9.6	20.75	58.5	13.6
[17]	0.212	0.547	0.334	---	-----	----	----
Average	0.238	0.536	0.334	9.6	20.75	58.5	13.6

(1) In tension.

whereas if σ_{cr} is taken as equal to the yield stress ($\sigma_{cr}=\sigma_{yr}=20.75$ ksi) then Equation 48 gives

$$\tau_r = 15.7 \text{ ksi}$$

as compared to the measured shear strength of the resin

$$\tau_r = 13.6 \text{ ksi.}$$

From the above results, it can be concluded that Equation 48 gives a reasonable estimate for the shear strength of resin.

The test-theory correlation shown in Figure 58 is quite good as compared to that shown in Figures 53 or 54. The improved correlation further fortifies the argument regarding the non-applicability of the short-beam shear test to determination of the true shear strength of composites.

Future studies of the items discussed above are planned to refine the failure criterion for composites subjected to shear loading.

Section 8
CONCLUSIONS AND RECOMMENDATIONS

Based on the work performed to date, the following conclusions and recommendations are made:

- The micromechanics failure criterion for transverse tensile strength of composites was found to show fair correlation with test data from actual composites. Further theory refinement appears to be desirable. Specific items which need further investigation are: verification of secondary assumptions made in the failure theory formulation; influence of void size, shape, and distribution; inelastic matrix effects; and influence of residual stresses.
- The micromechanics failure criterion for shear strength of composites was found to show fair correlation with test data (given in literature) obtained from solid-rod torsion tests. The test-theory correlations using the data from short-beam shear tests were found to be poor, although the predicted shear strengths were conservative. Torsional testing of composites and of the matrix materials is required before the validity of the theory can be assessed. The influence of items discussed in Item A on the shear strength of composites needs additional investigation.
- The transverse tensile and shear strengths of composites were found to be influenced by the fiber properties, matrix properties, fiber content, void content, and volume fraction of ineffective fibers. To apply the failure theories to composites made with anisotropic graphite fibers, estimates had to be made of the anisotropic properties of such fibers and of the internal stresses in composites made with such fibers. Attempts should be made to measure these properties. Moreover, the failure criteria presented in this report should be extended to account for the influence of fiber anisotropy on the transverse tensile and shear strengths of composites.
- Experimental studies employing model composites were found to be an invaluable tool in verifying the various steps leading to the formulation of a micromechanics theory for the transverse tensile strength of composites. Similar types of experiments would be desirable for verifying the various steps employed in the formulation

of micromechanics failure criteria for the shear strength of composites.

- Approximate theory for tensile strength of ductile and brittle materials containing voids was found to show good correlation with test data. The influence of matrix ductility on shear strength needs to be determined experimentally.
- For composites containing low void contents (k_{vc} < 5 percent), matrix ductility was found to have a significant influence on the transverse tensile strength of composites (Figure 42). For such composites (low k_{vc}) the matrix ductility was found to have a more significant influence on the transverse strength of composites than did the parameters of the third item of this section.
- Interaction of stress concentration from fibers and voids was found to be one of the key parameters influencing the transverse tensile and shear strength of composites. Consideration of stress concentrations due to fibers alone or voids alone was found inadequate in predicting the strength of composites.
- Use of strain gages on resin tensile specimens was found to reduce their tensile strengths as much as 52 percent as compared to the tensile strengths of resins without any strain gages.

Some preliminary conclusions as to how the constituent properties influence the transverse tensile and shear strength of composites, and recommendations for improving these properties are as follows:

- For void-free composites the transverse tensile strength, σ^*_T decreases with increasing E_f/E_r ratio and with increasing k_f. The transverse tensile strength can be increased by decreasing k_f, increasing σ_r or increasing E_r (from Equation 38).
- Both the transverse tensile strength, σ^*_T, and the shear strength, τ^*_{LT}, decrease with increasing void content k_{vc}. The void content k_{vc} can be reduced by using appropriate processing techniques (see Table 9 for example). Reducing k_{vc} by using high pressure during processing is not considered the best approach since by increasing the pressure, the fiber content, k_f, increases, which in turn decreases σ^*_T and τ^*_{LT} (see the previous item and Figures 44 and 58). Perhaps the prepregs should have higher resin contents,

than they have now, to avoid high k_f's. Once composites with low void-contents, say $k_{vc} \leq 1$ percent, have been achieved, further increases in σ_T^* and τ_{LT}^* can be obtained by using resins exhibiting ductility under tensile loading. Increased matrix ductility can be achieved through using new resin formulations or by modifying the cure cycles of the existing resins. (Extending the cure cycle over a longer period of time was shown in Subsection 6.1 and Figure 46 to yield relatively ductile materials.)

- Finally, the transverse and shear strengths of composites can be increased by decreasing the volume fraction of ineffective fibers, $\bar{k}_{if}$. The latter is expected to be a function of the fiber-matrix interface. Establishing what are the optimum properties of the interface to minimize $\bar{k}_{if}$ and thereby maximize σ_T^* and τ_{LT}^* would require indepth theoretical study of the problem.

Section 9

REFERENCES

1. L. B. Greszczuk. Interfiber Stresses in Filamentary Composites. AIAA Journal, 1971; Vol. 9, No. 7, P 1274-12480.

2. L. A. Fil'shtinskii. Stresses and Displacements in an Elastic Sheet Weakened by a Doubly Periodic Set of Equal Circular Holes. Prikladnaia Math. i Mekh., 1964; Vol. 28, No. 3, P 430-441.

3. D. A. Adams and D. R. Doner. Transverse Normal Loading of a Unidirectional Composite. Journal of Composite Materials, 1967; Vol. 1, No. 2, P 152-164.

4. D. A. Adams and D. R. Doner. Longitudinal Shear Loading of a Unidirectional Composite. Journal of Composite Materials, 1967; Col. 1, No. 1, P 4-18.

5. G. Pickett. Elastic Moduli of Fiber-Reinforced Plastic Composites. (Chapter 2) of Fundamental Aspects of Fiber-Reinforced Composites. R. T. Schwartz (editor). Interscience Publishers, New York, 1968; p 13-27.

6. R. Bailey and R. Hicks. Behavior of Perforated Plates Under Plane Stress. Journal of Mechanical Engineering Science, 1960; Vol. 2, No. 2, P 143-161.

7. S. Timoshenko. Theory of Elasticity. McGraw-Hill Book Company, Inc., New York, 1939.

8. E. R. Butcher. Transverse Tensile Properties of an Unbonded Model Composite. Journal of Material Science, No. 7, 1972.

9. C. B. Norris. Strength of Orthotropic Materials Subjected to Combined Stresses. Forrest Products Laboratory Report, FPL 1816, July 1950.

10. Structural Design Guide for Advanced Composites. Prepared Under AFML Contract F33615-69-C-1368 by North American Rockwell Corp., August 1969.

11. W. N. Reynolds. Physical Properties of Graphite. Elsevier Publishing Company, Ltd., New York, 1968.

12. "Integrated Research on Carbon Composite Materials." Technical Report AFML-TR-66-310, Part II, December 1967, P 269.

13. "Advanced Composites Material Study for Millimeter Wavelength Antennas." Technical Report AFML-TR-71-205, Vol. 1, October 1971, P 25.

14. L. B. Greszczuk. Micromechanics Failure Criteria for Composites. Presented at AIAA/ASME 12th Structures, Structural Dynamics and Material Conference, Anahe , California, April 1971.

15. J. V. Noyes and B. H. Jones. Crazing and Yielding of Reinforced Plastics. Air Force Materials Laboratory Technical Report, AFML-TR-68-51, March 1968.

16. L. B. Greszczuk. Effect of Combined Loading on Shear Strength of Composites and Adhesively Bonded Joints. MDC Report G-2613, December 1971 (Unpublished).

17. R. C. Novak. Investigation of Graphite Filament Reinforced Epoxies. Final Report Prepared by Philco-Ford Corporation Under Naval Air Systems Command Contract N00019-67-C-0354, May 1968.

18. G. L. Hanna and S. Steingeiser. Defining the Adhesion Characteristics in Advanced Composites. Composite Materials: Testing and Design. ASTM Publication STP 460, 1969, P 182.

19. R. C. Novak. Fracture in Graphite Filament Reinforced Epoxy Loaded in Shear. Composite Materials: Testing and Design. ASTM Publication STP 460, 1969, P 540.

20. A. Nadai. Theory of Flow and Fracture of Solids. McGraw-Hill Book Company, Inc., New York, 1950, P 210.

APPENDIX A
STRESSES AND DEFORMATIONS OF POROUS SOLIDS

APPENDIX A
STRESSES AND DEFORMATIONS OF POROUS SOLIDS

Microscopic observations of composites performed at MDAC, NRL, and by other investigators indicate that the voids within the matrix are nearly circular in cross section and are elongated. It is reasonable therefore to idealize the voids as cylindrical in shape. The influence of such voids and stresses and deformations of the matrix can be established as shown herein.

A.1 EFFECTIVE YOUNG'S MODULUS OF A SOLID CONTAINING A SQUARE ARRAY OF CYLINDRICAL VOIDS

For a solid containing cylindrical voids arranged in a square array (Figure A-1), the average stress σ_x at any point x, such as at section A-A, is

$$\sigma_x = \frac{\sigma_1 \ell}{\ell - \sqrt{R^2 - x^2}} \tag{A-1}$$

in the region $0 \leq x \leq R$ and

$$\sigma_x \approx \sigma_1 \tag{A-2}$$

in the region $R \leq x \leq \ell$, where the various terms are defined in Figure A-1. The average strain, ϵ_x at any point x is then

$$\epsilon_x = \frac{\sigma_x}{E} \tag{A-3}$$

Since ϵ_x is a function of x, therefore the strain over the width 2ℓ of the repeating element is

$$\epsilon_1 = \frac{1}{\ell}\left[\int_o^R \epsilon_x \, dx\right] + \left(\frac{1-\lambda}{1-\frac{\pi}{4}\lambda^2}\right)\sigma_1 \tag{A-4}$$

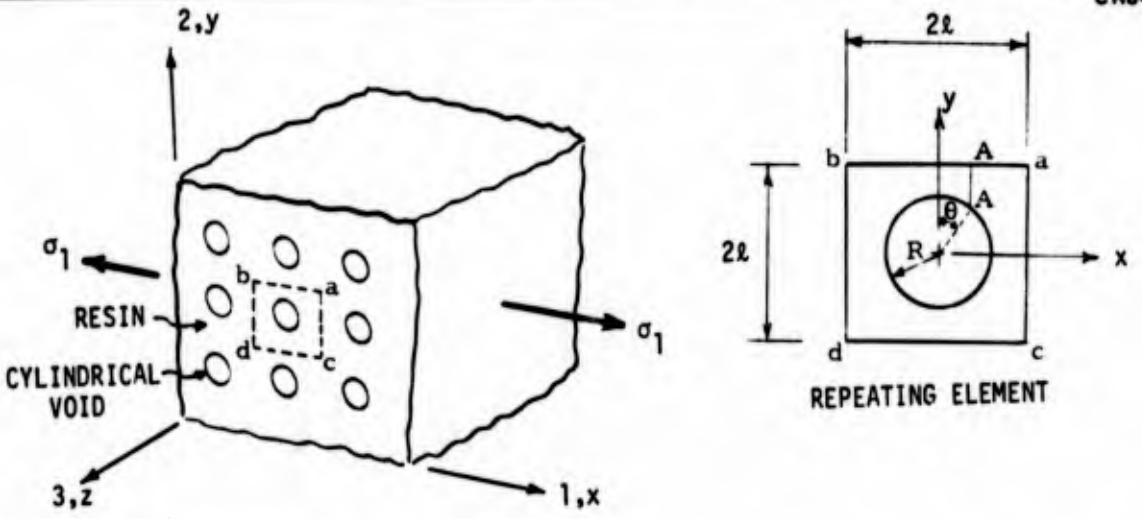

Figure A-1. Solid Containing a Square Array of Cylindrical Voids

Combining Equations A-1, A-2, A-3, and A-4, and integrating over the indicated limits gives

$$\epsilon_1 = \frac{\sigma_1}{E}\left\{\frac{1-\lambda}{1-\frac{\pi}{4}\lambda^2} - \frac{\pi}{2} + \frac{2}{\sqrt{1-\lambda^2}}\tan^{-1}\sqrt{\frac{1+\lambda}{1-\lambda}}\right. \tag{A-5}$$

where

$$\lambda = R/\ell = \sqrt{\frac{4k_v}{\pi}} \tag{A-6}$$

and k_v is the volume fraction of voids. The effective Young's modulus E_1 of a solid containing cylindrical voids is then simply

$$E_1 = \frac{\sigma_1}{E_1} = \frac{E}{\left\{\frac{1-\lambda}{1-\frac{\pi}{4}\lambda^2} - \frac{\pi}{2} + \frac{2}{\sqrt{1-\lambda^2}}\tan^{-1}\sqrt{\frac{1+\lambda}{1-\lambda}}\right\}} \tag{A-7}$$

The effective Young's modulus in Direction 2 is also equal to E_1.

A.2 INTERNAL STRESSES IN POROUS SOLIDS DUE TO TRANSVERSE NORMAL LOADING

If a solid containing a square array of cylindrical voids is subjected to normal loading (Figure A-1), stress concentrations will occur due to the presence of voids. To obtain these stress concentrations and the stress distribution within the repeating element bounded by boundaries ab, bd, dc, and ca (Figure A-1), advantage can be taken of the symmetry conditions, which require that the boundaries of the deformed repeating element remain parallel to the boundaries of the undeformed repeating element. The latter requirement essentially imposes a condition that the external boundaries of the repeating element undergo uniform strains at $x = \pm\ell$ and at $y = \pm\ell$. The second condition that needs to be satisfied is that the radial and shear stresses vanish at the boundary of the void, that is at

$$R = \sqrt{x^2 + y^2} \quad (x, y \leq R)$$

Both conditions can be satisfied if we seek a solution in the form

$$\sigma_x = (f_1)(f_2)\,\sigma_1 \tag{A-8}$$

where f_1 and f_2 are the still unknown functions, one of which, f_1, satisfies the conditions at the void boundary, and the other, f_2, satisfies the conditions at the external boundary ($x=\ell$) of the repeating element. The function f_1 can be determined from the results for a plate with a single hole. For this problem (Figure A-2), the three stress components due to remotely applied stress S are (Reference 7)

CR84

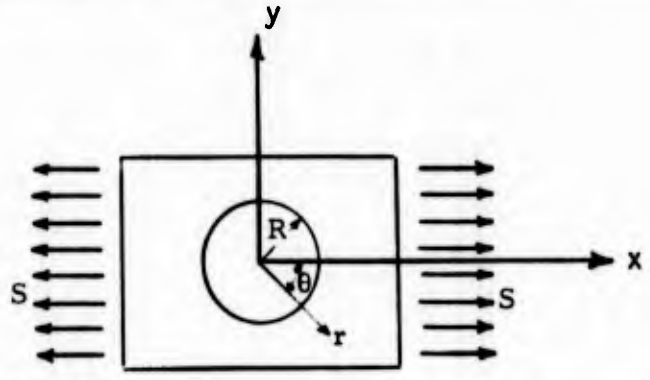

Figure A-2. Plate with a Single Hole

$$\sigma_r = \frac{S}{2}\left[\left(1 - \frac{R^2}{r^2}\right) + \left(1 + \frac{3R^4}{r^4} - \frac{4R^2}{r^2}\right)\cos 2\theta\right]$$

$$\sigma_\theta = \frac{S}{2}\left[\left(1 + \frac{R^2}{r^2}\right) - \left(1 + \frac{3R^4}{r^4}\right)\cos 2\theta\right] \qquad \text{(A-9)}$$

$$\sigma_{r\theta} = -\frac{S}{2}\left[1 - \frac{3R^4}{r^4} + \frac{2R^2}{r^2}\right]\sin 2\theta$$

These stresses can be expressed in terms of Cartesian coordinates by means of the following equations:

$$\sigma_x = \sigma_r \cos^2\theta + \sigma_\theta \sin^2\theta - \sigma_{r\theta} \sin 2\theta \qquad \text{(A-10)}$$

$$\sigma_y = \sigma_r \sin^2\theta + \sigma_\theta \cos^2\theta + \sigma_{r\theta} \sin 2\theta \qquad \text{(A-11)}$$

$$\sigma_{xy} = \frac{1}{2}(\sigma_r - \sigma_\theta) \sin 2\theta + \sigma_{r\theta} \cos 2\theta \qquad \text{(A-12)}$$

$$\sin\theta = \frac{y}{\sqrt{x^2+y^2}} \qquad \text{(a)}$$

$$\cos\theta = \frac{x}{\sqrt{x^2+y^2}} \qquad \text{(b)}$$

$$\sin 2\theta = \frac{2xy}{x^2+y^2} \qquad \text{(c)} \qquad \text{(A-13)}$$

$$\cos 2\theta = \frac{x^2-y^2}{x^2+y^2} \qquad \text{(d)}$$

$$r = \sqrt{x^2+y^2} \qquad \text{(e)}$$

Combining Equations A-9, A-10, A-11, A-12, and A-13 gives

$$\sigma_x = \frac{S}{2}\left\{\frac{2x^4+2y^4+4x^2y^2-R^2x^2+R^2y^2}{(x^2+y^2)^2} + \frac{4R^2x^2(3y^2-x^2)}{(x^2+y^2)^3} + \frac{3R^4(x^4+y^4-6x^2y^2}{(x^2+y^2)^4}\right\} \quad (A-14)$$

$$\sigma_y = \frac{S}{2}\left\{\frac{R^2(x^2-y^2)}{(x^2+y^2)^2} + \frac{4R^2y^2(y^2-3x^2)}{(x^2+y^2)^3} + \frac{3R^4(6x^2y^2-y^4-x^4)}{(x^2+y^2)^4}\right\} \quad (A-15)$$

$$\sigma_{xy} = -\frac{S}{2}\left\{\frac{2R^2xy}{(x^2+y^2)^2} + \frac{8R^2xy(x^2-y^2)}{(x^2+y^2)^3} - \frac{12R^4xy(x^2-y^2)}{(x^2+y^2)^4}\right\} \quad (A-16)$$

Thus for the loading shown in Figure A-2, if f_1 is taken as

$$f_1 = \frac{1}{2}\left\{\frac{2x^4+2y^4+4x^2y^2-R^2x^2+R^2y^2}{(x^2+y^2)^2} + \frac{4R^2x^2(3y^2-x^2)}{(x^2+y^2)^3} + \frac{3R^4(x^4+y^4-6x^2y^2)}{(x^2+y^2)^4}\right\} \quad (A-17)$$

the conditions at the void boundary will be satisfied. To satisfy the uniform strain condition at $x=\ell$, requires that f_2 be made proportional to the transverse stiffness E_x of the repeating element at any point y (Reference 1). The approximate expression for f_2 can be taken as

$$f_2 \approx \frac{E}{E_1}\left[1 - \sqrt{\left(\frac{R}{\ell}\right)^2 - \left(\frac{y}{\ell}\right)^2}\right] \quad (A-18)$$

in the region $0 \leq y \leq R$ and

$$f_2 \approx \frac{E}{E_1} \quad (A-19)$$

in the region $R \le y \le \ell$ where E_1 is given by Equation A-7. The final expression for σ_x now becomes (at $0 \le y \le r$)

$$\sigma_x = \frac{\sigma_1}{2}\left[1 - \sqrt{\left(\frac{R}{\ell}\right)^2 - \left(\frac{y}{\ell}\right)^2}\right]\left(\frac{E}{E_1}\right)\left\{\frac{2x^4+2y^4+2x^2y^2-R^2x^2+y^2R^2}{(x^2+y^2)^2}\right.$$

$$\left. + \frac{4R^2x^2(3y^2-x^2)}{(x^2+y^2)^3} + \frac{3R^4(x^4+y^4-6x^2y^2)}{(x^2+y^2)^4}\right\} \qquad \text{(A-20)}$$

The stress σ_x at two points of interest ($y=0$, $x=\ell$ and $y=\ell$, $x=\ell$) are

$$\sigma_x = \frac{\sigma_1}{2}(1-\lambda)(2-5\lambda^2+3\lambda^4)\frac{E}{E_1} \quad \text{at } y=0,\ x=\ell \qquad \text{(A-21)}$$

$$\sigma_x = \frac{\sigma_1}{2}\left(2+\lambda^2-\frac{3}{4}\lambda^4\right)\frac{E}{E_1} \quad \text{at } y=x=\ell \qquad \text{(A-22)}$$

The approximate expression for the stress σ_y can be obtained in a similar way and is:

$$\sigma_y = \frac{\sigma_1}{2}\left[1 - \sqrt{\left(\frac{R}{\ell}\right)^2 - \left(\frac{y}{\ell}\right)^2}\right]\left(\frac{E}{E_1}\right)\left\{\frac{R^2(x^2-y^2)}{(x^2+y^2)^2} + \frac{4R^2y^2(y^2-3x^2)}{(x^2+y^2)^3}\right.$$

$$\left. + \frac{3R^4(6x^2y^2-y^4-x^4)}{(x^2+y^2)^4}\right\} \qquad \text{(A-23)}$$

Again the stresses σ_y at the two points of interest are

$$\sigma_y = \frac{\sigma_1}{2}(1-\lambda)\left(\lambda^2-\frac{3}{4}\lambda^4\right)\frac{E}{E_1} \quad \text{at } x=\ell,\ y=0 \qquad \text{(A-24)}$$

$$\sigma_y = \frac{\sigma_1}{2}\left(-\lambda^2+\frac{3}{4}\lambda^4\right)\frac{E}{E_1} \quad \text{at } x=y=\ell \qquad \text{(A-25)}$$

To obtain the stress distribution at the points where the stresses are maximum (at Section x=0 in Figure A-1) it is sufficient to consider f_1 at x=0. From Equation A-17, at x=0

$$f_1 = \frac{1}{2}\left\{2 + \frac{R^2}{y^2} + \frac{3R^4}{y^4}\right\} \qquad \text{(A-26)}$$

The stress σ_x at that section will be of the form

$$\sigma_x = kf_1 \qquad \text{(A-27)}$$

where k is a constant evaluated from force equilibrium considerations. The condition of equilibrium at x=0, $R \leq y \leq \ell$ requires that

$$\sigma_1 = \frac{1}{\ell}\int_R^{\ell} kf_1 \, dy \qquad \text{(A-28)}$$

where σ_1 is the remotely applied stress.

Combining Equations A-26 and A-28, evaluating the integral and solving for k gives

$$k = \frac{2\sigma_1}{2-\lambda^2-\lambda^4} \qquad \text{(A-29)}$$

while combination of Equations A-29, A-27, and A-26 gives

$$\sigma_x = \left(\frac{2+\left(\frac{R}{y}\right)^2 + \frac{3R^4}{y^4}}{2-\lambda^2-\lambda^4}\right)\sigma_1 \qquad \text{(A-30)}$$

Similarly, the stress σ_y at x=0 is

$$\sigma_y = \frac{3\sigma_1\left[\left(\frac{R}{y}\right)^2 - \left(\frac{R}{y}\right)^4\right]}{2-\lambda^2-\lambda^4} \tag{A-31}$$

The stresses at the two points of interest x=0, y=R, and x=0, y=ℓ are:

At x=0, y=R

$$\sigma_x = \frac{6\sigma_1}{2-\lambda^2-\lambda^4} \tag{A-32}$$

$$\sigma_y = 0$$

At x=0, y=ℓ

$$\sigma_x = \left(\frac{2+\lambda^2+3\lambda^4}{2-\lambda^2-\lambda^4}\right)\sigma_1 \tag{A-33}$$

$$\sigma_y = \left\{\frac{3(\lambda^2-\lambda^4)}{2-\lambda^2-\lambda^4}\right\}\sigma_1 \tag{A-34}$$

APPENDIX B
TEST DATA FOR PHOTOELASTIC TEST SPECIMENS

Table B-1

STRAINS AND STRESS CONCENTRATIONS IN A PERFORATED PLATE WITH $(R/\ell) = 0.252$ ($k_v = 4.94\%$)

Location	Strain Gage Data					Photoelasticity Data	
	$\frac{\epsilon_x}{P}$ (1)	$\frac{\epsilon_y}{P}$	$\frac{\sigma_x}{\sigma_1}$	$\frac{\sigma_y}{\sigma_1}$	$\frac{p-q}{\sigma_1}$ (2)		$\frac{p-q}{\sigma_1}$ (2)
O	0.9908	-0.3088	1.028	0.044	0.984		1.038
A	1.099	-0.2496	1.179	0.157	1.022		1.123
B	--	--	(2.983)(3)	(0.00)	--		2.983
C	1.295	-0.5435	1.287	-0.105	1.392		1.380
D	0.8004	-0.2248	0.841	0.064	0.777		0.869
E	--	--	(0.00)	(-0.953)	--		0.953

(1) Stresses and strain evaluated at an applied load P = 1220.10 lb which corresponds to applied stress σ_1 = 743.0 psi.

(2) p-q denotes difference between principal stresses, p being the maximum stress, q being the minimum.

(3) Numbers in parenthesis were obtained by photoelasticity.

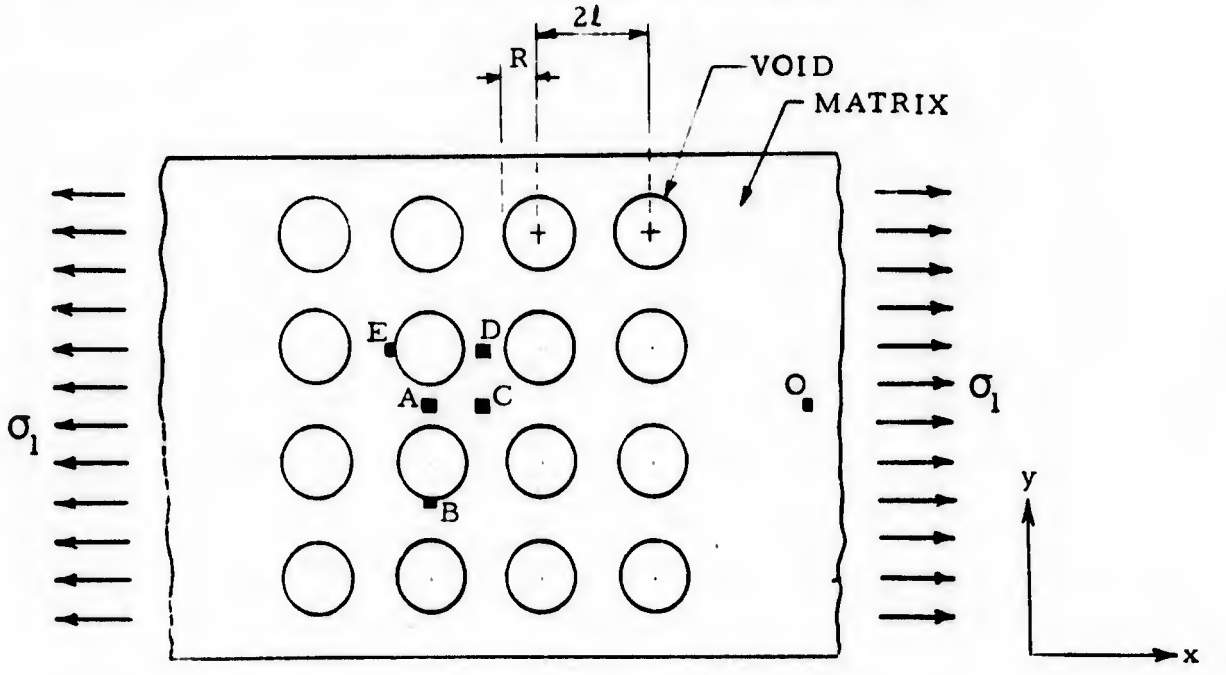

Preceding page blank

Table B-2

STRAINS AND STRESS CONCENTRATIONS IN A PERFORATED PLATE WITH $(R/\ell) = 0.358$ ($k_v = 10.07\%$)

Location	Strain Gage Data					Photoelasticity Data	
	$\frac{\epsilon_x}{P}$ (1)	$\frac{\epsilon_y}{P}$	$\frac{\sigma_x}{\sigma_1}$	$\frac{\sigma_y}{\sigma_1}$	$\frac{p-q}{\sigma_1}$ (2)		$\frac{p-q}{\sigma_1}$ (2)
O	1.062	-0.3188	1.107	0.062	1.045		1.035
A	1.198	-0.1533	1.333	0.310	1.023		1.109
B	--	--	(3.237)(3)	(0.00)	--		3.237
C	1.497	-0.7042	1.457	-0.210	1.667		1.559
D	0.5829	-0.1188	0.631	0.099	0.532		0.623
E	--	--	(0.00)	(-0.869)	--		0.869

Table B-3

STRAINS AND STRESS CONCENTRATIONS IN A PERFORATED PLATE WITH $(R/\ell) = 0.437$ ($k_v = 15.0\%$)

Location	Strain Gage Data					Photoelasticity Data	
	$\frac{\epsilon_x}{P}$ (1)	$\frac{\epsilon_y}{P}$	$\frac{\sigma_x}{\sigma_1}$	$\frac{\sigma_y}{\sigma_1}$	$\frac{p-q}{\sigma_1}$ (2)		$\frac{p-q}{\sigma_1}$ (2)
O	1.080	-0.3188	1.128	0.069	1.059		1.034
A	1.359	-0.1087	1.539	0.428	1.111		1.199
B	--	--	(3.148)(3)	(0.00)	--		3.148
C	1.705	-0.8425	1.643	-0.286	1.929		1.844
D	0.3977	-0.0050	0.461	0.156	0.305		0.285
E	--	--	(0.00)	(-0.720)	--		0.720

(1), (2), (3) See footnotes under Table B-1.

Table B-4

STRAINS AND STRESS CONCENTRATIONS IN A PERFORATED PLATE WITH $(R/\ell) = 0.505$ ($k_v = 20.0\%$)

Location	Strain Gage Data					Photoelasticity Data	
	$\frac{\epsilon_x}{p}$ (1)	$\frac{\epsilon_y}{p}$	$\frac{\sigma_x}{\sigma_1}$	$\frac{\sigma_y}{\sigma_1}$	$\frac{p-q}{\sigma_1}$ (2)		$\frac{p-q}{\sigma_1}$ (2)
O	1.072	-0.3559	1.104	0.022	1.082		1.019
A	1.544	-0.1185	1.750	0.492	1.258		1.259
B	-	-	(3.447)	(0.00)	-		3.447
C	1.880	-0.9982	1.783	-0.396	2.179		2.068
D	0.2026	-0.0345	0.222	0.042	0.180		0.135
E	-	-	(0.00)	(-0.615	-		0.615

Table B-5

STRAINS AND STRESS CONCENTRATIONS IN A PERFORATED PLATE WITH $(R/\ell) = 0.619$ ($k_v = 30.1\%$)

Location	Strain Gage Data					Photoelasticity Data	
	$\frac{\epsilon_x}{p}$ (1)	$\frac{\epsilon_y}{p}$	$\frac{\sigma_x}{\sigma_1}$	$\frac{\sigma_y}{\sigma_1}$	$\frac{p-q}{\sigma_1}$ (2)		$\frac{p-q}{\sigma_1}$ (2)
O	1.025	-0.3682	1.044	-0.011	1.055		1.080
A	2.070	-0.2126	2.325	0.596	1.729		1.753
B	-	-	(3.688)	(0.00)	-		3.688
C	2.164	-1.193	2.034	-0.507	2.541		2.563
D	-0.0520	0.1036	-0.018	0.099	0.117		0.135
E	-	-	(0.00)	(-0.599)	-		0.599

(1), (2), (3) See footnotes under Table B-1.

TABLE B-6

EXPERIMENTAL RESULTS ON INTERNAL STRESSES IN A COMPOSITE MODEL CONSISTING OF FIBERS, VOIDS AND MATRIX

LOCATION	STRESS CONCENTRATION σ_x/σ_1 IN SPECIMEN #1 (k_f = 40.07%; k_{vc} = 1.01%) (1)	STRESS CONCENTRATION σ_x/σ_1 IN SPECIMEN #2 (k_f = 54.54%, k_{vc} = 1.37%) (1)
a	3.099	3.006
b	4.380	3.984
c	1.405	1.177
d	1.512	0.368
e	1.057	1.007

(1) Stress concentrations evaluated at an applied load of P=871.5 lbs which corresponds to an applied stress σ_1=415 psi for specimen #1 and σ_1=484 psi for specimen #2

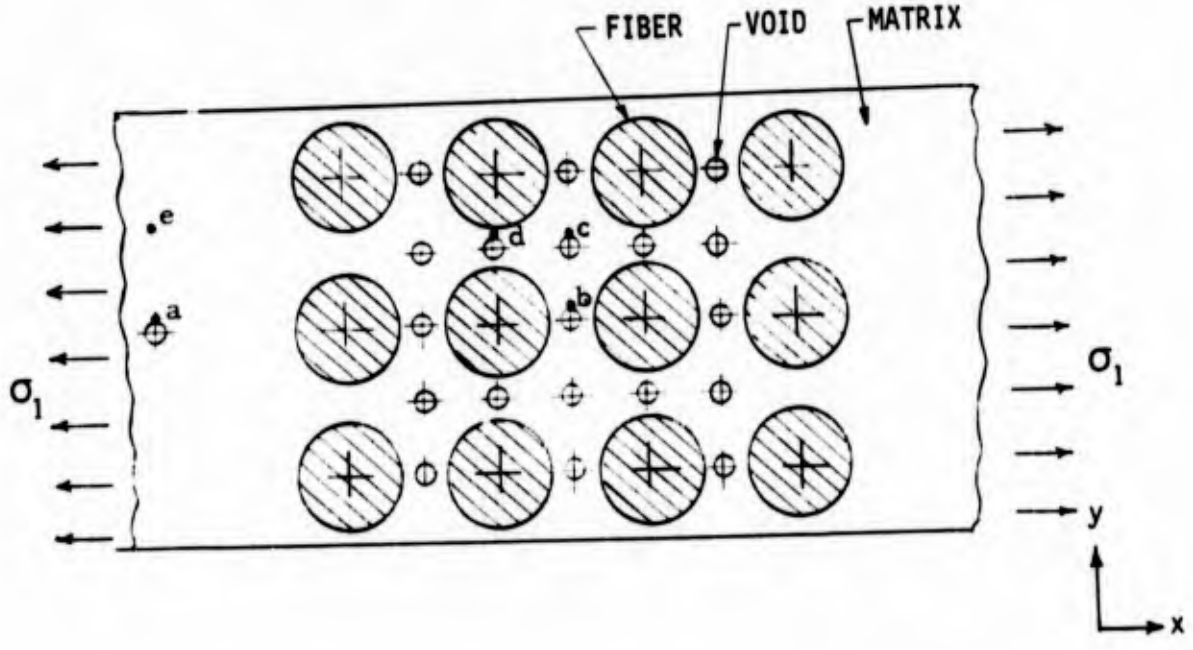

APPENDIX C

NUMERICAL EXAMPLES ON USE OF MICROMECHANICS FAILURE CRITERIA TO PREDICT THE TRANSVERSE TENSILE STRENGTH AND INTERLAMINAR SHEAR STRENGTH OF COMPOSITES

EXAMPLE 1 - TRANSVERSE TENSILE STRENGTH OF COMPOSITE

Given: Composite consisting of S-glass fibers and 1004 epoxy resin. The fiber content is $\bar{k}_{if} = 55\%$, void content $k_{vc} = 2\%$, ineffective fiber content, $\bar{k}_{if} = 0$.

The properties of constituents are:

$E_f = 12.4 \times 10^6$ psi (Young's modulus of fibers)

$E_r = 0.537 \times 10^6$ psi (Young's modulus of resin)

$\nu_f = 0.22$ (Poisson's ratio of fibers)

$\nu_r = 0.347$ (Poisson's ratio of resin)

$\sigma_r = 11.95 \times 10^3$ psi (tensile strength of resin)

$\tau_r = 15 \times 10^3$ psi (shear strength of resin)

The first step is to determine λ^*. Using Equation (29)

$$\lambda^* = 0.238$$

Now from Figure 9 or Equation (1) the E_1/E ratio corresponding to $\lambda^* = 0.238$ is

$$E_{1/E} \approx 0.92$$

or the reduced Young's modulus of resin containing voids is

$$E_r^* = (0.92)(E_r) = 494 \times 10^3 \text{ psi}$$

The stress concentrations due to fibers, K_x^*, K_y^* and K_z^* corresponding to

$$E_f/E_r^* = 25.1 \text{ and } \bar{k}_f = 55\%$$

are obtained from Table 1 by extrapolation. They are:

$$K_x^* \approx 1.746$$

$$K_y^* \approx 0.908$$

$$K_z^* \approx 0.908$$

The stress concentrations due to voids, $\bar{K}^*_{xA}$, K^*_{yD}, K^*_{xD}, K^*_{yA} and K^*_{zr} are obtained from Equations (32), (33), (34), (35) and (36)*. These are

$$\bar{K}^*_{xA} = 1.313$$

$$K^*_{yD} = 0.022$$

$$K^*_{xD} = 0.715$$

$$K^*_{yA} = 0.084$$

$$K^*_{zr} = 1.047$$

Substitution for K^*_x, K^*_y, K^*_z, K^*_{yD}, $\bar{K}^*_{xD}$, K^*_{yA}, K^*_{zr} and σ_r in Equation (31) gives

$$\sigma^*_T = 8,440 \text{ psi}$$

which is the predicted transverse tensile strength of composite.

EXAMPLE 2. SHEAR STRENGTH OF COMPOSITE

Assuming the same properties of composite as in the first example, λ^* is still the same as before, that is

$$\lambda^* = 0.238$$

From Equation (5) or Figure 10, the G_{13}/G ratio corresponding to λ^* is

$$\frac{G_{13}}{G} = 0.95$$

or the reduced shear modulus of the resin containing voids is

$$G^*_r = (0.95)(G_r) = 0.194 \times 10^6 \text{ psi}$$

*K^*_{yD}, K^*_{xD}, and K^*_{yA} can also be obtained from Figures 16 and 17.

where G_r was calculated from the usual relationship

$$G_r = \frac{E_r}{2(1 + \nu_r)}$$

The shear stress concentration due to fibers, K^*_{xz} corresponding to

$$\frac{G_f}{G^*_r} = 25.5 \text{ and } \overline{k}_f = 55\%$$

is obtained from Table 2 and is

$$K^*_{xz} = 1.748$$

The term K^*_{xzA} is evaluated from Equation (42) and is

$$K^*_{xzA} = 1.31$$

Substitution for K^*_{xz}, K^*_{xzA} and τ_r in Equation (41) gives

$$\tau^*_{LT} = 6,550 \text{ psi}$$

which is the predicted shear strength of composite.

APPENDIX D

TEST DATA FOR RESIN CASTINGS AND FOR TRANSVERSE TENSILE AND INTERLAMINAR SHEAR STRENGTH OF ACTUAL COMPOSITES

TABLE D-1

TEST DATA FOR 1004 EPOXY AND SC1008 PHENOLIC

SPECIMEN NUMBER (1)	DESIGNATION	WIDTH (in.)	THICK. (in.)	AREA (in)	LOAD (lbs)	TENSILE FAILURE STRESS (psi) (3)	FAILURE STRAIN (%) (3)	E x 10^{-6} (psi)	ν	FAILURE LOCATION (2)	REMARKS
1*	Dark(Phen)	0.244	0.0982	0.0240	(158)	(6580)	---	0.632		PIN	Postcured @ 350°F for 4 hours
2*	Dark(Phen)	0.246	0.0982	.02415	(365)	(15120)	(2.74)	0.658		PIN	
3	Light(Phen)	0.248	0.1009	0.02500	322	12870	4.15	0.551		T.S.	
4*	Light(Phen)	0.248	0.1010	0.02505	(307)	(12250)	(3.13)	0.570		PIN	
1**	Dark(Phen)	0.124	0.0985	0.01222	195	15960	---	---		T.S.	Postcured @ 350°F for 4 hours
2**	Dark(Phen)	0.125	0.0985	0.01232	204	16560	---	---		T.S.	
4**	Light(Phen)	0.125	0.1014	0.01268	160	12620	---	---		T.S.	
TR1	Light(Phen)	0.250	0.0980	0.0245	(162)	(6610)	(1.4)	0.560	0.352	S.G.	Strain Gage
TR2	"	0.250	0.0982	0.0246	282	11460	>2.5	0.520		T.S.	
TR3	"	0.250	0.0990	0.0248	283	11810	---	---		T.S.	
TR4	"	0.247	0.1009	0.0250	288	11565	5.65	0.566		T.S.	
TR5	"	0.250	0.1012	0.0249	292	11540	4.85	0.589		T.S.	Polished With 910 Adhesive
TR7	"	0.250	0.1014	0.0246	296	11655	---	---		T.S.	
TY-1	1004 Epoxy	0.250	0.098	0.0245	(180)	(7345)	(1.56)	0.595	0.352	S.G.	
TY-2	"	0.250	0.004	0.0250	(213)	(8520)	(2.0)	0.563	0.342	S.G.	
TY-3	"	0.250	0.099	0.0248	290	11690	---	---		T.S.	
TY-4	"	0.250	0.098	0.0245	313	12770	>2.9	0.453		T.S.	
TY-5	"	0.251	0.099	0.0250	285	11400	2.78	0.537		T.S.	

(1) *, ** denotes retest of the same specimen

(2) T.S. denotes failure in test section
S.G. denotes failure at lower stress because of strain gage

(3) Numbers in Parenthesis denote that failures were not valid; these values not used in average

TABLE D-2

TEST DATA FOR GLASS/EPOXY COMPOSITES

SPECIMEN NUMBER	SPECIFIC GRAVITY(1)			RESIN CONTENT (%)			k_{vc}(%)	k_f(%)	$\bar{k}_f$(%)	$E_T \times 10^{-6}$psi		$\sigma_T \times 10^{-3}$psi		$\tau_{LT} \times 10^{-3}$psi	
	E	T.T.S.	AVE	E	T.T.S.	AVE				ACTUAL	AVE	ACTUAL	AVE	ACTUAL	AVE
4-1	1.995	2.0099	2.0274	19.9	19.52	18.14	3.52	67.6	65.2	2.78	2.61	4.76	4.505	10.72	10.62
4-2		2.0303			17.89		3.84	70.0	67.4	2.45		4.25		10.73	
4-3		2.0420			17.01		4.01	71.2	68.2					10.41	
5-1	1.893	1.7993	1.7716	26.0	27.67	29.50	7.86	56.9	52.5	1.653	1.72	2.850	3.077	9.53	9.82
5-2		1.7706			29.15		8.28	55.1	50.5	1.877		2.720		9.86	
5-3		1.7448			31.68		7.89	52.2	48.1	1.614		3.660		10.06	
27-1	1.907	1.9043	1.9083	24.71	24.06	23.72	3.39	61.6	59.6	2.18	2.22	3.500	3.740	12.08	12.13
27-2		1.9216			23.45		4.77	62.3	59.4	2.21		4.400		12.37	
27-3		1.8990			23.64		5.75	62.1	58.5	2.26		3.320		11.93	
15-1	1.859	1.8507	1.8380	32.5	33.03	33.62	1.32	50.6	50.0	1.62	1.68	5.380	5.922	13.77	13.63
15-2		1.8401			32.85		2.00	50.9	49.9	1.76		6.060		13.47	
15-3		1.8231			34.97		1.41	48.6	47.9	1.73		5.150		13.64	
15-4										1.57		7.100			
2-1	1.820	1.8105	1.8356	36.0	36.05	34.64	1.29	47.4	46.8	1.61	1.65	7.88	7.78	11.80	11.90
2-2		1.8674			32.51		0.82	51.2	50.8	1.71		8.78		12.06	
2-3		1.8288			35.37		0.81	48.1	47.7	1.63		6.67		11.85	
28-1	2.072	1.9777	2.0145	18.8	22.11	21.64	0.86	64.1	63.6		2.66	8.17	9.56	14.26	14.07
28-2		2.0089			22.41		1.26	63.7	62.9	2.41		9.70		14.23	
28-3		2.0568			20.41		0.55	66.5	66.0	2.91		10.80		13.72	
10-1	1.963	1.9378	1.9091	25.6	28.25	29.64	0.32	56.2	56.1	2.01	1.89	9.30	8.69	14.48	14.19
10-2		1.8814			30.67		1.41	53.4	52.7	1.77		9.11		14.17	
10-3		1.9080			30.01		0.54	54.2	54.0	1.89		7.65		13.93	
3-1	1.988	1.9975	2.006	29.1	23.81	23.29	0.74	61.9	61.5	2.31	2.40	8.65	8.85	14.50	14.33
3-2		2.0294			21.27		1.17	65.1	64.2	2.54		10.06		14.50	
3-3		1.9749			24.79		1.10	60.6	59.2	2.34		7.84		14.28	

(1) E denotes that results obtained from edge of panel
T.T.S. denotes that results obtained from transverse tension coupons

TABLE D-3

TEST DATA FOR GLASS/PHENOLIC COMPOSITES

SPECIMEN NUMBER	SPECIFIC GRAVITY(1)			RESIN CONTENT (%)			k_{vc}(%)	k_f(%)	$\bar{k}_f$(%)	$E_T \times 10^{-6}$ psi		$\sigma_T \times 10^{-3}$ psi(2)		$\tau_{LT} \times 10^{-3}$ psi	
	E	T.T.S.	AVE	E	T.T.S.	AVE				ACTUAL	AVE	ACTUAL	AVE	ACTUAL	AVE
22-1		1.8240			24.07		8.2	60.8	55.9	1.42		1.132		8.72	
22-2	1.771	1.6164	1.7206	23.0	26.09	24.49	17.3	58.2	48.1	1.09	1.41	1.253	1.351	9.00	8.47
22-3		1.7215			23.31		13.9	61.8	53.2	1.73		1.668		7.70	
29-1		1.8741			29.62		1.3	54.0	53.3	1.84		1.710		9.68	
29-2	1.925	1.8794	1.8783	27.39	29.15	29.06	1.7	54.5	53.6	1.67	1.77	.960	1.220	9.15	9.06
29-3		1.8819			28.40		1.9	55.4	54.1	1.81		.990		8.35	
8-1		1.9161			25.43		4.1	60.5	58.0			.505		3.38	
8-2	2.081	1.9259	1.9210	15.53	21.56	24.58	5.1	64.2	61.0			.310	0.40	3.58	3.44
8-3					26.77			57.5				.390		3.37	
20-1		1.9881						60.0	59.0					4.21	
20-2	1.969	2.0105	1.9849	22.8										4.48	4.34
20-3		1.9501						60.0	57.8					4.34	

(1) see footnote in Table D-2

(2) Specimens were curved; data not valid

TABLE D-4

TEST DATA FOR GRAPHITE/EPOXY AND GRAPHITE/PHENOLIC COMPOSITES

SPECIMEN NUMBER	SPECIFIC GRAVITY(1)			RESIN CONTENT (%)			k_{vc} (%)	k_f (%)	$\bar{k}_f$ (%)	$E_T \times 10^{-6}$ psi		$\sigma_T \times 10^{-3}$ psi		$\tau_{LT} \times 10^{-3}$ psi	
	E	T.T.S.	AVE	E	T.T.S.	AVE				ACTUAL	AVE	ACTUAL	AVE	ACTUAL	AVE
6-1 (3)		1.4680			38.78		2.1	53.6	52.5	0.960		6.39		11.74	
6-2	1.465	1.4558	1.4643	37.6	38.71	38.68	2.9	53.8	52.2	0.992	1.016	6.05	6.28	11.82	11.79
6-3		1.4691			38.55		2.1	53.9	52.7	1.097		6.39		11.80	
9-1		1.5027			34.24		1.1	58.5	57.8	1.08		6.47		14.22	
9-2	1.443	1.4960	1.4981	35.8	35.37	34.86	1.4	57.3	56.5	1.07	1.009	5.74	6.77	14.10	13.97
9-3		1.4957			34.97		1.5	57.7	56.8	1.12		8.11		13.60	
11-1		1.5010			35.56		0.9	57.1	56.6	1.10		6.56		11.78	
11-2	1.499	1.4991	1.4986	34.3	35.23	35.04	1.1	57.4	56.7	1.02	1.007	6.07	5.65	12.72	12.28
11-3		1.4958			34.34		1.6	58.4	57.5	1.09		4.32		12.34	
24-1		1.3856			37.54		8.0	55.0	50.6	0.94		3.93		7.24	
24-2	1.378	1.3768	1.3869	39.7	37.59	37.69	8.5	54.9	50.2	0.86	0.933	3.54	4.19	7.40	7.31
24-3		1.3983			37.96		7.0	54.6	50.8	1.00		5.04		7.30	
24-4												4.24			
30-1		1.4822			34.12		2.5	58.6	57.1	1.13		2.50		10.83	
30-2	1.498	1.4787	1.4781		35.67	35.12	2.5	57.0	55.6	1.07	1.133	2.82	2.93	10.91	10.87
30-3		1.4734			35.57		2.7	57.1	55.5	1.20		3.47		10.88	
14-1 (3)		1.3675			30.13		10.4	62.3	55.9	1.03		2.32		4.48	
14-2	1.365	1.3684	1.3684		29.45	29.58	10.5	63.1	56.4	1.09	1.09	2.60	2.52	4.04	4.40
14-3		1.3693			29.17		10.6	63.4	56.6	1.15		2.64		4.68	
7-1		1.3926			28.13		9.4	64.6	58.5	1.11		3.45		7.47	
7-2	1.422	1.3966	1.3937		27.90	28.09	9.2	64.8	58.8	1.24	1.186	3.17	3.51	6.95	7.25
7-3		1.3918			28.25		9.3	64.4	58.4	1.21		3.90		7.32	
21-1		1.5023			30.65		1.4	61.6	60.8	1.03		0.97(2)		9.56	
21-2	1.501	1.5033	1.5032		30.70	30.54	1.2	61.6	60.9	1.14	1.086	1.53(2)	1.14	9.45	9.41
21-3		1.5041			30.27		1.2	62.2	61.5			0.94(2)		9.22	

(1), (2) see footnotes in Tables D-2 and D-3

(3) Note specimens 6, 9, 11, 24, and 30 were made with 1004 Epoxy resins; specimens 19, 7, and 21 were made with SC1008 phenolic resin.

TABLE D-5

TEST DATA FOR BORON/EPOXY COMPOSITES (4)

SPECIMEN NUMBER	SPECIFIC GRAVITY(1)			RESIN CONTENT (%)			k_{vc}(%)	k_f(%)	$\bar{k}_f$(%)	$E_T \times 10^{-6}$ psi		$\sigma_T \times 10^{-3}$ psi		$\tau_{LT} \times 10^{-3}$ psi	
	E	T.T.S.	AVE	E	T.T.S.	AVE				ACTUAL	AVE	ACTUAL	AVE	ACTUAL	AVE
14-1		1.9709			22.48		5.8	62.5	58.9	1.90		6.31		13.83	
14-2(2)	1.980	1.9863	1.9821	(21.8)	24.57	24.08	3.5	59.7	57.6	2.73	2.403	6.86	6.67	13.47	13.69
14-3		1.9892			25.27		1.5	58.7	57.9	2.58		6.85		13.76	
13-1		2.0587			23.70		8.9	60.8	55.5	3.70		9.58		14.56	
13-2(2)	2.050	2.0584	2.0603	(20.0)	24.98	24.55	3.1	59.2	57.3	3.10	3.373	9.38	9.53	14.56	14.56
13-3		2.0638			24.96		3.0	59.3	57.5	3.32		9.62		14.56	
25-1		1.8201			26.34		9.9	57.3	51.6	1.94		6.40		13.20	
25-2(3)	1.878	1.8556	1.8517	(19.6)	24.95	26.25	9.2	59.1	53.6	2.52	2.270	7.08	7.01	13.00	13.00
25-3		1.8794			27.46		6.0	55.8	52.5	2.35		7.54		12.80	
26-1		1.9866			23.46		4.1	61.1	58.5	3.13		11.62		16.50	
26-2(3)	2.029	2.0163	2.0117	(18.3)	25.40	24.05	1.0	58.4	57.7	3.12	3.377	12.70	12.05	16.70	16.61
26-3		2.0322			23.34		2.0	61.1	59.9	3.88		11.83		16.62	

(1) see footnote in Table D-2

(2) Specimens made with 1004 Epoxy

(3) Specimens made with Harmco 5505

(4) Composites contained 104 glass scrim cloth